QUANTITATIVE LINEAR OPTICAL SCATTERING SPECTROSCOPY OF TWO-DIMENSIONALLY TEXTURED PLANAR WAVEGUIDES

by

WILLIAM JODY MANDEVILLE

B.S., United States Air Force Academy, 1988
M.S., Air Force Institute of Technology, 1992

A THESIS SUBMITTED IN PARTIAL FULFILMENT OF
THE REQUIREMENTS FOR THE DEGREE OF

DOCTOR OF PHILOSOPHY

in

THE FACULTY OF GRADUATE STUDIES

(Department of Physics
and Astronomy)
We accept this thesis as conforming
to the required standard

THE UNIVERSITY OF BRITISH COLUMBIA

June 2001

In presenting this thesis in partial fulfilment of the requirements for an advanced degree at the University of British Columbia, I agree that the Library shall make it freely available for reference and study. I further agree that permission for extensive copying of this thesis for scholarly purposes may be granted by the head of my department or by his or her representatives. It is understood that copying or publication of this thesis for financial gain shall not be allowed without my written permission.

Department of Physics and Astronomy
The University of British Columbia
Vancouver, Canada

Date 28 Jun 2001

Abstract

Linear white light spectroscopy in conjunction with rigorous computer modeling reveals the fundamental nature of the electromagnetic excitations associated with the simple lattice and defect superlattice texturing of 2D planar waveguides. By achieving unprecedented agreement between experimentally measured and rigorously simulated band structures of leaky modes associated with the second, and up to the seventh, zone-folded Brillouin zones of square and triangular lattice structures, a thorough characterization of the polarization and dispersive properties of these electromagnetic modes has been achieved. An evaluation of the usefulness of a newly developed diffraction measurement technique for probing band structure is presented in conjunction with data and simulations for waveguides with defect superlattices. Textured planar waveguides, as a powerful medium for engineering devices which control the propagation of light, are explored via the thorough characterization of a novel polymer waveguide, and a GaAs waveguide that was engineered to possess a flat band for use in non-linear optics applications; in addition an original design is discussed for an angle and polarization insensitive notch filter based on a localized defect mode.

Contents

List of Tables

List of Figures

Acknowledgements

I would like to thank my advisor, Dr. Jeff F. Young, for his unfailing support and inspired guidance. He patiently and unselfishly provided motivation, clarification and direction without regard for his pressing schedule.

I am indebted to the members of Dr. Young's lab (past and present) for their suggestions and assistance throughout the course of this project. In particular, I would like to thank: Dr. Paul Paddon for eloquently reintroducing me to the 'basics' after my seven year hiatus from graduate school; Vighen Pacradouni and Allan Cowan, for the many enlightening discussions we shared; Hong Ma for his enthusiastic contributions to the polymer research; and Alex Busch for his invaluable guidance with the "hard parts"– math and LaTex.

I also would like to acknowledge my wife, Chris, for her tremendous support throughout this ordeal, and my sons, Duncan, Jack and Kit, for their patience. I owe them a dept of gratitude that I will never be able to repay.

Chapter 1

Introduction

Photonic crystals are of great interest due to their potential to provide advances in science and technology comparable to the advances provided by semiconductors over the last 50 years. Photonic crystals do for photons what semiconductor crystals do for electrons. Nature created semiconductor crystals such that the atoms are arranged in a perfectly periodic lattice spaced on the order of the wavelength of the electrons propagating through them. This periodic "electrical" potential creates the rich band structure which has been studied and exploited since the 1950's. Nature has provided few crystals with an analogous "photonic" potential lattice spaced on the order of the wavelength of light. [18, 36] However, with recent technological advances, such crystals are being manufactured. These man-made, low-loss periodic dielectric media are known as "photonic crystals." [12] The term"photonic crystal" is used to describe structures in which a periodic modulation of the index of refraction is used to control the propagation of light through Bragg diffraction. In general the periodicity can be in one dimension (1D), 2D or 3D. The unusual optical properties of 1D textured dielectrics were recognized

and exploited long before the term "photonic crystal" was introduced.

The familiar "quarter-wave dielectric stack" structure is essentially a photonic crystal. It uses alternating layers of high and low refractive index materials to efficiently reflect normally-incident light with wavelengths in a range of approximately twice the optical period[1] of the stack. The light within this "forbidden gap" is diffracted backwards, so that the reflection process is lossless. The width of the gap scales as the difference in the refractive indices, Δn, of the constituent layers, and the sharpness of the gap edges increases as the number of layers increases. For typical dielectric materials, such as a quarter wave stack, $\Delta n \leq 0.5$, and the center frequency and width of the gap vary rapidly as the incident angle of the radiation is varied away from the normal. In particular, the gap shrinks and then vanishes at angles greater than $\sim 30°$. [9] These effects of 1D photonic crystals have had great impact on optical applications; 2D and 3D photonic crystals have the potential to have an even greater impact.

In 1987, Yablonovitch [37] and John [13] independently recognized that a 3D-textured structure with a sufficiently large index-contrast could exhibit a complete bandgap: that is, such a material could inhibit the propagation of electromagnetic radiation within some continuous range of frequencies, regardless of the direction of propagation or the polarization of the field. The significance of this generalization can perhaps best be appreciated by considering that the total photonic density of states within such a material is dramatically altered from that available in bulk dielectrics. In the gap the density of states can approach zero, and near the band edges it is considerably enhanced over a

[1]The optical period is the vacuum wavelength divided by the average index of the periodic dielectric.

relatively narrow range of frequencies. This should profoundly affect the fundamental properties of electronic oscillators in these materials, and these modified properties may well form the basis of new optical technologies.

Yablonovitch et al. [38] were the first to realize a full 3D photonic crystal by drilling a dielectric block full of holes on the order of centimeters in diameter. The resulting face-centered cubic (FCC) crystal structure exhibits a full bandgap at microwave frequencies. By inserting an appropriate defect site within these crystals it is possible to completely localize radiation at frequencies that fall within the bandgap. In finite-sized crystals, these localized defect states act as high quality (Q), dispersionless filters. Numerous applications for these microwave photonic crystals have been demonstrated, including narrow band notch filters, highly directional, low-loss antennae, and high-transmission 1D defect waveguides that can include abrupt, right-angle bends. [4, 7, 11, 34]

The potential impact of these crystals is even greater in the optical and near-infrared frequency domain where they may provide the platform technology needed to achieve highly integrated optical processing circuits. [1] Current optical fiber communication systems are based largely on discrete bulk or fiber optic components (splitters, switches, etc.) that are difficult to mass-produce in a cost-effective manner. Progress has been made towards integrating these functions on "optical chips" based on planar waveguide technologies. If the functions could be integrated using photonic crystals, it would represent the ultimate in miniaturization. This is because light propagating in photonic crystals with complete bandgaps can, in principle, be channeled through and coupled

between lossless defect-waveguides that contain bends with effective radii of curvature on the order of a single wavelength of light. The dispersion of these defect guides, and the dispersion of the background photonic crystal, can be tuned to achieve unique control over the propagation properties of the light in 3D. Furthermore, if implemented in an electronically resonant medium (such as a III-V semiconductor, like InP or GaAs), microcavity lasers can be realized that take advantage of the singular photonic density of states associated with isolated defect modes (effectively, microcavities with effective volumes less than 0.1 cubic microns). [35]

Photonic crystals with bandgaps in the near infrared require control over the dielectric texture on lengthscales of ~200–500 nm. While some groups have realized 3D crystal structures with gaps in the near infrared [3, 16, 39], they are very difficult to fabricate, especially when engineering defects into their structure. While 2D photonic crystals cannot possess full bandgaps, they do exhibit many of the attractive features of their 3D counterparts, while being easier to fabricate. Although the total density of photonic states cannot be reduced to zero in "pure" 2D crystals (i.e. ones that are translationally invariant normal to the plane of the texture), 2D photonic crystals can exhibit complete bandgaps if the out-of-plane momentum of the light is restricted. In fact, pure 2D crystals are in a sense "better" than 3D, in that the two orthogonal polarization states (transverse electric (TE) and transverse magnetic (TM)) are completely independent of each other, making it easier to achieve large bandgaps. In practice, there is always some out-of-plane

variation of the fields even in bulk 2D crystals, which means that the pure 2D electromagnetic simulations only approximate reality. The errors in propagation simulations are small in the limit of "tall" crystals and correspondingly large beam cross-sections, but this is not always a practical geometry outside of the laboratory. With respect to light-matter interactions, pure 2D models really only work if the dipole distribution is also purely 2D, which severely restricts the relevance of such simulations. If the dipole distribution is not translationally invariant, there will always be some components of its radiation directed out-of-plane, and these will, in general, couple to a finite density of photonic states.

Two-dimensionally textured slab waveguides are even simpler to fabricate because the texture must only be as thick as the waveguide, which is typically less than a few microns. This geometry is also directly compatible with existing optoelectronic technologies. With this "2D + 1" geometry of textured planar waveguides, the translational invariance perpendicular to the textured plane is sacrificed from the outset. This immediately introduces a richness in the electromagnetic band structure that is absent in the pure 2D case, yet distinct from the pure 3D case. There are some drawbacks with this 2D + 1 geometry: there can be no complete photonic bandgaps, even in a restricted sense; and it is difficult (but not impossible) to avoid intrinsic out-of-plane coupling to radiation modes. Although consequences such as these may seem severe, the potential benefits of a relatively simple fabrication technology and the compatibility with integrated optoelectronics are significant. This motivates the search for a quantitative understanding of

light propagation in structures characterized by this 2D + 1 symmetry.

Many of the concepts originally motivated by the pure 3D and 2D simulations can be retained in the 2D +1 geometry, if care is taken to properly engineer the structure to minimize the influence of radiation modes and polarization mixing. In addition, the radiation coupling that is in some cases to be avoided, can in fact be used to advantage. Since the Brillouin zone is 2D, and momentum perpendicular to the layers is manifestly not a good quantum number for the electromagnetic excitations, it is possible to directly probe a significant fraction of the total band structure simply by illuminating it from the vacuum with collimated light. Furthermore, 2D textured waveguides offer a powerful medium for engineering the coupling of radiation into and out of the plane from the vacuum half space, which is desirable in certain applications.

The fundamental objective of the work described in this thesis is to acquire high-quality, broadband linear optical scattering data from a variety of 2D textured planar waveguide structures in order to reveal the fundamental nature of the corresponding electromagnetic excitations. This was achieved by building a special light-scattering apparatus, and seeking the best possible quantitative agreement between the acquired data and accurate electromagnetic models developed to simulate scattering in this 2D + 1 dielectric geometry.

In Chapter 5, the results of linear white light spectroscopy experiments conducted using the light-scattering apparatus are presented and rigorously compared with simulations based on the Green's function formalism described in Chapter 2. First, the

theoretical and experimental results from two basic structures are used to derive a comprehensive understanding of electromagnetic excitations associated with 2D textured planar waveguides. Section 5.1.1 discusses the dispersion and polarizations of leaky modes in a textured planar waveguide with a simple square lattice of air holes. [21] This work represents the most thorough quantitative description of the low-lying resonant photonic bands of high index-contrast textured planar waveguides to date. This qualitative and quantitative analysis of square lattices was extended to high index-contrast triangular lattices, and experimentally confirmed, as described in Section 5.1.2.

Chapter 5 also describes two examples of 2D textured planar waveguides engineered with specific applications in mind. The first example, in Section 5.2.1, addresses the use of resonant coupling to effect a polarization insensitive notch filter in low index-contrast, 2D textured polymer waveguides. This section provides the first quantitative study of the scattering properties of these structures which were fabricated using a direct-write holographic technique in a special azo-polymer by Paul Rochon's group at the Royal Military College of Canada. The second example, discussed in Section 5.2.2, experimentally and theoretically demonstrates how a high index-contrast 2D textured planar waveguide can be engineered to possess a band that is effectively *flat* along the entire Γ–X direction of a 2D square Brillouin zone. Flat bands have been theoretically shown to significantly enhance certain non-linear optical conversion processes in bulk photonic crystals.

In the final section of Chapter 5, a novel diffraction measurement technique, developed

by the author for this research, is explored via the characterization of three textured planar waveguides with defect superlattices. The efficacy of this method for probing the band structure of high and low dispersion modes is evaluated. It is shown how this background-free measurement technique can be used to further the quantitative analysis of textured planar waveguides. This section also presents and analyzes the engineering of a localized defect mode in the first order gap to realize a design for an angle and polarization insensitive notch filter.

Chapter 2

Linear Light Scattering Spectroscopy of Textured Planar Waveguides

This chapter introduces some of the key physics of textured planar waveguides, describes the spectroscopic techniques used to probe the band structure of these waveguides, and discusses a Green's function model used to simulate the influence of periodic 2D texturing in planar waveguides.

2.1 Background

Light traveling through a textured planar waveguide experiences dispersion, much like electrons traveling through a semiconductor crystal. Just as electrons in a semiconductor experience a periodic *electrical* potential from each atom in the crystal lattice, the photons in a textured planar waveguide experience a periodic *photonic* potential. This section presents some of the key characteristics associated with the dispersion of photons traveling through a textured planar waveguide.

First, untextured waveguides are reviewed. Next, the polarization and dispersion properties of 2D textured waveguides are discussed for square and triangular lattices. Then, the effect of a defect superlattice on the band structure is described.

2.1.1 Untextured Planar Waveguides

A planar waveguide is a structure that uses total internal reflection between the core and cladding material to confine light in the plane of propagation. The physical characteristics of the waveguide determine which modes of light are allowed to propagate. Solving Maxwell's equations for an asymmetric[1] waveguide yields independent solutions for transverse electric (TE) and transverse magnetic (TM) polarized modes that are bound to the waveguide. A TE mode's *electric* field is oriented in the plane of propagation, and is thus transverse to the direction of propagation, whereas a TM mode has its *magnetic* field oriented in-plane, transverse to the direction of propagation. Plotting the solutions to the scaler wave equation as a function of in-plane wavevector ($K_{||}$) on a dispersion diagram produces a graph like the one shown in Figure 2.1. Note that there are an infinite number of discrete modes, but only the two lowest modes are shown. The lowest energy mode is always TE.

Also plotted on the dispersion diagram in Figure 2.1 are three straight lines that represent the dispersion of light in air, in bulk core material, and in bulk cladding material. The slope of each of these lines is proportional to the reciprocal of the index of refraction

[1] An asymmetric waveguide is one in which the cladding material on top of the core has a different index of refraction than the cladding on the bottom.

in the corresponding material. These lines are referred to as *light lines*. These light lines divide the graph into four regions. Below the core light line is a forbidden region where no electromagnetic modes can exist. Above the air light line is a region where a continuum of radiation modes exist. The modes in this region represent radiation which is multiply reflected but otherwise passes *through* the waveguide. Between the air light line and the substrate light line is a region where cladding modes occur. These cladding modes can be thought of as passing back and forth between the cladding material and the waveguide core, but not passing from the core into the air due to total internal reflection. The final region, which occurs between the substrate light line and the core light line, is where the bound or "slab" modes occur. Modes in this region experience total internal reflection at both the core-air interface and the core-cladding interface. Schematic diagrams of the electric field profile for modes in each of these regions are shown in this figure.

When a planar waveguide is periodically textured, the dispersion of guided light is altered, analogous to the way in which the dispersion of free electrons is altered by a semiconductor lattice. The next section discusses how texturing changes the properties of a planar waveguide, and describes in detail two of the many possible lattice configurations: square and triangle.

2.1.2 2D Simple Lattices

A 2D simple (no defects) lattice has a two-dimensional unit cell possessing a single lattice site. When a 2D simple lattice is etched into the surface of a planar waveguide, the

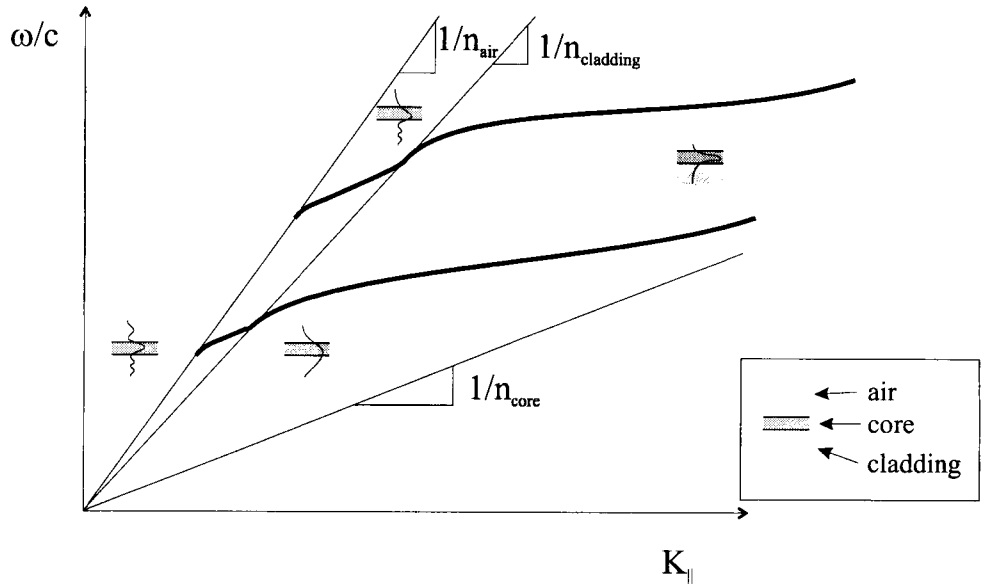

Figure 2.1: Schematic dispersion diagram for an untextured, asymmetric planar waveguide. The two lowest energy modes are shown as bold lines. The air, substrate and cladding light lines are shown. Schematic diagrams inset in each region indicate the electric field profile for modes in that region.

periodic holes form a periodic dielectric structure which changes the dispersion characteristics of the waveguide. Specifically, when light propagates in a planar waveguide with a 2D periodic lattice, the light Bragg scatters off the periodic dielectric grating, causing a renormalization of the slab modes. Per Bloch's theorem, the dispersion of the resultant modes represented on a dispersion diagram can be folded into the first Brillouin zone, allowing the use of the reduced zone scheme. As depicted in the schematic diagram of zone-folding shown in Figure 2.2, the band is folded back at the edge of the Brillouin zone ($K_{||} = K_g/2$, where K_g is the grating vector.). When the bands are zone-folded, portions of them fall above the air light line, represented by the gray area in the schematic. Modes in this region are considered "leaky" since they have Fourier components which radiate

out of the waveguide. The modes below the air light line are still bound to the waveguide and have no radiating component. At the first Brillouin zone boundaries (2D), the normal slope of the dispersion (i.e. group velocity) goes to zero, which is the result of the Bragg scattering creating standing waves and opening gaps in the allowed frequencies. When the gaps are sufficiently large, it is possible for a smaller gap to exist within some range of frequencies everywhere on the first Brillouin zone boundary. In this case there is a "complete pseudo-gap" for that particular set of renormalized slab modes.

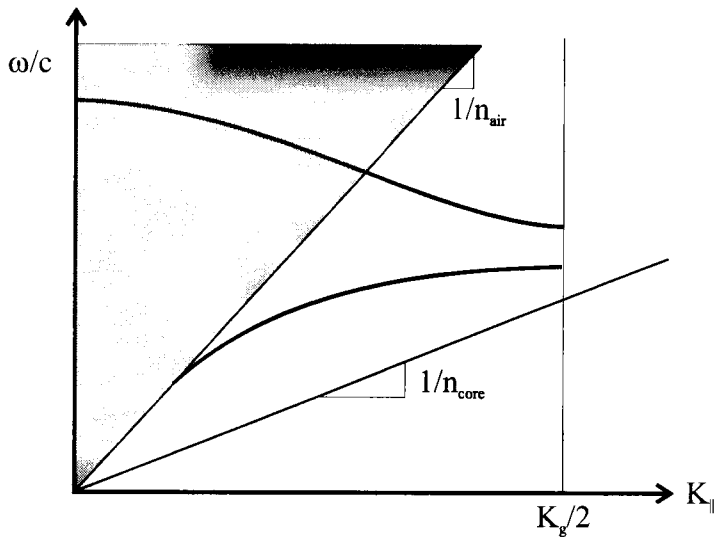

Figure 2.2: Schematic of 1D zone-folding.

The size of the gaps at zone edge, and whether or not a gap is complete, depend upon the grating materials and lattice configuration of a 2D textured planar waveguide. The size of a gap at zone edge is determined by the difference in energy between the two standing wave solutions which occur at this point. One standing wave has nodes located in the dielectric, while the other has nodes located in the holes which comprise

the grating. The higher the index-contrast is between the grating layer and the material comprising the grating (air in this case), the larger the gap will be. [12] The size of the gap is also affected by the filling fraction[2] of the grating. Smaller first order gaps occur when the air filling fraction is near zero or one; the first order gaps become proportionally larger as the filling fraction approaches 50%. The more the grating perturbs the modes, the larger the gaps will be. Whether or not a gap is a *complete* pseudo-gap is related to the size of the gaps at the zone boundaries and the symmetry of the lattice configuration. The more symmetric the lattice, and the larger the gap, the more likely it is that there will be a complete pseudo-gap for all directions.

When a plane wave is incident on the surface of a textured planar waveguide with a well-defined in-plane wavevector, $\vec{K}_i$, the incident field can be written as

$$\vec{E}_i(\vec{K}_i; z) = \vec{E}_o e^{-iw_o z} e^{i\vec{K}_i \cdot \vec{\rho}} \tag{2.1}$$

where $w_o = \sqrt{\tilde{\omega}^2 - K_i^2}$, $\tilde{\omega} = \omega/c$, and $\vec{\rho} = x\hat{x} + y\hat{y}$. [5] The incident plane wave may have any polarization. If the grating has a well-defined 2D periodic texture represented by reciprocal lattice vectors, $\{\vec{G}_m\}$, the electric field in the grating can be conveniently represented as [5]

$$\vec{E}(\vec{\rho}, z) = \sum_m \vec{E}(\vec{K}_i + \vec{G}_m; z) e^{i(\vec{K}_i + \vec{G}_m)\cdot\vec{\rho}}. \tag{2.2}$$

These plane waves, with well-defined frequency and in-plane wavevector, $\omega, K_{||}$, are useful to determine the dispersion of the leaky modes attached to textured waveguides,

[2]Filling fraction is defined as the area of the grating material in a unit cell divided by the area of the unit cell.

both experimentally and through modelling. For some general $\omega, K_{||}$, the non-specular ($\vec{G} \neq 0$) field components in Equation 2.2 will be small. However, when $\omega, K_{||}$ coincides with one of the allowed leaky eigenstates of the 2D textured waveguide, one or more of the scattered field components in Equation 2.2 becomes large. For the low-lying bands studied throughout this thesis, the general dispersion and polarization properties can often be described using a small sub-set of the Fourier components of Equation 2.2. It is usually sufficient to consider the zeroth order (specular) component, and one or two sets of nearest neighbors. The zeroth order component is usually small, but is essential because it is the one responsible for coupling light into and out of the guided modes of the waveguide.

The pure kinematic effects of 2D texture on the dispersion and polarization properties of the leaky modes are presented in this section, for both square and triangular lattice types. Only s-polarized scattered fields are considered in Equation 2.2. For weak texture, and under resonant excitation conditions, these basically represent TE-polarized slab modes. More generally, the scattered components in a 2D textured planar waveguide are both s- and p-polarized, corresponding respectively and approximately to TE and TM polarized slab modes. However, for many of the GaAs-based structures examined here, the TE–TM separation is large enough to effectively decouple the two.

When a 2D scattering potential is weak, the main effect the grating has on the extended 2D dispersion of the waveguide is to zone-fold the slab modes into the first (2D) Brillouin zone, as illustrated in Figure 2.3. The general characteristics and shape of the

dispersion in the limit of weak texturing can be understood by considering that the main effect of the grating is then merely to introduce new in-plane momentum components to the incident field, thus affording it the opportunity to excite what are effectively pure TE slab modes with wavevectors given by $\vec{K}_i + \{\vec{G}_m\}$.

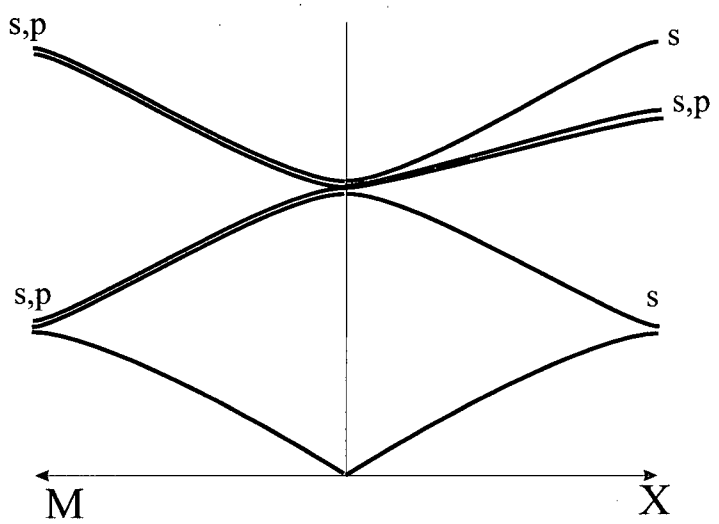

Figure 2.3: Schematic dispersion diagram for a thin planar waveguide textured with a 2D square lattice. The 's' and 'p' designations refer to polarizations of the photonic eigenstates, as discussed in the text.

Figure 2.4 is a momentum space diagram of the nine dominant Fourier components of the dielectric scattering potential for a simple square lattice. The reciprocal-lattice vectors of a square lattice are given by $\vec{G} = iK_g\hat{x} + jK_g\hat{y}$ where $K_g = 1/\Lambda$, i and j are positive integers including zero. Figure 2.4(a) corresponds to the incident plane-wavevector, $\vec{K}_i$, aligned along the X symmetry direction. Figure 2.4(b) corresponds to the incident plane-wavevector, $\vec{K}_i$, aligned along the M symmetry direction. For both of these figures, the central point represents the zeroth order component of the scattering

potential, and $\vec{K}_i$ is represented by the small dotted vectors. The in-plane wavevectors of the TE field components and their corresponding polarizations are represented by the solid arrows and gray arrows respectively.[3]

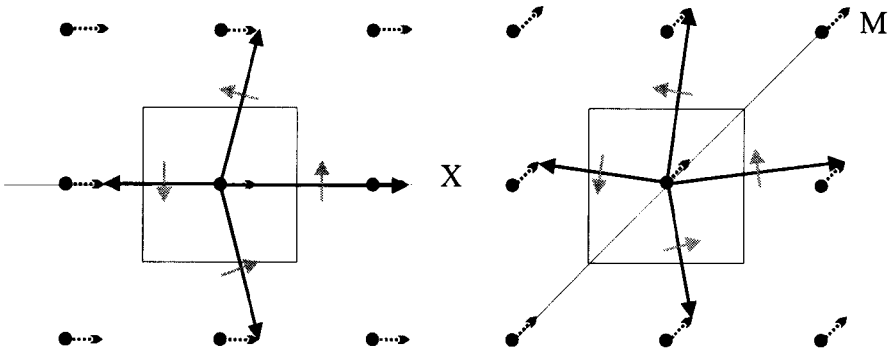

Figure 2.4: Momentum space diagram for a square lattice. Figure (a) represents incident radiation along the X symmetry direction. Figure (b) represents incident radiation along the M symmetry direction. The dots represent the Fourier components of the dielectric scattering potential. The small dotted vectors represent the in-plane wavevector of the incident radiation. The large vectors represent the in-plane field vectors which result when the scattering potential adds momentum to the incident field. The polarization of each field component is represented by the small gray vectors.

If the (isotropic) dispersion of the underlying TE slab modes is denoted by $\omega(K_{||})$, the zone-folded dispersion expected for a very weak 2D texture with square symmetry can be understood as follows. For a given incident wavevector $\vec{K}_i$, the Fourier components of the dielectric texture scatter the incident field into a discrete set of scattered states with in plane wavevectors $\vec{K}_i + \vec{G}_m$. When the incident frequency corresponds to one of the slab mode frequencies at these in-plane wavevectors, $\omega(|\vec{K}_i + \vec{G}_m|)$, the scattering will be

[3]A similar diagram can be made for the TM field components and their corresponding polarization vectors.

resonantly enhanced, corresponding to the excitation of one of the localized excitations of the 2D textured slab. For the four smallest reciprocal lattice vectors with magnitude K_g, these resonantly excited slab modes disperse with $\vec{K}_i$, as illustrated schematically in Figure 2.3. In particular the mode at $\omega(|K_i\hat{x} + K_g\hat{x}|)$ increases monotonically as $\vec{K}_i$ increases along the X direction. This dispersive mode corresponds to the highest band along the X direction in Figure 2.3. The mode excited at $\omega(|K_i\hat{x} - K_g\hat{x}|)$ disperses down in energy as $\vec{K}_i$ increases in the X direction, while the modes at $\omega(|K_i\hat{x} \pm K_g\hat{y}|)$ disperse upward, but at a moderate rate compared to the other two modes illustrated in Figure 2.3.

The polarization labels on the bands shown in Figure 2.3 can be understood using the following symmetry argument. The polarization (s, p or elliptical) of the radiation reflected from the surface for a given incident plane wave at $\vec{K}_i$ is determined by the Fourier component of the polarization density in the grating at the same $\vec{K}_i$. From the theory described below (Section 2.2), for a thin textured grating, this component of the polarization density in the grating can be expressed as [5]

$$\vec{P}(\vec{K}_i) = \sum_m \chi(\vec{G}_m)\vec{E}(\vec{K}_i - \vec{G}_m) \tag{2.3}$$

Under resonant excitation conditions, one or two Fourier components of the field corresponding to the resonantly excited TE slab modes will dominate the scattered field everywhere except at $\vec{K}_i$=0. For the upward dispersing mode in Figure 2.3, this corresponds to a TE slab mode at $\vec{K}_i + K_g\hat{x}$, which is polarized in the $\hat{y}$ direction. From Equation 2.3 above, the polarization density at $\vec{K}_i$ is then polarized in the $\hat{y}$ direction,

thus generating an s-polarized radiation field in the upper half space. The same is true for the rapidly downward dispersing branch in Figure 2.3. Things are slightly more complicated for the moderately dispersing branches because from symmetry, the incident field must excite either symmetric or antisymmetric combinations of these slab modes (degenerate in the absence of texture) at $\vec{K}_i \pm K_g\hat{y}$. From the polarization vectors shown in Figure 2.4, a symmetric superposition of these scattered slab modes will add as shown in Equation 2.3 to yield a polarization density at $\vec{K}_i$ oriented along the $\hat{y}$ direction, corresponding again to s-polarized radiation in the upper half space. However, the antisymmetric combination leads to a polarization density oriented parallel to $\vec{K}_i$, which can only lead to p-polarized radiation in the upper half space, hence the polarization labels in Figure 2.3. It follows that there are 2 s- and 2 p-polarized modes, one each dispersing up and down, when $\vec{K}_i$ is oriented along the M direction. If $\vec{K}_i$ does not lie in a plane with mirror symmetry, the modes are, in general, elliptically polarized, and cannot be labelled as pure s- or p-polarized.

An analysis similar to the one just presented can be done to determine the dispersion and polarization characteristics of the modes attached to a planar waveguide textured with a triangular lattice. Momentum space diagrams for a triangular lattice are shown in Figure 2.5. Figure 2.5(a) shows an incident wavevector aligned along the M symmetry direction while Figure 2.5(b) shows an incident wavevector aligned along the K symmetry direction. Since the group of "nearest neighbors" consists of six Fourier components, there are six bands making up the second order TE-like gap. The dispersion and polarizations

of these six bands are shown in Figure 2.6. In the M direction there are four s-polarized bands: two dispersing up in energy and two dispersing down in energy. In addition there are two p-polarized bands: one dispersing up in energy and one dispersing down in energy. In the K direction there are two s- and two p-polarized bands which disperse up in energy, and one s- and one p-polarized bands which disperse down in energy.

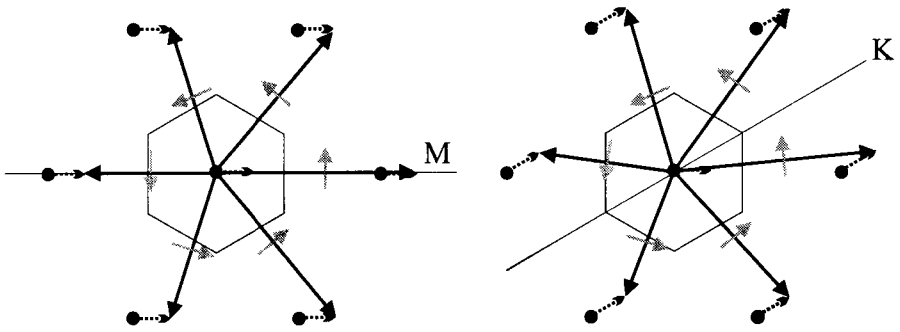

Figure 2.5: Momentum space diagram for a triangular lattice. Figure (a) represents incident radiation along the M symmetry direction. Figure (b) represents incident radiation along the K symmetry direction. The dots represent the Fourier components of the dielectric scattering potential. The small dotted vectors represent the in-plane wavevector of the incident radiation. The large vectors represent the in-plane field vectors which result when the scattering potential adds momentum to the incident field. The polarization of each field component are represented by the small gray vectors.

One of the significant findings of this thesis work was that the dispersion and polarization properties of the low-lying leaky bands in *strongly* textured waveguides can largely be interpreted by combining this kinematic picture with non-perturbative, strong coupling of these basic bands near zone boundaries, and near anticrossings that may occur anywhere in the first Brillouin zone.

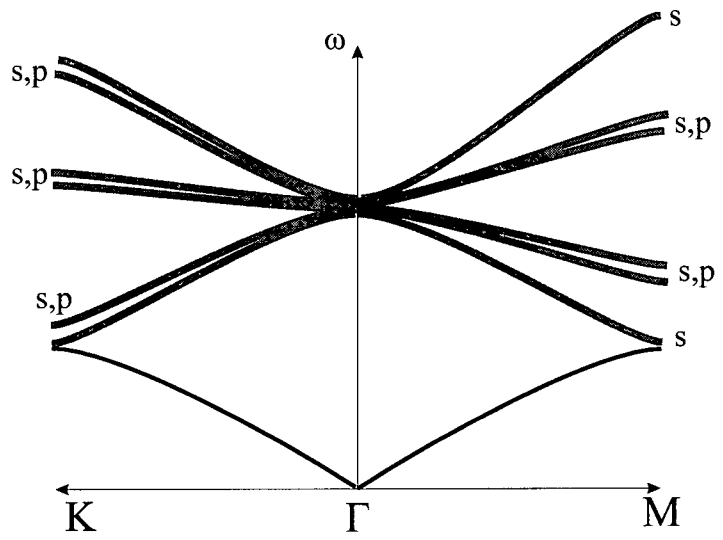

Figure 2.6: Schematic dispersion diagram for a thin planar waveguide textured with a 2D triangular lattice.

2.1.3 Defect Superlattices

As discussed previously, textured planar waveguides made with gratings of simple lattices can affect the propagation of photons, which is akin to the atoms in the crystal lattice of a semiconductor affecting the propagation of electrons. Continuing the analogy to semiconductors, adding defects to the lattice in a planar waveguide can allow modes to occur in the photonic bandgap, which is similar to adding impurities to a semiconductor that give rise to states within the electronic bandgap. This section discusses the incorporation of a defect superlattice into a textured planar waveguide.

When a defect superlattice is incorporated into a textured planar waveguide, the unit cell for the lattice increases to include the defect. For example, for a defect superlattice in a 1D grating that leaves out every fifth lattice point, the unit cell would be five times

larger than the unit cell of the "base" lattice. The reciprocal lattice vectors for the defect superlattice are 1/5 the length of that of the base lattice ($K_g^D = \frac{1}{5}K_g^0$). Adding the defect decreases the Brillouin zone to 1/5 the size that it is for the non-defect lattice, resulting in more frequent zone-folds. Figure 2.7 illustrates these changes by superimposing a dispersion diagram for a defect superlattice on a dispersion diagram for a non-defect lattice: the solid lines represent the band structure for a non-defect base lattice; the dashed lines represent the band structure for the identical lattice, with the exception that a defect superlattice has been incorporated. This figure shows the decrease in size of the Brillouin zone and the increase in zone-folds. Figure 2.8 shows the dispersion for a waveguide with a defect superlattice superimposed on a dispersion diagram for a base lattice that produces a much larger pseudo-gap than in the previous example. In this case, the incorporation of a defect superlattice does more than merely increase the zone-folding: it introduces a mode into this large pseudo-gap. While these illustrations are for 1D textured planar waveguides, incorporating a defect superlattice in a 2D textured planar waveguide produces qualitatively similar results, as discussed below in Section 5.3.3.

When a 2D textured planar waveguide with a defect superlattice produces a mode in the first order pseudo-gap, only light of that frequency is allowed to propagate while all other frequencies of light in the gap are forbidden to propagate. This effect can allow for the localization and channeling of light in the waveguide [14,40], making it useful for many applications. Lasers have been designed and demonstrated using localization of light in optical microcavities located at defects in photonic crystal lattices. [22] Additionally,

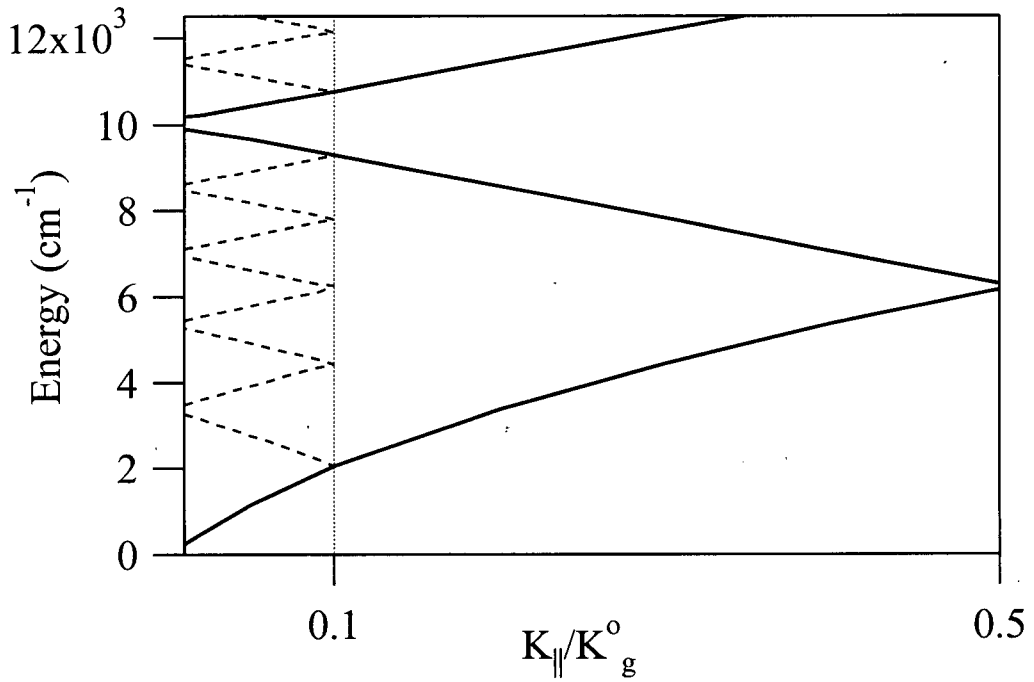

Figure 2.7: Band structure for a thin GaAs planar waveguide with 1D defect superlattice of air "holes." The air filling fraction of the texturing is 2.5%. The solid lines show the dispersion for this structure without the superlattice, while the dashed ones represent the modified dispersion of this structure when every fifth "hole" is omitted.

analysis has been done on channeling light via 1D arrays of defect sites in a photonic crystal lattice. [2]

This thesis seeks to quantitatively characterize the electromagnetic excitations attached to textured planar waveguides with and without defect superlattices. A rigorous computer model and white light spectroscopy are used in conjunction to study the electromagnetic response of these structures to radiation incident from the top half space. The computer code and the spectroscopic techniques used are described in the following sections.

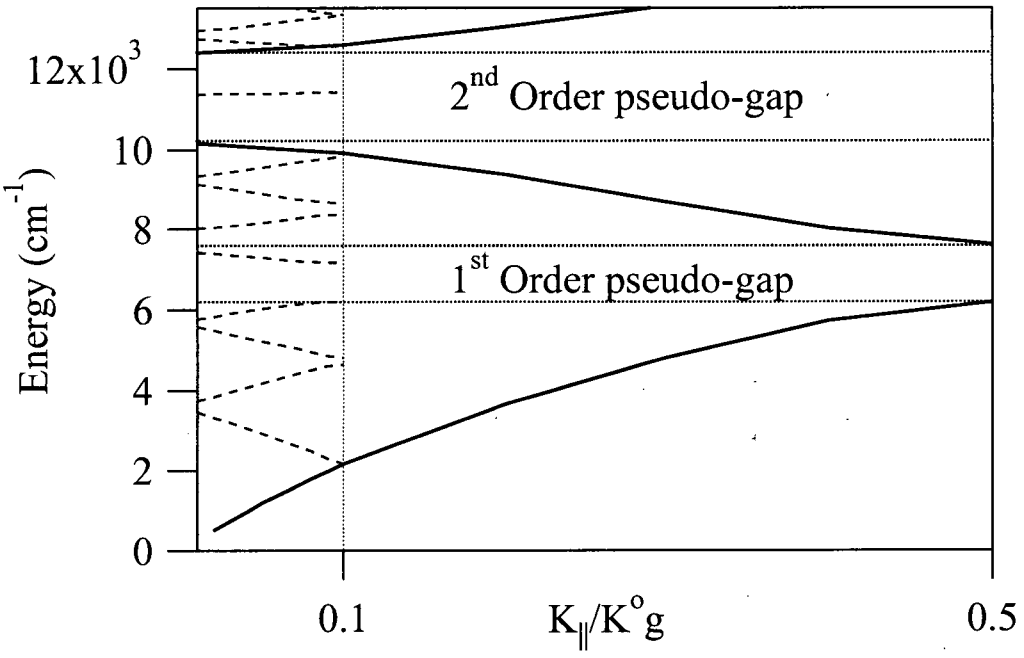

Figure 2.8: Band structure for a thin GaAs planar waveguide with a 1D defect superlattice of air "holes". The air filling fraction of the texturing is 25%. The solid lines show the dispersion for this structure without the superlattice, while the dashed ones represent the modified dispersion of this structure when every fifth "hole" is omitted. K_g° is the grating vector of the "base" lattice. Notice that in this case the superlattice does more than simply zone-fold the base lattice modes: it introduces defect modes in both the first- and second-order pseudo-gaps.

2.2 Green's Function Model

In order to explore the photonic band structure associated with textured planar waveguides, a computer code was used to model the waveguide's response to electromagnetic radiation. The results of this computer code have been validated by comparison with other models [21] as well as by comparison with experimental results [20]. This code mathematically models the electric fields associated with textured planar waveguides

by implementing a Green's function technique to solve Maxwell's equations. For the modeling of defect superlattices reported in this thesis, modifications were made to the code which are discussed below.

The computer code is designed to accurately model the scattering of light incident on a textured planar waveguide, such as the one depicted schematically in Figure 2.9. The waveguide depicted has four layers: substrate, lower cladding, core and upper cladding. The code has the capability to model any number of layers, including semi-infinite upper and lower layers. The code is also capable of modeling any angle of incident light (θ and ϕ) on the surface of the waveguide.

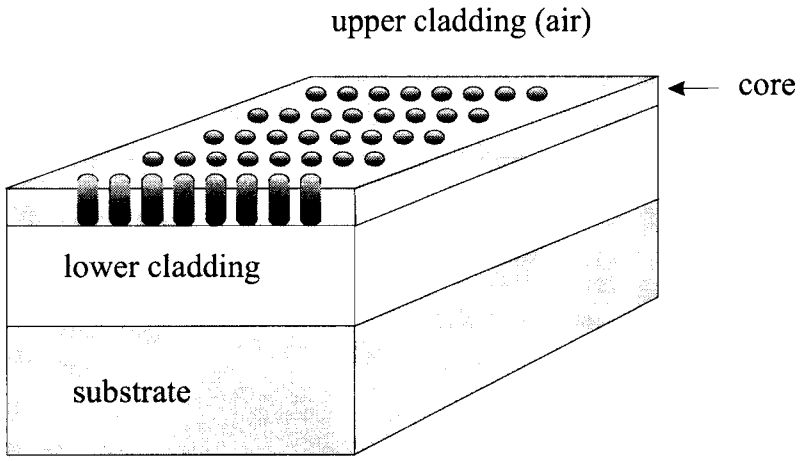

Figure 2.9: Schematic diagram of a textured planar waveguide.

The code implements a solution of Maxwell's equations in the waveguide geometry by taking the periodic polarization density in the textured region as the driving term for a Green's function. [5] The self-consistent solution for a single Fourier component of the

field in the grating is given by

$$\vec{E}(\tilde{\omega}, \vec{K}_n, z) = \vec{E}^{hom}(\tilde{\omega}, \vec{K}_n, z) + \int dz' \overleftrightarrow{g}(\vec{K}_n, \tilde{\omega}, z, z') \sum_m \overleftrightarrow{\chi}^{(1)}_{nm}(-\tilde{\omega}, \tilde{\omega}) \vec{E}(\tilde{\omega}, \vec{K}_m, z') \quad (2.4)$$

when a plane wave with frequency $\tilde{\omega} = \omega/c$ and in-plane wavevector $\vec{K}_i$, is incident from the upper half space, and where $\vec{K}_m = \vec{K}_i - \vec{G}_m$ is the in-plane wavevector of the Fourier components of the field, and $\vec{G}_m$ are the reciprocal lattice vectors. [5] The periodic susceptibility is represented as a Fourier series with coefficients $\overleftrightarrow{\chi}_{nm}$ that couple the various Fourier components of the scattered field. The infinite set of vector integral equations implied in Equation 2.4 is reduced to 3N scaler algebraic equations by truncating the Fourier series describing the in-plane components of the field at N. This also requires that the textured region is sufficiently thin so that the fields can be taken as constant over its extent, thus eliminating the integral over dz' in Equation 2.4. Gratings that are too thick for this assumption can be modeled by dividing them into thinner regions that each satisfy the constant field approximation. This technique is described in detail for a single layer structure in [5].

In the original code, the reciprocal lattice vectors as well as the Fourier coefficients were hand-coded for each lattice investigated. This was sufficient when modeling a simple lattice (i.e. one that has a single lattice point in the unit cell), which typically requires fewer than ten Fourier coefficients to properly model the low-lying bands.

The calculations for defect superlattices can require more than 200 Fourier coefficients,

making hand-coding impractical and inefficient. To facilitate simulations of defect superlattices, subroutines were written which calculate the reciprocal lattice vectors and Fourier coefficients. The Fourier coefficients which are used by the code to represent the periodic polarization in the grating layer are normalized to range between 0 and 1, where 0 represents no hole and 1 represents a hole. For a simple lattice described by

$$f(\vec{r}) = \sum_{nm} C_{nm} e^{i \vec{G}_{nm} \cdot \vec{\rho}} \tag{2.5}$$

the Fourier coefficients, C_{nm}, are given by

$$C_{nm} = \frac{4}{A_{cell}} \int_0^b dx \sqrt{b^2 - x^2} \cos(G_{nm} x) \quad = \quad \frac{2}{A_{cell}} \frac{b\pi}{G_{nm}} J_1(b\, G_{nm}) \tag{2.6}$$

where

$$G_{nm} = G_0 \sqrt{n^2 + m^2 - 2nm \cos(\pi - \alpha)} \tag{2.7}$$

and where b is the radius of the holes, n and m are the base lattice unit vectors and α is the angle between them. G_{nm} is the reciprocal lattice vector.

To generate a Fourier series for a defect superlattice, first the above equations are used to generate a Fourier series which describes the "base" simple (non-defect) lattice, (a), shown in a real-space plot in Figure 2.10. Next, a Fourier series is generated which represents the location and size of those holes to be omitted to form the defect, (b). Finally, the Fourier series for (b) is subtracted from the Fourier series for (a) producing the Fourier series for the defect superlattice (c), that for this example omits every fifth hole in the base lattice pattern. Optionally, an additional Fourier series can be generated

in order to add holes of a selected radius into the "empty" superlattice spaces, resulting in a defect comprised of holes which are smaller or larger than those of the base lattice, rather than a defect comprised of omitted holes.

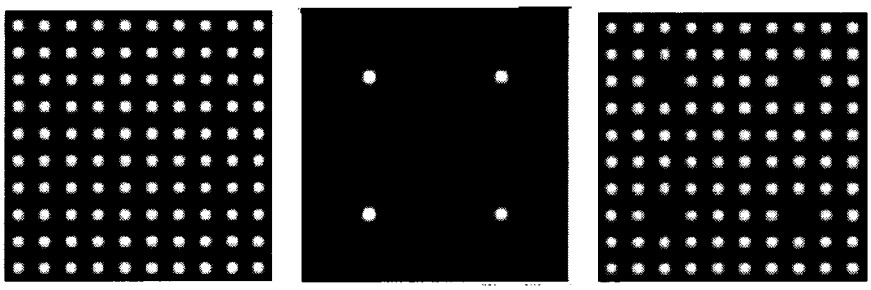

(a) (b) (c)

Figure 2.10: Graphical representation of Fourier coefficient generation technique. (a) represents the base lattice. (b) represents the defect location. (c) is the resulting defect superlattice. (c)=(a)-(b).

2.3 Spectroscopy

In conjunction with the Green's function code, white light spectroscopy is used to characterize the textured planar waveguides. White light spectroscopy consists of illuminating the waveguide with a broadband source at a well-defined angle of incidence, and using a spectrometer to analyze the scattering spectrum to infer the band structure. For the research presented here, two types of spectroscopic technique are used: a well-documented specular measurement technique, and a novel diffraction measurement technique developed by the author.

2.3.1 Specular Measurement Technique

To characterize the textured planar waveguides for this thesis, the band structure was mapped and in some cases the lifetimes were measured. A specular measurement technique was used to accomplish this for the waveguides with 2D simple lattices. This technique involves shining white light on the surface of a textured planar waveguide at a well-defined angle of incidence and then analyzing the spectra of the specularly reflected light. This technique provides a straight-forward means for mapping the leaky photonic modes of textured planar waveguides.

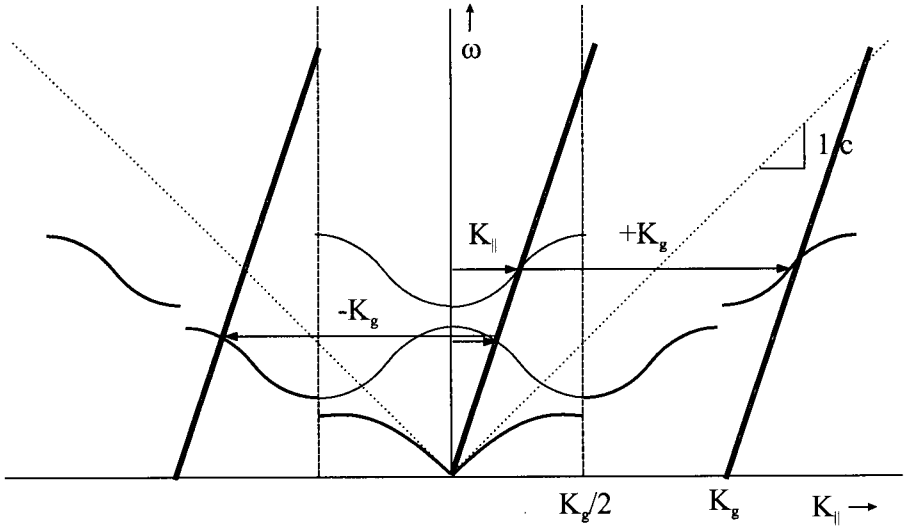

Figure 2.11: Schematic dispersion diagram for a 1D textured waveguide. Bold lines indicate locations probed with the specular measurement technique.

When white light is incident on the surface of a textured planar waveguide at a well-defined angle of incidence, each energy, ω, of the incident light corresponds to a specific in-plane wavevector, $K_{||}$, according to the relation $K_{||} = \omega \sin\theta$. Generalizing the kinematic arguments given above, coupling into a guided mode eigenstate will occur

whenever $K_{||} \pm nK_g$ stimulates a mode. Here n is any integer and K_g is the grating vector. Figure 2.11 shows a zone-folded schematic diagram of the dispersion for a waveguide with a 1D textured layer clad by air on top and bottom. The dotted line represents the air light line. Any modes which are above the air light line (when folded into the first Brillouin zone) are accessible with this specular measurement technique. The solid lines represent the parameter space probed with this technique for a specific angle of incidence. At each point where this line intersects a band, a feature is detected in the specular reflectivity spectrum. A simulated example of the spectra that can be obtained with this technique is shown in Figure 2.12. The narrow features are Fano-resonances which are a result of coupling into guided modes of the waveguide. A mathematical fitting technique can be used to extract the modes' positions and lifetimes from this type of spectra. [21] By recording and analyzing the spectra for multiple angles of incidence, the band structure of the waveguide's photonic modes can be mapped and the lifetimes can be measured.

2.3.2 Diffraction Measurement Technique

The specular measurement technique works well for characterizing the band structure of many textured planar waveguides, but the mathematical fitting technique used to extract the mode energy and linewidth from the specular background is not well-suited for use when the modes are closely spaced. If the modes could be observed free of the specular background, the characteristics could be analyzed without complicated mathematical fitting. The author developed a background-free probe technique based on the light

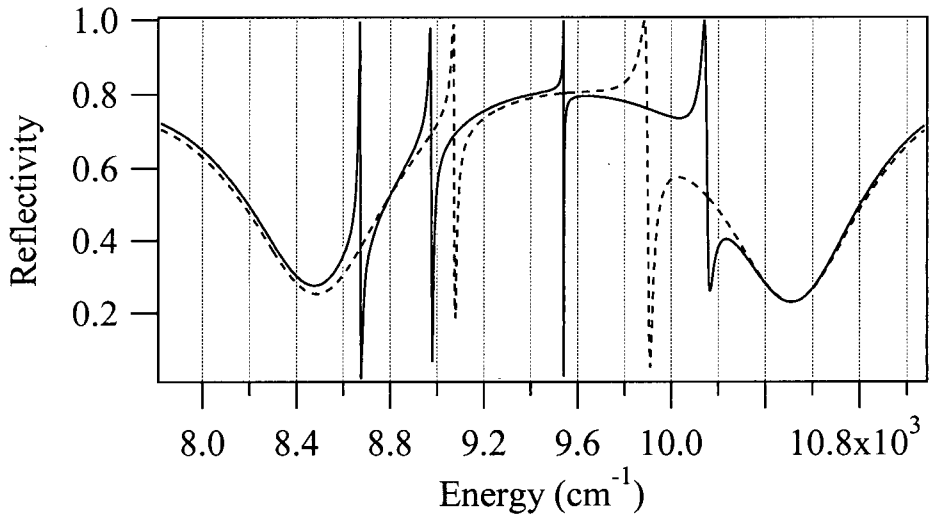

Figure 2.12: Representative reflectivity spectra from a textured planar waveguide with a square lattice of holes. Solid lines represent s-polarization; dashed lines represent p-polarization. The narrow features are Fano-resonances which are a result of coupling into guided modes of the waveguide.

diffracted, rather than reflected, from samples containing a superlattice of defects. This diffraction measurement technique is described below.

To implement this new diffraction measurement technique, light at a particular angle of incidence stimulates a guided mode by adding an integer multiple of defect lattice grating vectors to the parallel component of the incident light. This is represented by the equation $K = K_{||} \pm nK_g^D$. The light is scattered out of the waveguide by adding or subtracting an integer multiple of defect lattice grating vectors from the guided mode. While the specular technique uses the same number of grating vectors to stimulate the mode as to scatter out of the mode, the diffraction technique uses an unequal number.

This diffraction measurement technique is shown schematically in Figure 2.13. The parameter space probed by the incident beam is represented by the bold line. This

schematic corresponds to a 1D lattice with a defect located at every fifth site. In this case the defect lattice grating vector is 1/5 the size of the base lattice grating vector. Coupling to the guided mode results by adding or subtracting 5 *defect lattice* grating vectors. The light now scatters out of the waveguide not only in the specular direction, but also in any of the directions associated with the lines parallel to the bold line labeled '0' on Figure 2.13. The location of the $-K_g^D$ diffracted order is indicated on the diagram by a circle.

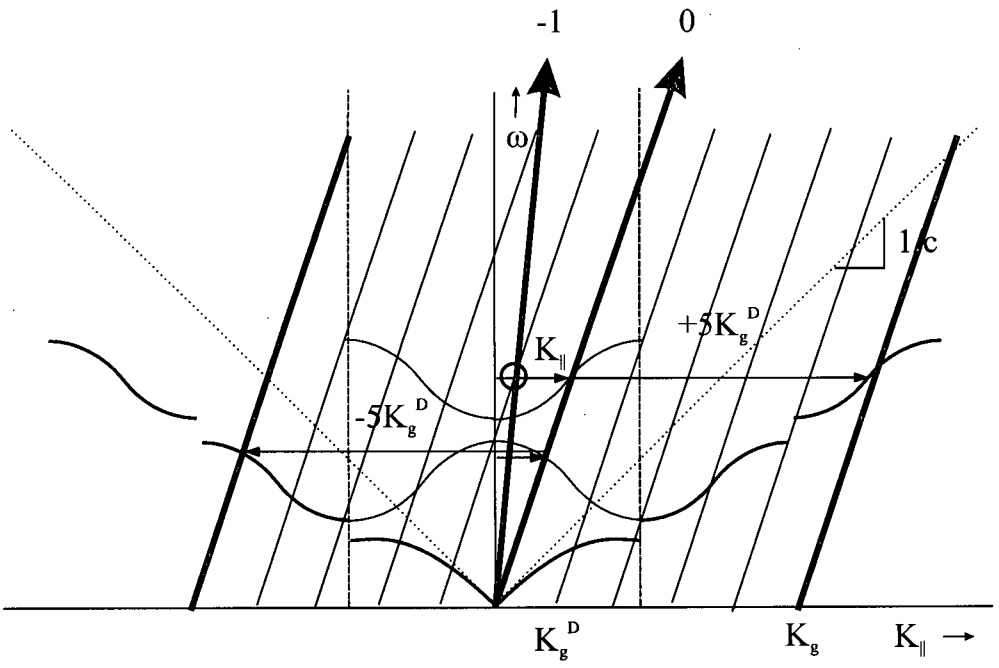

Figure 2.13: Schematic dispersion for the diffraction probing method. The direction of the specular reflection is labeled 0, while the direction of the $-K_g^D$ diffracted order is labeled -1.

Theoretically, the diffraction technique should allow observation of modes above the light line free from specular background. Significantly, it could also allow for the viewing of modes from the base lattice which are below the light line. Conventional methods for

probing modes below the light line involve elaborate techniques for getting light into and out of the waveguide. The diffraction measurement technique offers the potential to map these modes by simply illuminating them from the upper half space, allowing analysis of the scattered light which reveals the band structure of the bound modes.

To investigate whether the diffraction measurement technique has these capabilities, the Green's function code was used to simulate light diffracting from a textured planar waveguide with a defect superlattice. The simulation was done for a free-standing GaAs waveguide, 80 nm thick, with a square lattice of circular holes completely penetrating the core, spaced 400 nm apart with a radius of 110 nm. The defect superlattice was created by omitting every fifth hole in the x and y directions. Figure 2.14 shows a simulation of the first order diffraction which results when broadband light is incident normal to the surface of this waveguide. It is readily apparent that the modes in this spectra are free of the specular background. It is not obvious, however, where these modes originate. If these modes originate below the light line of the base lattice, then it should be possible to reproduce their energies by looking at the dispersion of the defect-free base lattice, as discussed below.

A momentum space diagram for the waveguide containing the superlattice (Figure 2.15) illustrates which specific in-plane wavevectors occur within the reduced zone of the base lattice. In this diagram, the large gray dots represent the reciprocal lattice vectors of the base (non-defect) lattice. The square identifies the first Brillouin zone of this base lattice, and the triangle delineates the reduced zone. The small gray dots represent the

reciprocal lattice vectors that are introduced by the defect superlattice. The dark dots with the small squares around them represent reciprocal lattice vectors from the defect lattice occurring within the reduced zone of the base lattice. When light is incident normal to the surface of the waveguide, the in-plane wavevector of the incident radiation is zero, so the in-plane wavevectors of the field scattered by the defect superlattice are just given by the reciprocal lattice vectors of the defect superlattice. Figure 2.15 shows that there are five distinct in-plane wavevectors (dark dots) where the defect superlattice samples the first Brillouin zone of the base lattice.

Figure 2.16 shows the calculated specular reflectivity spectra from the defect-free base lattice at these five wavevectors. Poles in these spectra represent true bound modes that lie below the lightline in the base lattice band structure. Labels in Figures 2.14 and 2.16 relate the peaks observed in the background-free diffraction spectra from the defect superlattice sample with the poles observed in the reflectivity spectra at the relevant in-plane wavevectors of the base lattice. This confirms that, theoretically, the use of defect superlattices does offer the ability to probe the dispersion of true bound modes that exist below the light line in the defect-free Brillouin zone.

This diffraction measurement technique can be used whenever the energy of the mode to be detected radiates a diffracted signal above the light line. Any lattice that has periodic spacing longer than the wavelength of the probe light will have at least one diffracted order. In waveguides where a diffracted signal does not exist above the light line, a defect superlattice can be incorporated to create one. Textured planar waveguides

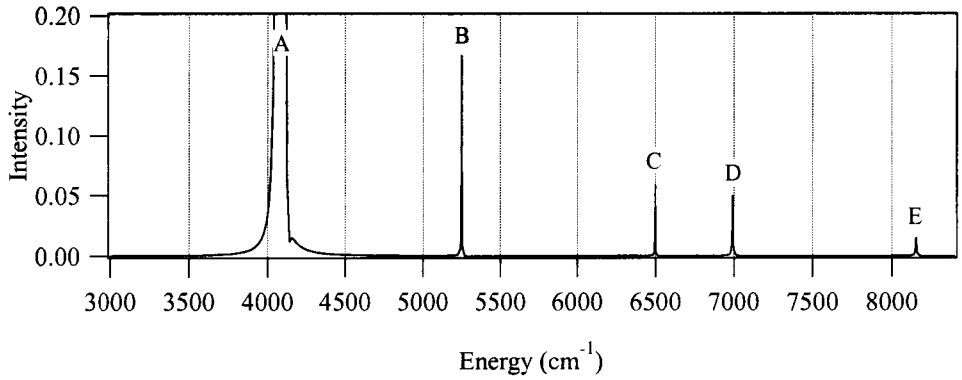

Figure 2.14: Simulated s-polarized K_g^D diffraction spectra from a waveguide with a defect superlattice with a pitch 5x the pitch of the base lattice. Base lattice pitch is 400 nm. Incident light is normal to the surface of the waveguide. Note: The feature labeled 'A' does not diffract above the surface of the waveguide.

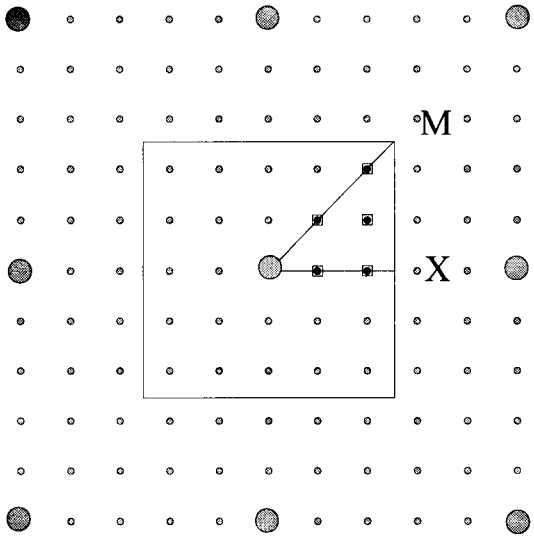

Figure 2.15: Momentum space diagram for a square defect lattice where every fifth lattice site contains a defect. Large dots indicate lattice sites related to the "base" lattice. Dots with small squares indicate defect lattice sites that lie within an irreducible portion of the base lattice reduced zone.

with defect superlattices are used to evaluate this diffraction method in Chapter 5.

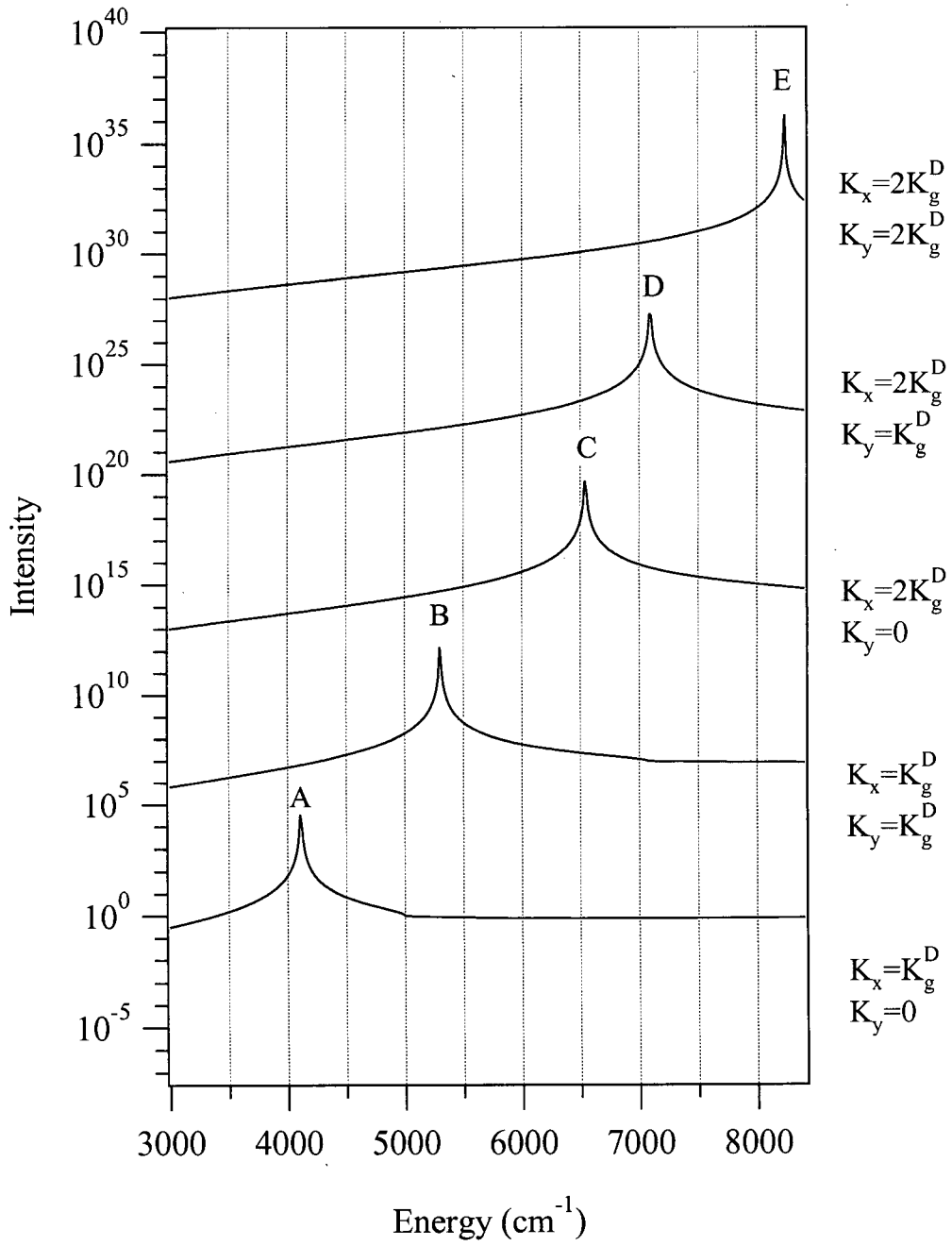

Figure 2.16: Simulated s-polarized spectra for the defect-free lattice described in the text. The notations along the right side indicate the in-plane wavevectors for each spectra. Poles indicate bound modes that exist below the air light line.

Chapter 3

Experimental Design

This chapter describes an apparatus designed and built to implement the linear light scattering techniques described in Chapter 2. The apparatus makes it possible to characterize leaky photonic modes of textured planar waveguides. Its function is to bring white light incident on a textured planar waveguide at a well-defined angle and to collect, condition and focus the light scattered from the waveguide into a spectrometer for analysis. The basic design consists of a fiber optic white light source, three ellipsoidal mirrors, and a concentric rotation stage. Reflective optics were chosen throughout for their ability to avoid the chromatic aberrations inherent in refractive optics. The apparatus was designed specifically to work with a Bomem DA8 Fourier Transform Interferometer (FTIR). The key challenge in the design was to ensure achromatic performance over the range of 6,000 – 13,000 cm^{-1} ($\sim 0.8\,\mu m$ – $1.7\,\mu m$) while localizing the scattering area to $\sim 100\,\mu m \times 100\,\mu m$, the typical size of the textured planar waveguides studied here. For the overall design of the apparatus, ease of use was a primary objective. Samples can be mounted and aligned quickly and characterized easily.

3.1 Apparatus

The principle components of the experimental apparatus are a white light source, focusing optics, positioning mechanics, and a spectrometer. A schematic of the optical layout is shown in Figure 3.1. Unpolarized white light is delivered via a fiber optic cable fixed to a large rotating ring which is concentric with a small rotation stage that holds a textured planar waveguide sample. The white light emitted from the output facet of the fiber is imaged onto the sample by an ellipsoidal mirror (EM1). The light striking the sample is reflected, transmitted, and/or diffracted. One of these emissions is collected by a second ellipsoidal mirror (EM2) and subsequently refocused to an image plane where an adjustable field stop is used in conjunction with a removable CCD camera to eliminate extraneous light. The light then passes through a linear polarizer where the s- or p-polarization is allowed to continue to a third ellipsoidal mirror (EM3). This final ellipsoidal mirror focuses the light into the Bomem FTIR for spectral analysis.

A detailed description of the experimental subsystems follows.

3.1.1 Light Source

A fiber-coupled light source was chosen for this experiment to facilitate easy positioning of the incident light. The textured region of the planar waveguide is typically only $90\,\mu\text{m} \times 90\,\mu\text{m}$, therefore the diameter of the light on the sample was chosen to be $200\,\mu\text{m}$ to overfill the pattern slightly. To achieve the $200\,\mu\text{m}$ diameter spot, the output facet of a $100\,\mu\text{m}$ diameter core optical fiber (optimized for NIR transmission) is imaged by

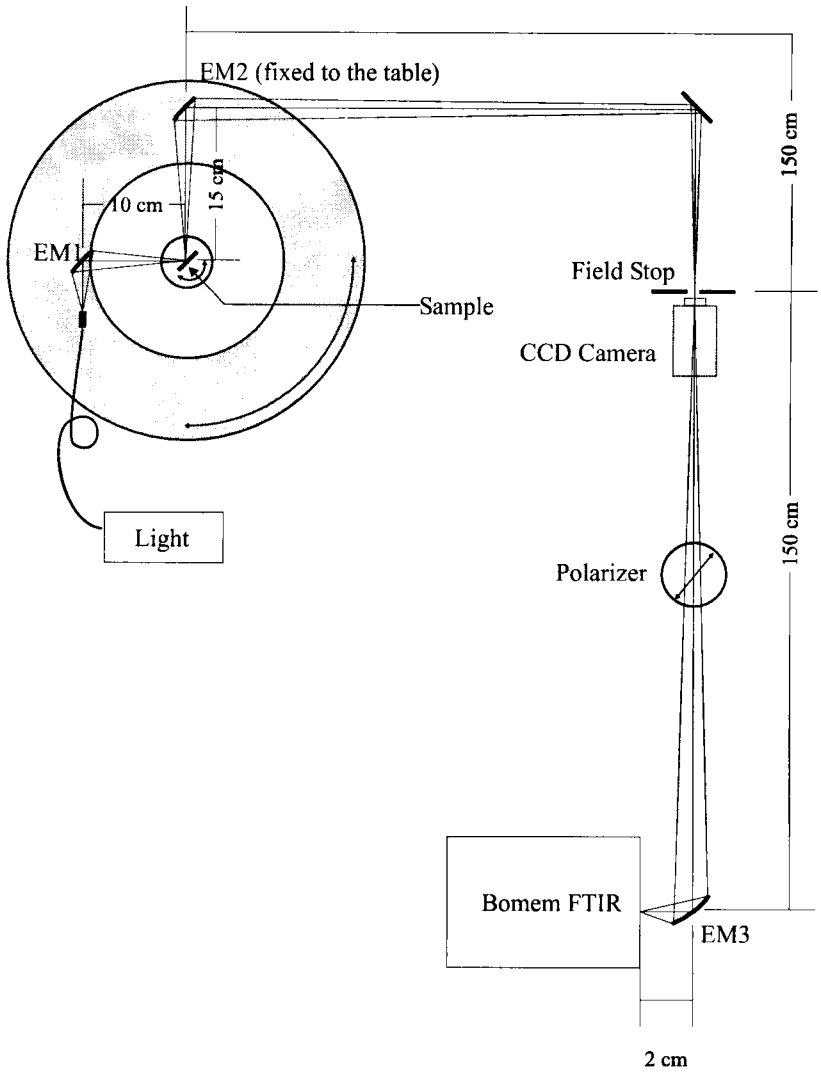

Figure 3.1: Schematic of the experimental apparatus used for optical characterization of textured planar waveguides.

EM1, which was designed to provide a 2x magnification. A 100 watt tungsten quartz halogen bulb housed in a radiometric fiber optic source (Oriel 77501) was chosen for the light source. The electronics in this light stabilize the output to be that of a 3200° Kelvin blackbody. The broadband light emitted from the output facet of the 100 μm diameter fiber was measured to be approximately 1 mWatt between 400 nm and 1.1 μm.

3.1.2 Optics

The function of the optics in this apparatus is to efficiently focus white light onto a sample, collect light emitted from the sample, condition the light and focus it into the FTIR. The design of the optics was constrained by several factors: the parameters of the existing FTIR and the optical fiber chosen to deliver the light, the necessity to create an enlarged image for use with a field stop, and the decision to use white light. Specifically, the light entering the FTIR had to have a full angle divergence of $\sim 14°$ (F/4) to properly fill its internal optics. Secondly, the optics had to accommodate the 100 μm diameter core optical fiber. Thirdly, the optics had to create a 10x image, which is of adequate size for use with the field stop. Finally, the choice to use white light necessitated the use of reflective optics throughout the apparatus in order to avoid the chromatic aberrations inherent in refractive optics. The function of the optics could be achieved and the constraints could be accommodated by using either ellipsoidal mirrors or paraboloidal mirrors.

Ellipsoidal mirrors were chosen over paraboloidal mirrors for their ability to provide point-to-point focusing using a single mirror. A single ellipsoidal mirror focuses light coming from one focus to the other focus, whereas a paraboloidal mirror collects light from its focus and collimates it. A second paraboloidal mirror must be used to take the collimated light and focus it to form an image. Since some light is lost upon reflection, a design with fewer mirrors is preferable when maximum optical throughput is required.

Off-the-shelf ellipsoidal mirrors are not generally available, so mirrors were custom designed and fabricated for this experiment. The following describes how these mirrors were designed.

The following discussion of the mirror design refers to the ellipse pictured in Figure 3.2. The three ellipsoidal mirrors were designed to function interdependently (i.e. a change in a parameter of one mirror necessitated dependent changes in the others). The mirrors were designed as ellipsoidal mirrors where the central cross-section is a simple ellipse. To define the ellipse, the initial consideration was the desired magnification produced by the mirror. Mathematically, the magnification of a simple lens or mirror is determined by the equation $M_t = S_i/S_o$ [9] where M_t is the transverse magnification, and S_i and S_o are the image and object distances respectively. For these mirrors the magnification is given by $M_t = r_2/r_1$. A specific value of either r_1 or r_2 was selected based on the desired physical dimensions of the apparatus. Adding r_1 and r_2 gives the major axis of the ellipse ($2b = r_1 + r_2$). Next the eccentricity of the ellipse must be determined. To do this, the angle between r_1 and r_2 must be selected; to facilitate alignment, 90° was selected for all three mirrors. Finally, in order to specify the physical size of the mirrors, the angles θ_1 and θ_2 must be selected. For this experiment a small cone angle of light illuminating the sample was desired in order to approximate collimated light. See Table 3.1 for the specifications of each mirror. Note the bold values indicate the initial design constraints from which all other values were calculated.

In addition to the specifications delineated in Table 3.1, there was an additional design

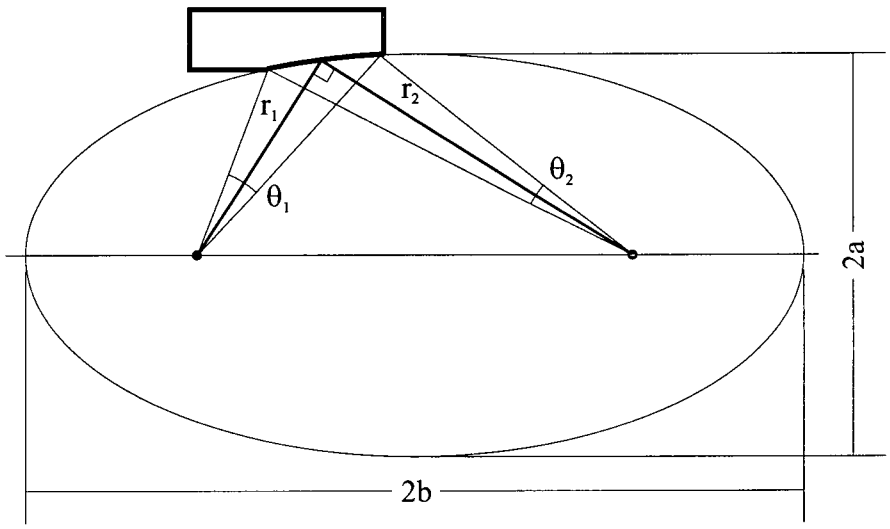

Figure 3.2: Schematic diagram of ellipsoidal mirror design. Light emitting from a point source at one focus will be imaged at the other focus.

requirement for mirror EM1. A portion of the mirror blank was removed to allow mirror EM2 to be placed in close proximity to mirror EM1, in order to enable viewing of the specular reflection as close to normal incidence as possible (see Figure 3.3). Mirrors EM1, EM2, and EM3 were fabricated out of aluminum by Lumonics Corporation.

The following section discusses the components for positioning the mirrors and sample.

Table 3.1: Ellipsoidal mirror specifications. Note: Bold values indicate design constraints.

	EM1	EM2	EM3
r_1 (cm)	5	15	150
r_2 (cm)	10	150	2
M_t	**2**	**10**	0.013
θ_1	3.8°	**2.0°**	0.19°
θ_2	**2.0°**	0.19°	14.39° (**F/4**)

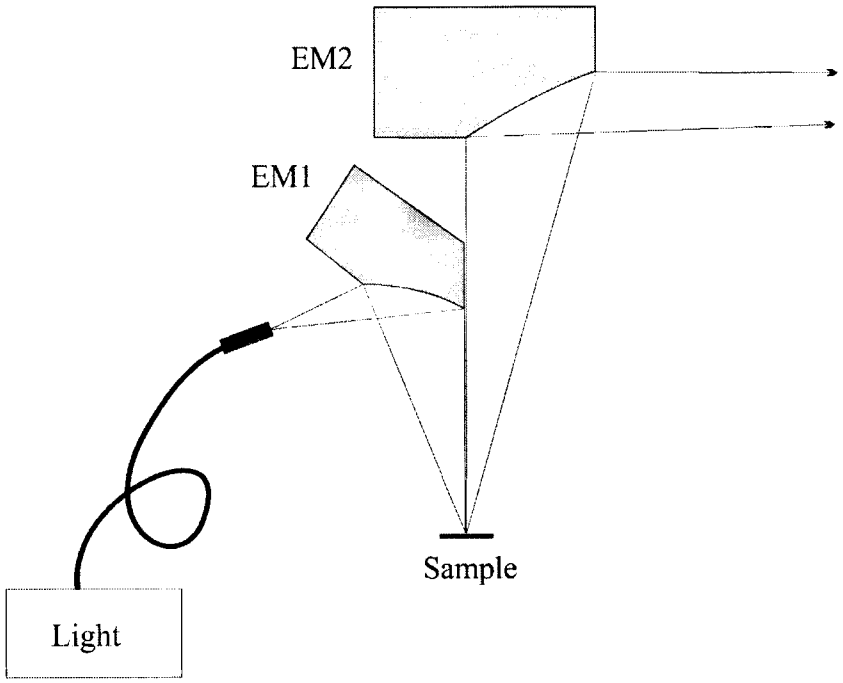

Figure 3.3: Detail of EM1 and EM2 mirrors, showing shape of EM1 which allows viewing of specular reflection near normal incidence.

3.1.3 Positioning Mechanics

The primary function of the positioning mechanics is to enable consistent and precise placement of the sample and light source relative to each other and to the collection optics. For this experiment, the FTIR and associated collection optics remain stationary while the sample and source light rotate. A concentric, $\theta - 2\theta$ design is used to accomplish this. This concentric system consists of an inner rotation stage which holds the sample, and an outer rotating ring which holds EM1 as well as the end of the optical fiber. The system is aligned so that the light is focused precisely at the shared center of rotation. Positioning a textured planar waveguide sample precisely on the center of rotation of the two rotation stages enables the sample to be rotated to different viewing angles

without requiring the viewing optics (EM2 and EM3) to be realigned. To achieve the precise positioning of the sample, a five stage sample mount was designed (see Figure 3.4). The bottom translation stage allows the center of rotation of the sample mount to be positioned concentric with the outer rotating ring. The horizontal rotation stage is used in conjunction with the outer rotation ring to control the angle of incident light, θ. The XYZ translation stage is used to position the sample on the center of rotation of the sample stage and to position the height of the sample relative to the optics. The tilt stage is used to ensure the sample is mounted vertically. Finally, the vertical rotation stage is used to adjust the azimuthal angle of the sample (ϕ). This five stage system allows for samples to be mounted rapidly as well as accurately.

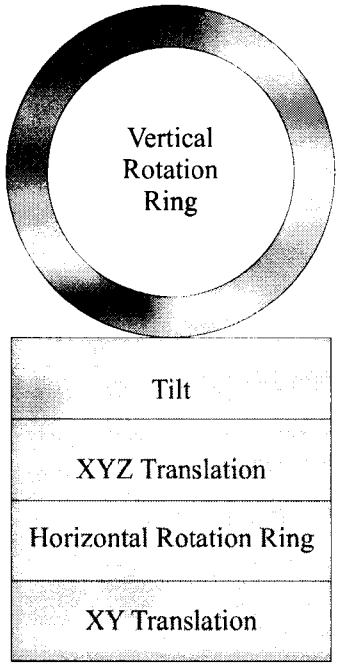

Figure 3.4: Block diagram showing sample mounting and alignment apparatus.

The mount, shown in Figure 3.5, was designed to be used in conjunction with the vertical rotation ring depicted in Figure 3.4. This mount was designed to hold the sample in the center of the vertical rotation ring allowing for the maximum possible angle of incidence for both reflection and transmission measurements without necessitating adjustment to the position of the sample. Based on the physical size of the vertical rotation ring and the 2° divergence of incident light, the maximum angle of incidence for reflection and transmission measurements is ~65°. The mount was designed for ease of use in affixing various samples. The mount has a flat, polished surface onto which the sample is affixed. The sample is held in place with an adhesive medium, such as vacuum grease for the lighter weight GaAs samples, and two-sided tape for the heavier polymer samples. When placing a sample onto the mount, it is not necessary to position it precisely, because, as previously discussed, the translation stages are used to perform all necessary adjustments to bring the sample into proper alignment. Further, the sample can be mounted such that the area of interest is held above the mount, allowing for transmission as well as reflection.

3.1.4 Spectrometer

The light scattered from the textured planar waveguide sample is analyzed with a Bomem FTIR. This spectrometer consists of a Michelson interferometer with a quartz beam splitter and an InGaAs detector. The light is focused into the entrance aperture of the

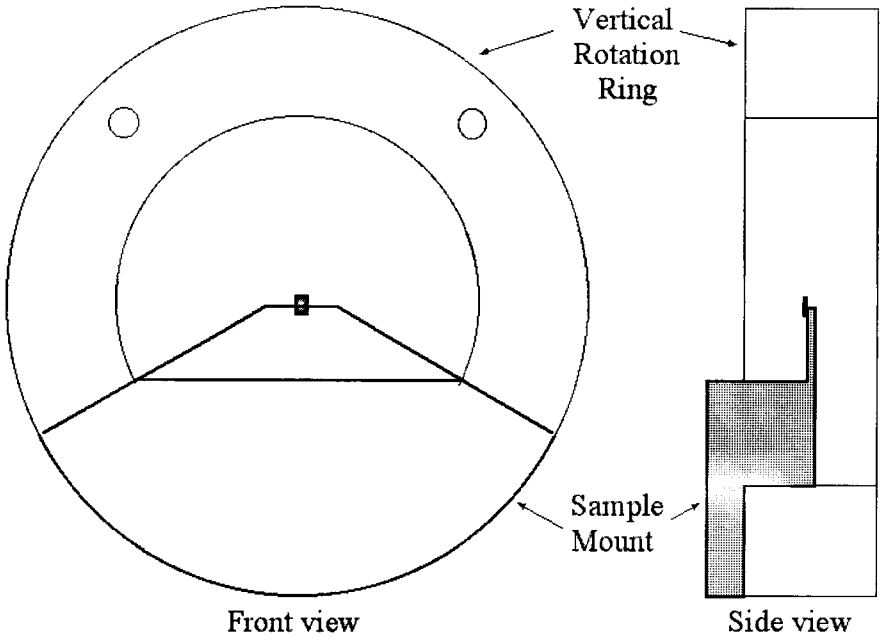

Figure 3.5: Detail of sample mount used in vertical rotation ring.

FTIR by mirror EM3, with the F/4 needed to properly fill the internal optics. The InGaAs detector and quartz beam splitter allow spectral measurements from approximately 6,000 cm^{-1} to 13,000 cm^{-1}.

3.2 Alignment and Operation of Apparatus

The following is the procedure for aligning the apparatus for use, listed in the prescribed order. Place the sample to be characterized on the sample mount. Align the centers of rotation of the inner rotation stage and the outer rotating ring to coincide. Focus EM2 on this shared center of rotation, using the image on the CCD camera as a guide. Adjust EM1 to focus the light onto this center of rotation, using the CCD camera to confirm proper placement. Use the XYZ translation stage to position the sample at the shared

center of rotation and at the proper height. Remove the CCD camera from the optics path. Back-illuminate the detector aperture inside the Bomem FTIR and use to co-align with the light reflected from the sample. Remove back illumination source.

To collect data at a desired angle of incidence, use the vernier scales on the outer rotating ring, the inner rotation stage and the vertical rotation ring to adjust the angle of incident light and the angle of collected light accordingly.

3.3 Alternate Configurations

This experimental apparatus is versatile, allowing for the substitution of light sources as well as collection optics. Mounts were designed to accommodate an Erbium doped fiber amplifier (EDFA) as an alternate light source. Also, an additional sample mount was designed to be used in place of the vertical rotation ring to allow the viewing of light emitted from the cleaved edge of a sample which would otherwise be blocked by the vertical rotation ring. This mount is shown in Figure 3.6.

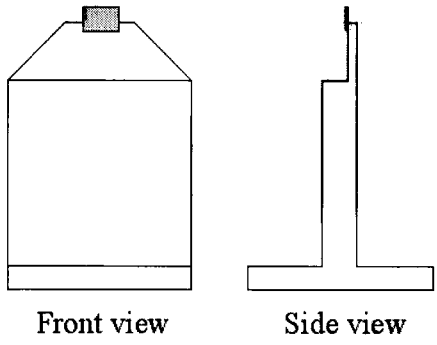

Figure 3.6: Sample mount specifically designed to enable the viewing of light coupling out of the cleaved edge of a waveguide.

Chapter 4

Sample Preparation

The experimental apparatus described in Chapter 3 is used to characterize textured planar waveguides. Two types of textured planar waveguides are investigated in this thesis: GaAs on oxide, and polymer on glass. This chapter discusses the fabrication of these textured planar waveguides.

4.1 GaAs Sample

There are four phases in the fabrication of a GaAs-based textured planar waveguide such as the one depicted in Figure 4.1: growth of the planar waveguide, electron beam lithography, etching, and oxidation. A description of each of these phases follows.

4.1.1 Planar Waveguide Growth

The first step in fabricating a GaAs-based textured planar waveguide is to make a planar waveguide. This is done by using molecular beam epitaxy (MBE) to grow $Al_{0.98}Ga_{0.02}As$

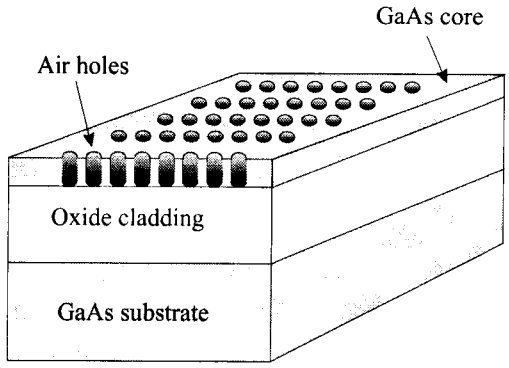

Figure 4.1: GaAs-based textured planar waveguide schematic.

on a GaAs substrate. The waveguide core is then grown on top of the $Al_{0.98}Ga_{0.02}As$ layer.

Dr. Shane R. Johnson from Arizona State University grew two separate planar waveguides, ASU721 and ASU506, which were used for the experiments reported here. ASU721 was grown on a 500 μm GaAs substrate; the $Al_{0.98}Ga_{0.02}As$ layer is $\sim$1.6 μm thick and the core is 80 nm thick, consisting of two layers: a 40 nm GaAs cap on top of 40 nm of $Al_{0.3}Ga_{0.7}As$. ASU506 was grown on a 100 μm GaAs substrate; the $Al_{0.98}Ga_{0.02}As$ layer is 1.0 μm thick and the single layer core of GaAs is 155 nm thick.

Once complete, the planar waveguide wafer is cleaved into smaller samples for further processing. The typical sample size used for these experiments was 5 mm x 5 mm.

4.1.2 Electron Beam Lithography

To prepare the waveguide samples for lithography, they are cleaned and an electron beam resist is applied to the top surface of each. For this experiment, ASU721 and ASU506 were cleaned with acetone and methanol. The resist applied was approximately 3 drops of

4% Polymethylmethacrylate (PMMA) 950K dissolved in a chlorobenzene solution. The samples were spun at 8,000 rpm for 40 seconds, yielding a thickness of approximately 200 nm. Finally the samples are baked on a hot plate at 175°C for a minimum of 2 hours. This process bakes off the solvents in the PMMA, and the samples are ready for lithography.

Electron beam lithography is a process by which an electron beam transfers a prescribed pattern onto a resist. A Hitachi 4100 computer-controlled thermal-emission scanning electron microscope (SEM) was used to perform the lithography on the GaAs samples. Lithography software (NPGS) [19] directs the SEM to make a pattern in the PMMA by exposing the resist at pre-determined coordinates with a specified dose. The electron beam breaks the long polymer chains of the PMMA. The broken chains are then removed from the sample by developing, which involves immersing the sample in chemicals that selectively eliminate the shorter polymer chains without affecting the longer chains. The longer the electron beam dwells in a particular location during lithography, the more chains are broken, resulting in a larger hole once developed. The developing recipe for this experiment is shown in Table 4.1. The PMMA resist has now been transformed into an etching mask.

4.1.3 Etching

To transfer the pattern from the mask to the sample, an etching process is used. The etching for this experiment is based on a dry plasma technique and is done with a

Table 4.1: PMMA developing recipe

Chemical	Time
MIBK	90 sec
Propanol	30 sec
DI Water	30 sec
Oxyethylmethenol	15 sec
Methanol	30 sec

Plasma Quest electron-cyclotron resonance (ECR) etcher. In the etcher, within a strong, static magnetic field, a microwave source drives the electrons in a low pressure gas at their cyclotron resonance, creating a plasma. The radio frequency (RF) bias drives ions from the plasma cloud along the magnetic field lines to strike the sample normal to the surface, where they kinematically and chemically etch the exposed GaAs. The specific etch recipe used is shown in Table 4.2. This recipe, developed based on research presented by Sah [27], etches cylindrical holes (or other desired pattern) with vertical sidewalls in the GaAs at approximately 100 nm per minute. During etching, the masked portions of the GaAs are protected by the PMMA, while the chemicals etch the remainder of the GaAs. The PMMA is also etched by the chemicals, but the etching time is short enough (i.e. less than 150 seconds) that the chemicals do not fully ablate the mask. After the etching process is complete, the sample is rinsed with acetone and methanol to remove the remaining PMMA. The sample is now ready for oxidation.

Table 4.2: ECR recipe

Cl_2	2.0 sccm
BCl_3	2.0 sccm
Ar	20.0 sccm
Microwave	100 Watts
RF Bias	100 Volts
RF Power	25 Watts
Chuck Temp	5°C
Process Pressure	10 mTorr
Backside He	5 Torr
Time	145 sec

4.1.4 Oxidation

The final step in fabricating the GaAs textured planar waveguides used in this thesis is to oxidize the aluminum cladding layer of the waveguide using an oxidation furnace. For a detailed description of the design and construction of the oxidation furnace used here, refer to Reference [32]. To oxidize the aluminum layer, the sample is sealed in the oxidation furnace which is purged with dry nitrogen for 1 hour. Subsequently the temperature is increased from room temperature to 425°C over a period of 30 minutes. The temperature is maintained at 425°C for 40 minutes, during which time 100 sccm of nitrogen is bubbled through 95°C water and routed through the furnace. This warm, moist environment oxidizes the aluminum layer through the etched holes. After the 40 minute oxidation period, the 100 sccm of nitrogen is re-routed directly into the furnace,

bypassing the bubbler, slowly purging the moisture out of the furnace while the temperature is reduced at a rate of 30° per hour until reaching room temperature, which completes the oxidation process.

The purpose of oxidizing the aluminum layer is to change its index of refraction so that it is significantly lower than that of the core layer. Prior to oxidation, the index of refraction of the aluminum layer is n_{Al}=3.6; oxidation reduces this to n_{oxide}=1.6. [33] The resultant GaAs textured planar waveguide has a high index core ($n_{core} \simeq$3.5) with low index cladding (n_{air}=1.0, n_{oxide}=1.6). The fabrication process is now complete, and the sample is ready to be mounted in the experimental apparatus for characterization.

4.2 Polymer Sample

The 2D textured polymer waveguides used in this investigation were fabricated by Paul Rochon's group at the Royal Military College of Canada.

The polymer material is an azoaromatic polymer film, specifically poly[(4-nitrophenyl) [4-[[20(methacryloyloxy)ethyl]ethylomino]phenyl]diazene] (pDR1M). [10, 15, 24] To fabricate this waveguide, a piece of BK7 glass was spin-coated with this polymer to a thickness of ~400 nm.

The process of texturing this polymer waveguide is unique, due to the polymer's unusual response to intense light. This photofabrication process is a direct-write technique which transfers a holographic pattern directly to the polymer. A 514 nm argon laser beam is expanded and collimated, and used to form a linear interference pattern in the

polymer layer of the waveguide. This particular polymer has a well known trans-cis-trans photoisomerization that causes a change in orientation of the polymer molecules. The polymer moves as macromolecules when "activated" by light at a modest intensity ($\sim$mW/cm^2), well below the glass transition temperature of the polymer. This has a migration effect since the molecules that happen to move into the dark areas stop moving. The polymer becomes thicker in the areas of destructive interference and thinner in the areas of constructive interference. The resultant pattern is a linear variation in the morphology of the polymer which directly corresponds to the interference pattern used. To make a 2D square lattice grating, a linear pattern is made, then the process is repeated with the sample rotated 90°. The exposure pattern for this polymer grating is shown in Figure 4.2.

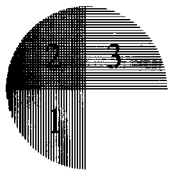

Figure 4.2: Exposure pattern for the polymer sample. Regions (1) and (3) are 1D gratings, while the overlapping region (2) is a 2D square lattice.

This fabrication technique can be used to make gratings in the polymer with a depth of modulation of several hundred nanometers. Gratings written in this way are easily erased by heating the sample to the glass transition temperature, but are thought to be

stable at room temperature. [25]

Chapter 5

Results and Discussion

This chapter presents the results of linear white light spectroscopy experiments on several 2D textured planar waveguides. The experimental data is rigorously compared with simulations based on the Green's function formalism described in Chapter 2. Together, the theoretical and experimental results from some basic structures are used to derive a comprehensive understanding of electromagnetic excitations associated with both low and high index-contrast 2D textured planar waveguides. This forms the foundation for using the same techniques to design and characterize structures with particular properties that may find applications as linear and non-linear optical components.

Section 5.1 presents the dispersion and polarization properties of modes near the second order gap of two simply-textured planar GaAs waveguides as determined from specular reflectivity spectra. Outstanding quantitative agreement between the model and experimental results is demonstrated for both square and triangular lattice structures in thin ($\sim$80 nm) GaAs slabs. The results from these high index-contrast structures reveal substantial renormalization of the electromagnetic modes attached to the porous slab

over a range of frequencies that span approximately 10% of the "center frequency." The dispersion, lifetimes, and composition of these leaky Bloch states are interpreted using a simple picture: the 2D texture couples what are effectively the slab modes characteristic of an untextured structure with the core layer replaced by a uniform layer of refractive index given approximately by the average index of the textured core.

Section 5.2 reports dispersion properties of two quite different structures that were considered because of their potential relevance in practical applications. Section 5.2.1 discusses a low index-contrast 2D textured waveguide formed in a novel polymer material that spontaneously develops a deep ($\sim$200 nm) texture with sub-micron periods upon being exposed to holographic laser fields. These polymer structures were developed in Kingston Ontario, and the results reported here represent the first comprehensive study of their scattering properties over a broad range of frequencies. Section 5.2.2 reports the successful realization of a high index-contrast textured planar waveguide specifically designed to possess an extremely flat band along the entire Γ–X axis of the square Brillouin zone. Such flat bands are expected to offer significant advantages in some non-linear optical applications.

Section 5.3 experimentally and theoretically evaluates the use of defect superlattices as an effective alternative for probing the electromagnetic Bloch states associated with porous slab waveguides. The evaluation process identifies instances where a new diffraction measurement technique offers considerable advantages due to its background-free nature, but also identifies some limitations of the approach, at least when implemented

with a low power white light source. Finally, Section 5.3.3 describes a design for an angle insensitive notch filter based on a high index-contrast structure that incorporates a defect superlattice and exhibits a complete first-order pseudo-gap.

5.1 Waveguides with Simple 2D Gratings

The purpose of this section is to explore the symmetry and polarization properties of leaky modes bound to textured planar waveguides, and to quantitatively validate the computer modeling code. Specifically, the specular reflectivity technique is used to probe the modes near the second order gap of waveguides with square and triangular lattices that were designed and fabricated for this purpose. Both waveguides contain high index-contrast gratings.

5.1.1 Square Lattice

To investigate the characteristics of a planar waveguide with a simple, high index-contrast grating, a square lattice of round holes was etched into a GaAs waveguide, like the one depicted in Figure 4.1. This waveguide does not have a complete photonic pseudo-gap, but was selected for pedagogical purposes because it illustrates key features of the dispersion of photonic modes in this type of waveguide.

The textured planar waveguide sample discussed in this section was fabricated by another student in the group, V. Pacradouni, using ASU721. The sample is comprised of: 40 nm of GaAs on top of 40 nm of $Al_{0.3}Ga_{0.7}As$, clad by air above and 1.8 μm of fully

oxidized $Al_{0.98}Ga_{0.02}As$ below, on a GaAs substrate. A square lattice of circular holes 550 nm apart with a radius of 165 nm was etched completely through the waveguide core, extending into the underlying cladding. The patterned region is 90 μm x 90 μm. The oxide cladding layer is sufficiently thick that the evanescent Fourier components of the Bloch states in the vicinity of the second order gap are limited to the oxide layer. Thus, the finite lifetimes of the modes are determined entirely by a single Fourier component of the polarization which radiates into the upper and lower half spaces.

This sample was characterized by V. Pacradouni using the apparatus designed and built by the author. A detailed investigation of this sample is presented in Reference [21]. When the photonic modes of this sample are probed in the Γ–X direction using the specular measurement technique, the spectra shown in Figure 5.1 are obtained. [20] The dashed spectrum at the bottom of Figure 5.1 was simulated for p-polarized radiation incident at 5°. The second line from the bottom is the corresponding p-polarized data taken from the GaAs waveguide. S-polarized data for various angles of incidence are also shown. The low frequency oscillations are Fabry-Perot fringes, which are due to the interference of light reflecting off the top and bottom surfaces of the oxide layer. The sharp Fano-like resonances indicate coupling into one of the leaky eigenstates of the textured waveguide. These resonances are narrow for modes with long lifetimes and wide for modes with short lifetimes.

To extract the energy and lifetime of the modes from these spectra, a mathematical fitting technique was used. This technique fits an Airy function to the Fabry-Perot

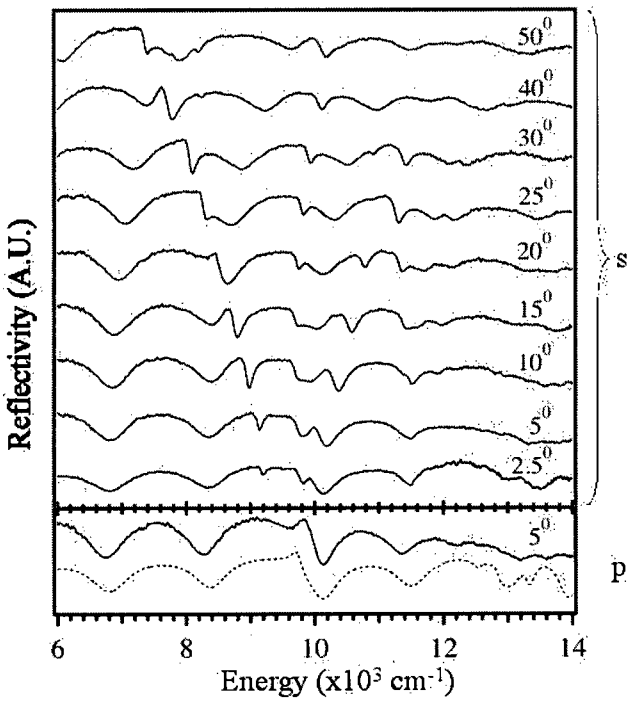

Figure 5.1: Specular reflectivity data for a textured planar waveguide with a simple square lattice of holes etched through the core of ASU721. Angle of incidence is labled on each spectrum. The bottom two spectra are a comparison of simulation (dotted line) and data (solid line) for p-polarized reflectivity. The upper nine spectra are s-polarized specular reflectivity data. [20]

oscillations and a Fano-function to each mode. For a detailed description of this fitting technique refer to Reference [21]. The energy of the modes and the angles of incidence are used to convert these spectra into a dispersion diagram.

Figure 5.2 shows the dispersion diagram for this GaAs waveguide sample. This diagram depicts the s- and p-polarized bands for both the model and the experimental data.

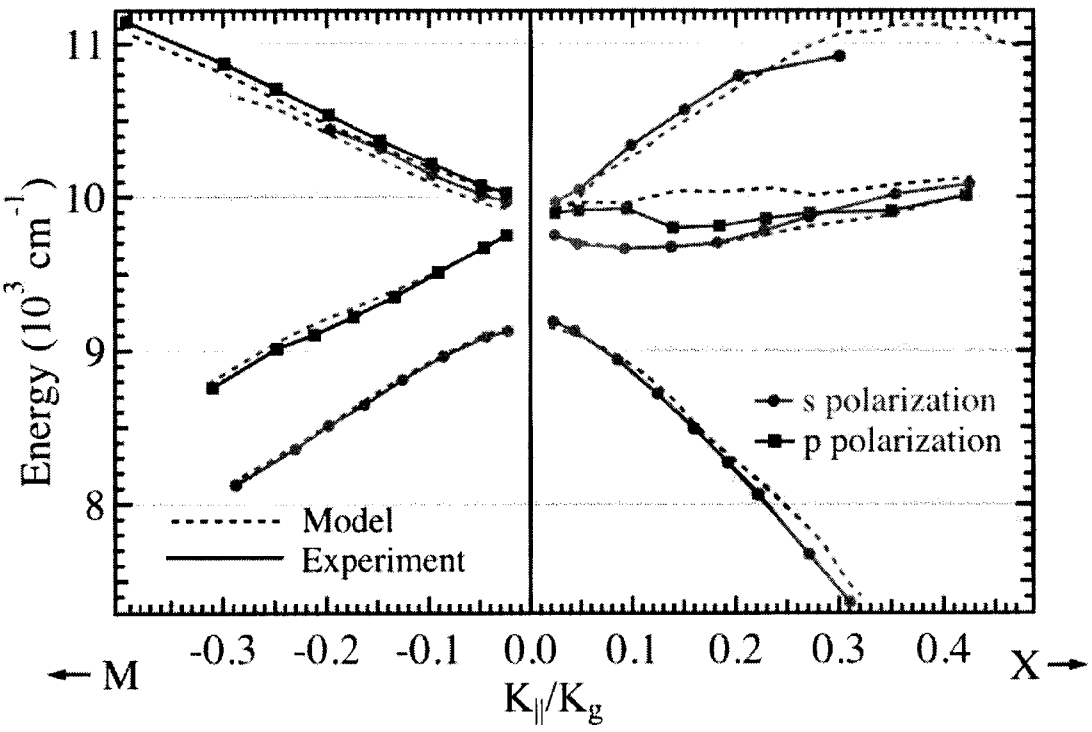

Figure 5.2: Dispersion diagram of the data and simulations for the 2D textured planar waveguide with the square lattice described in the text. [20]

The key computer modeling parameters used are shown in Table 5.1. There are two low-dispersion bands in the Γ–X direction near 10,000 cm^{-1}. These bands have a very low group velocity and are therefore good candidates as hosts for certain non-linear optical conversion processes. [28–30] As a consequence of the symmetry of a square lattice (as discussed in Chapter 2), one p- and three s-polarized bands are evident near the second order gap in the Γ–X direction, while there is one s-polarized band and one p-polarized band dispersing up, and one s-polarized band and one p-polarized band dispersing down in the Γ–M direction. This grating produces a large second order gap at zone center, ~10% of the center frequency. Reference [20] elaborates on the dispersion of the mode

lifetimes, which are also in remarkable agreement with the simulations and predictions based on symmetry arguments. The quantitative agreement between the data and the computer model for the dispersion, as well as for the lifetimes of the modes, to this author's knowledge is the best reported for 2D textured planar waveguide structures.

Table 5.1: Key modeling parameters for textured planar waveguide with square lattice

Parameter	Value
Pitch	550 nm
Hole radius	161 nm
Thickness of core	83 nm
Core composition	60% $Al_{0.3}Ga_{0.7}As$
	40% GaAs
Oxide thickness	1900 nm
Hole depth	433 nm

While others have been successful in demonstrating a complete gap in a pure 2D photonic crystal of "infinite" rods arranged in a square lattice [12], attempts have proven unsuccessful at creating a complete pseudo-gap in a planar waveguide with a square lattice of holes such as the one described above. A more symmetric lattice configuration makes it easier to achieve a complete pseudo-gap in a planar waveguide.

5.1.2 Triangular Lattice

To explore the band structure of a planar waveguide with a more symmetric lattice, a high index-contrast triangular grating was designed and fabricated. This waveguide was specifically designed in order to characterize the polarization and dispersion properties of

the bands near the second order gap using the specular reflectivity technique. This section demonstrates the characteristics specific to a triangular lattice, and shows the band structure to be richer than that of the previously discussed square lattice. Although this particular waveguide was not engineered to have a complete second order pseudo-gap, a triangular lattice does have a sufficiently high degree of symmetry to produce a complete pseudo-gap, as will be discussed in Section 5.3.3. Unlike the square lattice structure discussed above, the $Al_{0.98}Ga_{0.02}As$ layer beneath the core slab layer in this triangular lattice structure was only partially oxidized, to a depth of ~200 nm. Nevertheless, the simulations again agree remarkably well with the experimentally determined dispersion, as discussed in the present section, and with the lifetimes, as discussed below in Section 5.3.2.

To fabricate this textured planar waveguide, a 90 μm x 90 μm triangular lattice of circular holes 600 nm apart with a radius of 80 nm was etched completely through the core of an ASU721 waveguide, omitting every seventh hole.[1] The $Al_{0.98}Ga_{0.02}As$ layer was partially oxidized, producing a thin oxide layer, on the order of 200 nm thick, on top of the remaining ~1600 nm of un-oxidized $Al_{0.98}Ga_{0.02}As$.

Probing the photonic modes of this waveguide with the specular measurement technique produces the spectra shown in Figure 5.3 for the M direction, and the spectra in Figure 5.4 for the K direction. The Fano-like resonances are evident, as well as Fabry-Perot oscillations. Closer examination of the spectra for a 10° angle of incidence in the M direction (shown in Figure 5.5) reveals a beat in the Fabry-Perot oscillations, which

[1]The reason for the omission of every seventh hole will be explained in Section 5.3

is a result of the two 1D optical cavities (Al-oxide and $Al_{0.98}Ga_{0.02}As$) created by the partial oxidation. There are four s- and two p-polarized resonances in the spectra, which are labeled on this diagram.

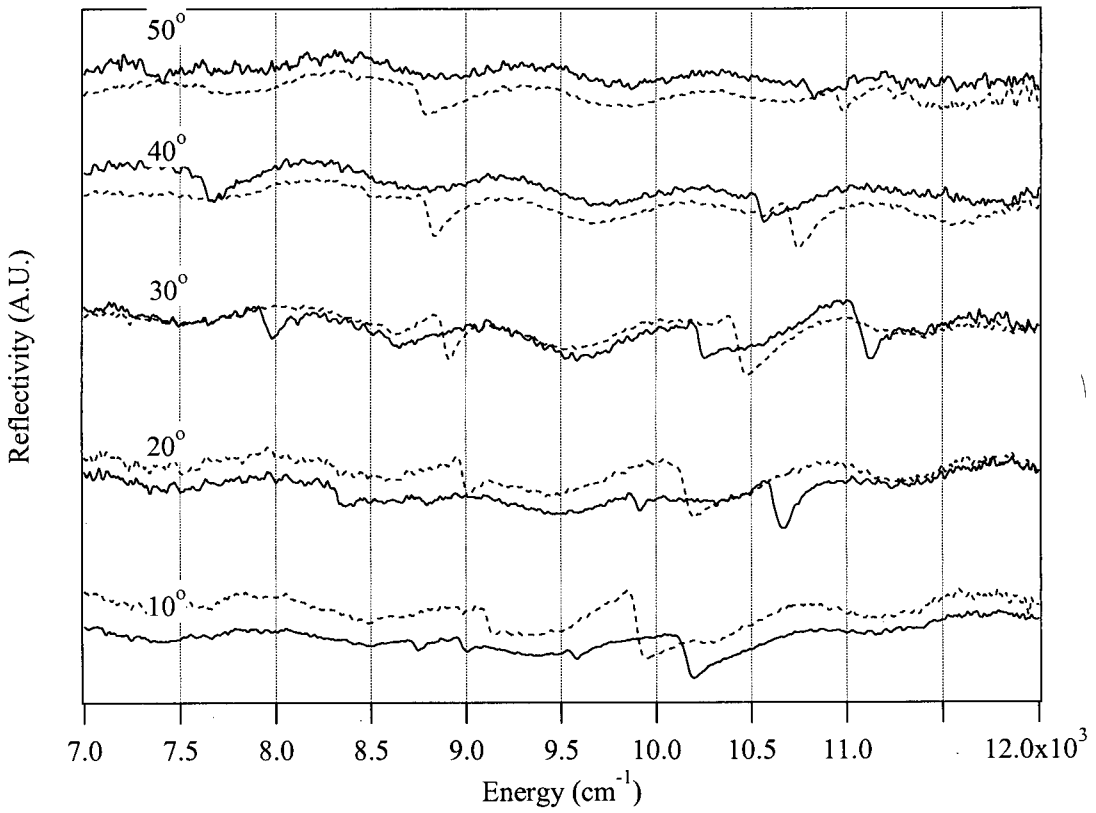

Figure 5.3: Specular reflectivity data for the Γ–M direction from the GaAs textured planar waveguide with a triangular lattice discussed in the text. Solid lines represent s-polarization; dashed lines represent p-polarization.

The mode energies were extracted from the spectra to produce the data points in the dispersion diagram shown in Figure 5.6. In the M direction near zone center, there are four s-polarized bands: two dispersing up in energy, and two dispersing down. There are also two p-polarized bands: one dispersing up, and one down. In the K direction near

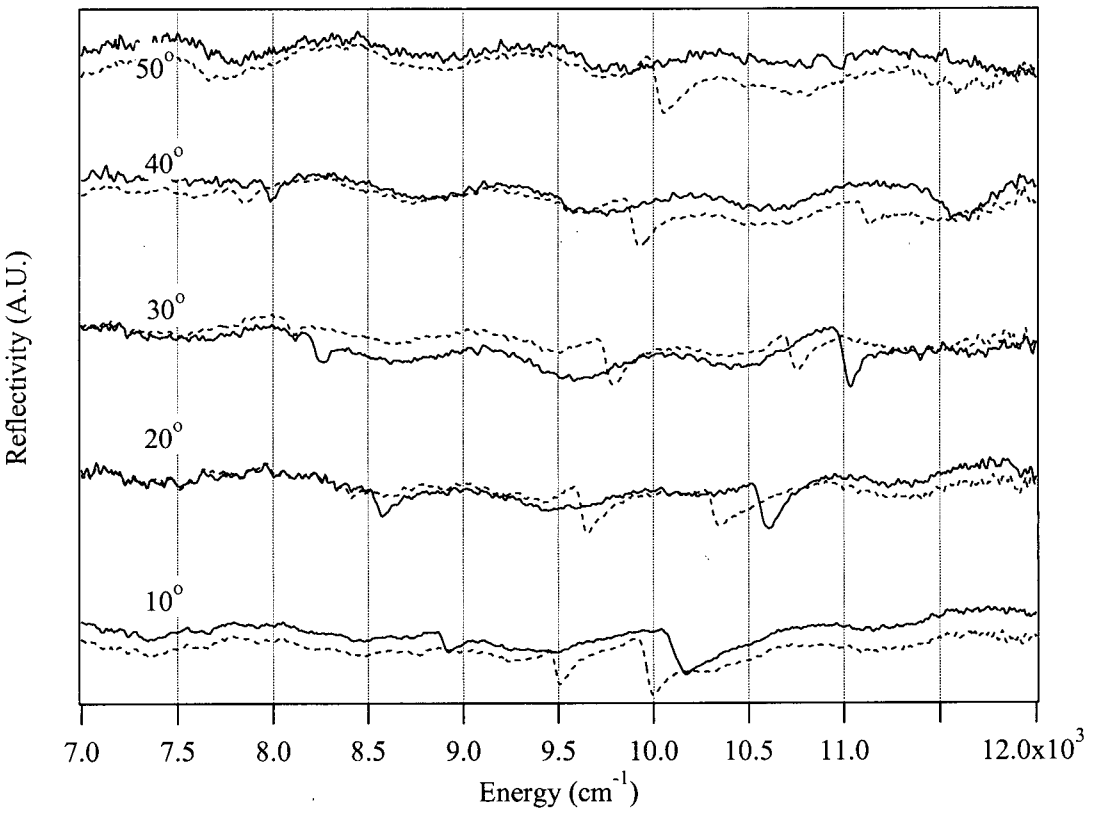

Figure 5.4: Specular reflectivity data for the Γ–K direction from the GaAs textured planar waveguide with a triangular lattice discussed in the text. Solid lines represent s-polarization; dashed lines represent p-polarization.

zone center there are also six bands, however three are s- and three are p-polarized. Two s- and p-polarized pairs disperse up in energy, one pair more strongly than the other. A third pair disperses down in energy. For both the M and K directions, the bands away from zone center and away from the anticrossings are good illustrations of the kinematic dispersion properties discussed in Section 2.1.

To further investigate the characteristics of these modes, the computer model was used to simulate incident radiation at a 10° angle of incidence in the M direction. The

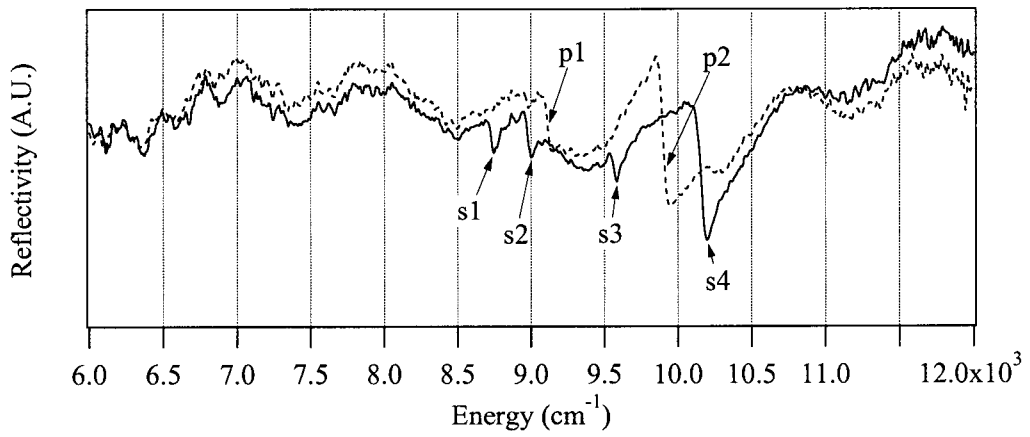

Figure 5.5: Specular reflectivity data for a 10° angle of incidence in the M direction. Solid lines represent s-polarization; dashed lines represent p-polarization. Notice the two Fabry-Perot frequencies which are due to incomplete oxidation of the $Al_{0.98}Ga_{0.02}As$ layer. The higher frequency is approximately 1,000 cm^{-1} which corresponds to ~1,300 nm of unoxidized $Al_{0.98}Ga_{0.02}As$. Six modes are annotated.

six resonant modes clearly seen in the data for this angle of incidence are labeled in Figure 5.5. The four s-polarized modes are labeled s1–s4, while the two p-polarized modes are labeled p1 and p2. The strength of the Fourier components of the field (see Equation 2.2) vary from one mode to the next. Figure 5.7 depicts the relative strengths of each of these Fourier components for each of the six modes. Figures (a) and (d) both show the same two dominant components. These components are "away" from the direction of the incident wavevector and therefore produce downward propagating modes. These components add symmetrically creating an s-polarized mode, and anti-symmetrically creating a p-polarized mode. Figures (b) and (e) show two dominant components each, however in this case the dominant components are "toward" the direction of propagation. These two situations give rise to the upward dispersing s- and p-polarized modes. In the

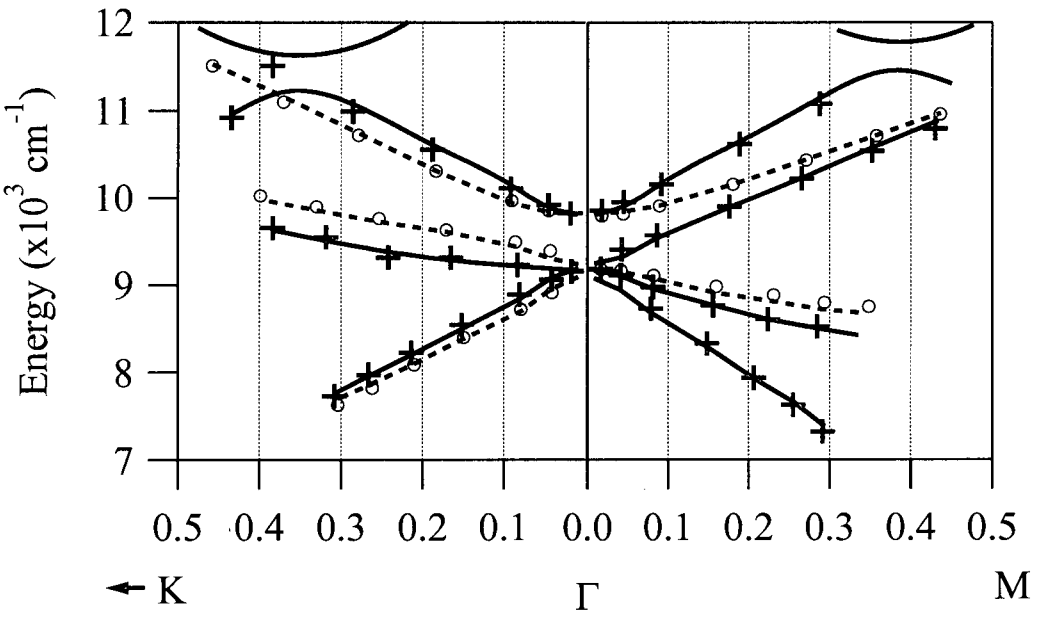

Figure 5.6: Dispersion diagram for the planar waveguide with the triangular lattice discussed in the text. The crosses represent s-polarized data. The circles represent p-polarized data. The solid lines represent s-polarized simulations. The dashed lines represent p-polarized simulations.

final two figures, (c) and (g), there is a single dominant component which gives rise to one s-polarized mode dispersing quickly downward and another dispersing quickly upward. It is important to note these results are for modes occurring approximately 20% of the way across the Brillouin zone, which is far from zone center where there is strong coupling between several of the field components. This is not explained by simple kinematic arguments.

To illustrate the strong coupling near zone center, momentum space diagrams were constructed for the modes close to zone center ($K_{||} = 0.01K_g$) but still slightly detuned in the M direction. These diagrams are shown in Figure 5.8. These diagrams reveal strong

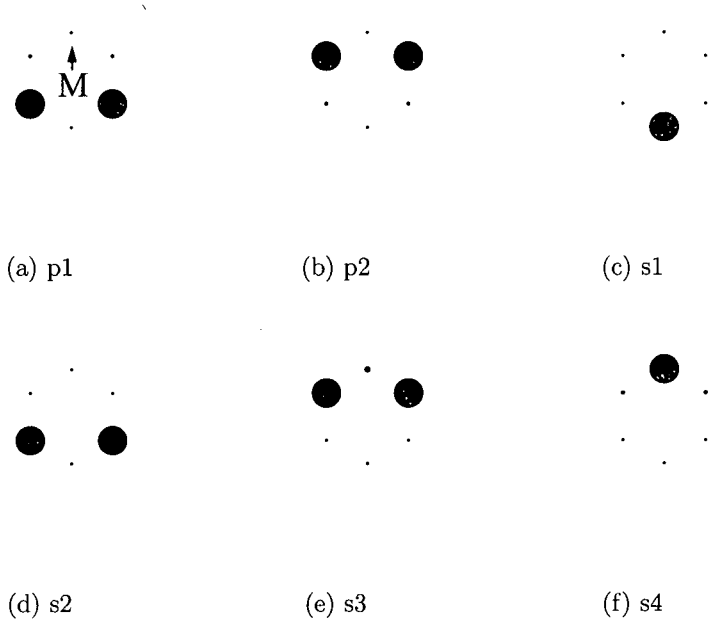

Figure 5.7: Momentum space diagrams for each Bloch mode of the triangular lattice waveguide when probed with light at a 10° angle of incidence. The strength of each Fourier component is indicated by the size of the dot. The labels for each diagram correspond to the labels on the modes shown in Figure 5.5

coupling between multiple field components, which is very non-kinematic. Away from zone center, the highest energy bands display anti-crossings with modes descending from a higher order gap. The size of the gaps is similar to the zone-center gap, suggesting strong band-mixing, which cannot be explained with simple kinematics. Although this waveguide has a defect superlattice, the dispersion properties and polarizations of these bands are fully consistent with that of a waveguide with a simple (non-defect) triangular lattice.

The simulated band structure obtained using the parameters in Table 5.2, is represented as lines on the dispersion diagram in Figure 5.6. As with the square lattice sample,

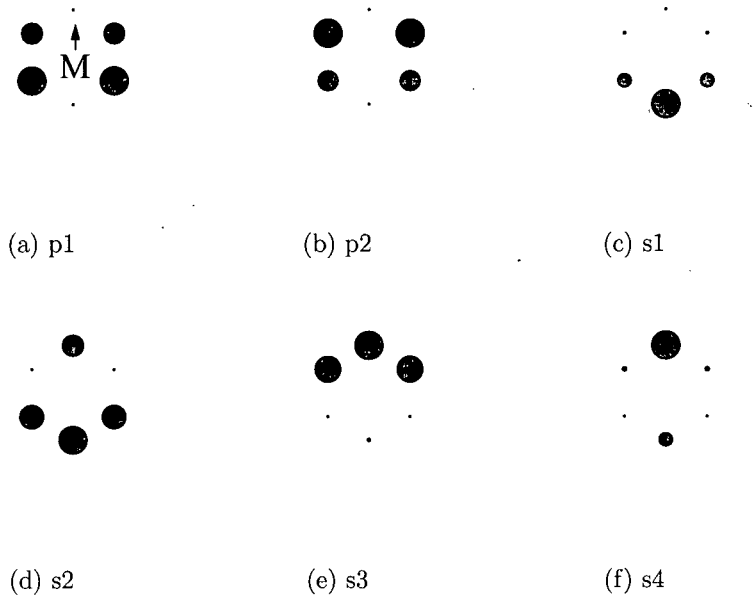

Figure 5.8: Momentum space diagrams for each Bloch mode of the triangular lattice at $K_{||}=0.01K_g$ in the M direction. The M direction is toward the top of the page. The strength of each Fourier component is indicated by the size of the dot. The labels for each diagram correspond to the labels on the modes shown in Figure 5.5

there is remarkable quantitative agreement between the model and the data with regard to dispersion and polarizations. The only parameter of the waveguide which was altered from its nominal value[2] for this simulation was the thickness of the core; it was modeled as a single layer, 73 nm thick, comprised of $Al_{0.15}Ga_{0.85}As$, which was used to simulate the combination of the 40 nm thick layer of $Al_{0.30}Ga_{0.70}As$ and the 40 nm thick layer of GaAs in the sample.

Computer modeling was performed to determine the effect the defect superlattice has on the dispersion characteristics of this structure. Figure 5.9 shows a comparison of

[2]The deviation from the nominal value is within the margin of error.

Table 5.2: Key modeling parameters for textured planar waveguide with triangular lattice

Parameter	Value
Pitch	600 nm
Hole radius	80 nm
Thickness of core	73 nm
Core composition	$Al_{0.15}Ga_{0.85}As$
Oxide thickness	200 nm
Hole depth	73 nm

the spectra for the waveguide at 10° with and without the defect superlattice. There is essentially no difference between the results of the modeling with defects and without them. Thus, in this context, the defect superlattice incorporated in this sample represents only a weak perturbation. The utility of this defect superlattice is explained in Section 5.3.2.

Computer modeling was also performed to study the effect of the thickness of the oxide layer for this structure. Figure 5.10 shows the simulated spectra for this sample with 200 nm of oxide, i.e. a thin oxide cladding. Figure 5.11 shows the simulated spectra for this sample with a thick oxide (1600 nm of fully oxidized $Al_{0.98}Ga_{0.02}As$) cladding. The spectra for the thick oxide sample shows well-defined, narrow Fano resonances, which go to unity reflectivity. [6] The spectra for the thin oxide shows much broader, less well-defined resonances, which do not go to unity reflectivity. The broad nature (i.e. short lifetime) of these modes is due to the fact that the evanescent components of the Bloch states of these modes penetrate the thin oxide and radiate into the substrate through

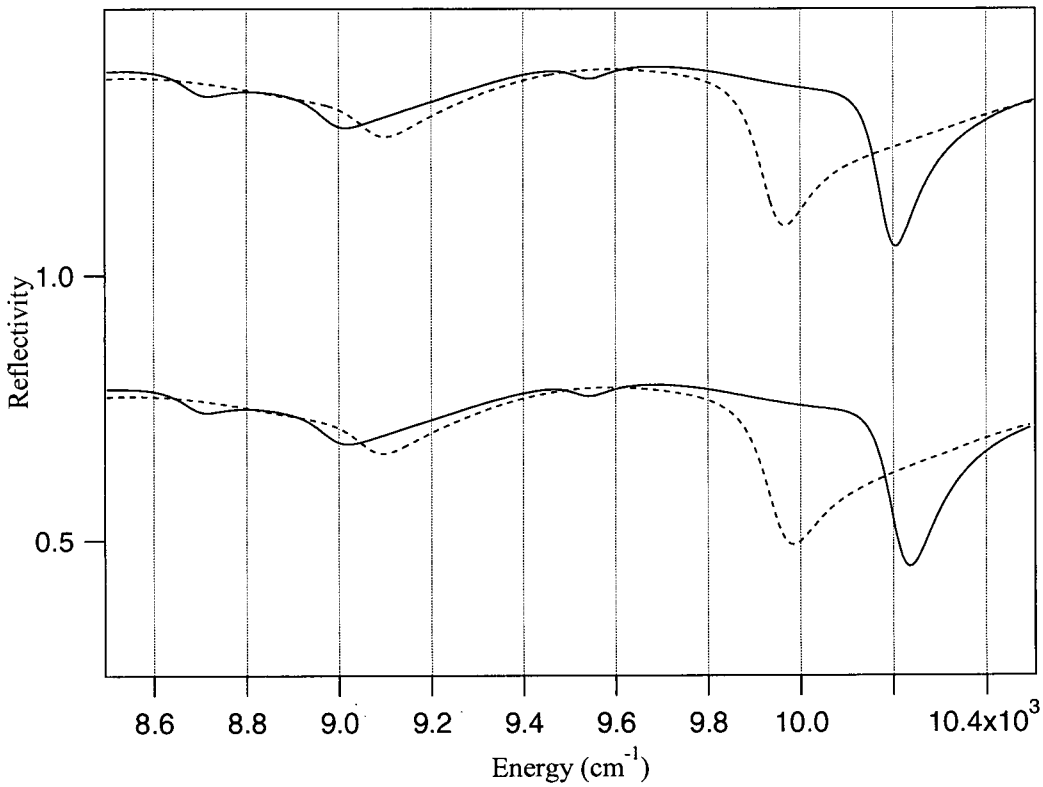

Figure 5.9: Comparison of simulations of the triangular lattice waveguide with and without a defect superlattice at a 10° angle of incidence in the M direction of symmetry. The solid lines represent s-polarized and the dashed lines represent p-polarized reflectivity spectra. The defect superlattice spectra appear below the non-defect spectra.

the oxide. This issue is quantitatively addressed in Section 5.3.2. It is interesting to note that this qualitative change in the nature of the modes has hardly any effect on the dispersion or the energy of the modes, but a dramatic effect on the lifetimes.

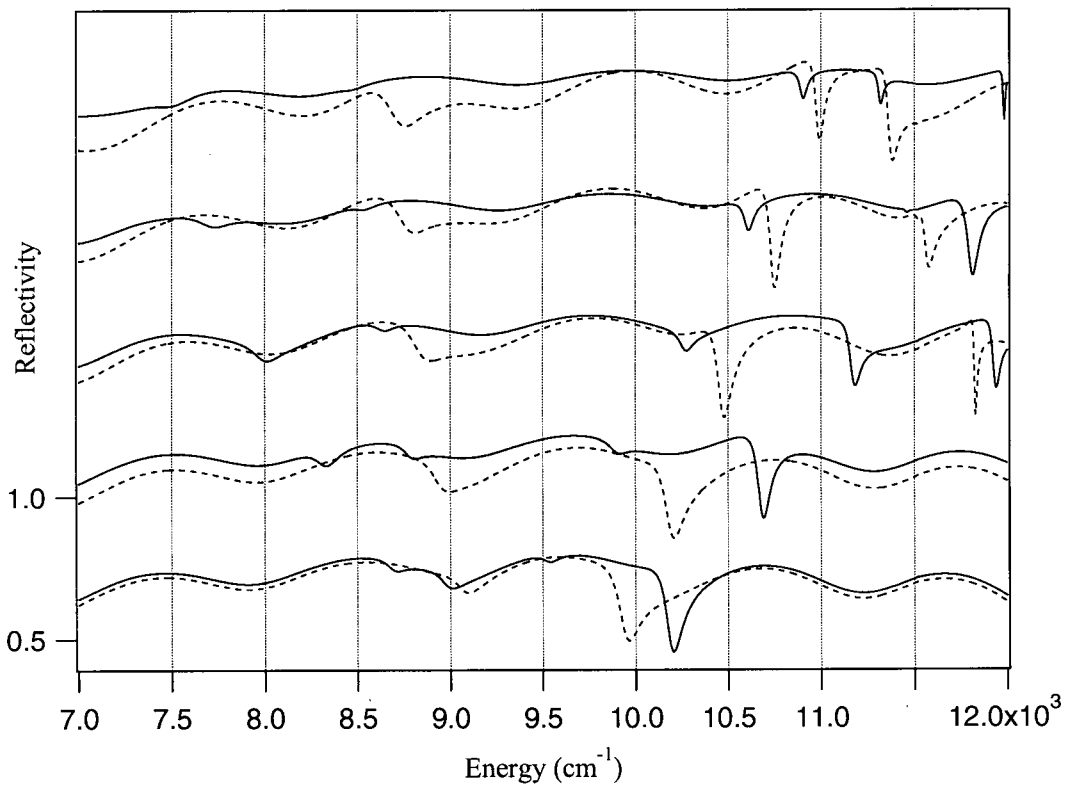

Figure 5.10: Simulated spectra for the M direction of a triangular lattice sample with 200 nm of oxide, i.e. thin oxide layer. The spectra are for angles of incidence of 10°, 20°, 30°, 40°, and 50° from the bottom up. Solid lines represent s-polarization; dashed lines represent p-polarization.

This section has demonstrated the ability to accurately fabricate and characterize textured planar waveguides, and to accurately predict with a rigorous computer model the complex band structure of these waveguides. Outstanding quantitative agreement has been shown between the computer modeling results and the data for both of the simple

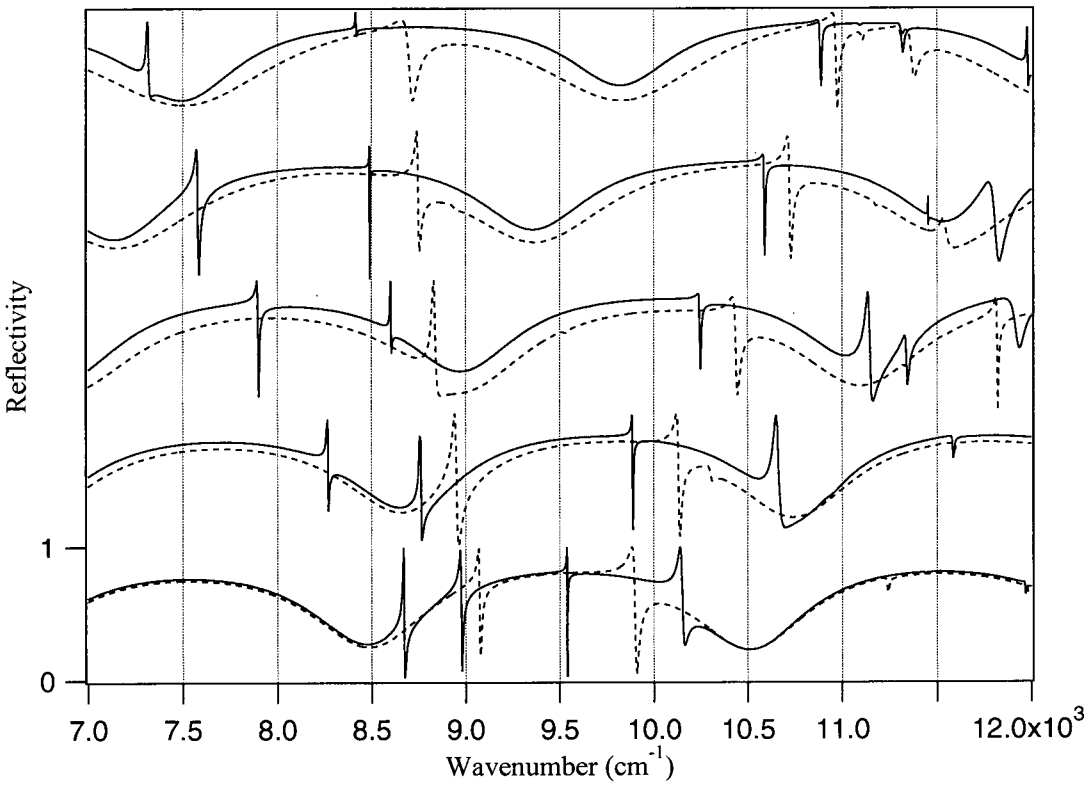

Figure 5.11: Simulated spectra for the M direction of a triangular lattice sample with 1600 nm of oxide, i.e. thick oxide layer. The spectra are for angles of incidence of 10°, 20°, 30°, 40°, and 50° from the bottom up. Solid lines represent s-polarization; dashed lines represent p-polarization.

lattice configurations examined. The configuration and materials of textured waveguides have been shown to strongly influence the propagation of light in these structures. The ability to predict through computer modeling the effects of these factors on the electromagnetic excitations of these waveguides, combined with a thorough understanding of the underlying nature of the modes, provide the basis for engineering desired band structures using the proven fabrication and characterization techniques.

5.2 Waveguides Engineered for Specific Applications

Planar textured waveguides offer a powerful medium for engineering devices which control the propagation characteristics of light, both in the waveguide and in the surrounding half spaces. This section describes two examples of textured planar waveguides which have been engineered for specific applications. The first is a low index-contrast textured waveguide which uses resonant coupling to effect a polarization insensitive notch filter for radiation incident from the upper half space. This is just one of many examples of simple passive optical devices that might be easily fabricated from the intriguing azo-polymers described in Chapter 4. The results in Section 5.2.1 serve as much to characterize the properties of these textured polymers as they do to demonstrate a particular optical functionality. The second example is a high index-contrast waveguide engineered to possess an extremely broad, flat band, which has been predicted to be useful for significantly enhancing the second harmonic optical conversion process for modes propagating inside photonic crystals. [28, 29, 31]

5.2.1 2D Textured Azo-Polymer Waveguides

Polymer pDR1M is a novel material which can be quickly and simply made into large area, low index-contrast, periodically textured waveguides using a direct-write holographic technique, as described in Chapter 4. Because waveguides fabricated with this polymer do not have the stringent purity requirements that their semiconductor counterparts do, fabrication costs are much less for devices manufactured with this material. This section

reports the first in-depth quantitative study of the broadband scattering properties of this type of azo-polymer waveguide. The reflective characteristics peculiar to this type of waveguide make it particularly well-suited for use as an optical filter. Polymers are currently used in numerous optical applications, such as coatings, filters and fibers. As a representative example of a polymer waveguide application, this section presents the simulation of a pDR1M textured planar waveguide as a polarization insensitive notch filter.

Prior to texturization, the pDR1M polymer waveguide consisted of a nominally 400 nm thick film on BK7 glass. The index of refraction of the polymer was measured to be 1.66 in the visible with an Abbe refractometer, and is estimated to be 1.65 in the near-infrared. [26] The index of refraction of the glass is 1.507 at 1 μm. [8] The core was textured with a square lattice of period 659$\pm$2 nm[3] and a nominal average modulation amplitude of 250 nm. The unit cell of this lattice consists of a paraboloidal-like "rise" in the core medium, rather than a cylindrical hole with vertical sidewalls. The result is a grating of significantly different morphology than the previously discussed GaAs textured planar waveguides, as the atomic force micrograph of the surface of the textured polymer shows in Figure 5.12.

Since the grating of the polymer waveguide is structurally different from the lithographically defined gratings discussed throughout this thesis, the parameters of the polymer grating layer are defined differently for the Green's function code. Previously, where the code modeled a layer of GaAs with "holes" of air, for this waveguide the code models

[3]The period of the lattice was measured using HeNe diffraction.

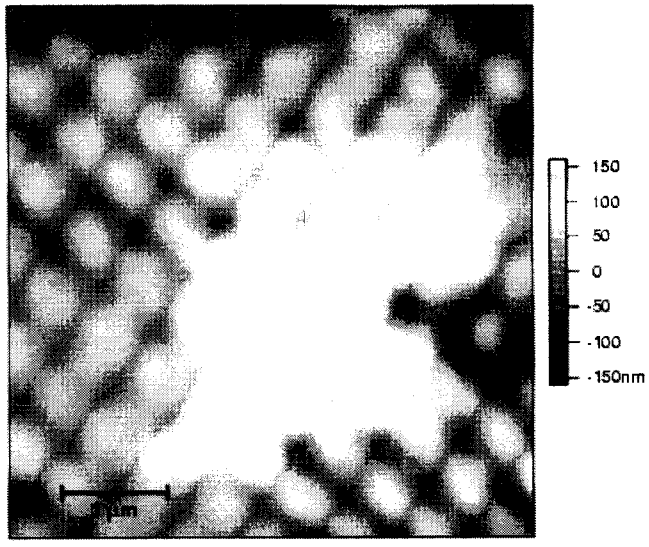

Figure 5.12: Atomic force micrograph of the surface of the textured polymer (pDR1M) waveguide referred to in the text.

a layer of air with "holes" of polymer. Each unit cell of the polymer grating was modeled as a thick vertical cylinder, rather than the actual shape, which was somewhat non-uniform and asymmetric. The paraboloidal shape of the mounds was not entered into the code because modeling them as vertical cylinders with the appropriate filling fraction is sufficient to accurately reproduce the measured dispersion of a waveguide with a low index-contrast grating such as this. The simulated spectra for the polymer waveguide were generated by the computer code using the values shown in Table 5.3.

Table 5.3: Key modeling parameters for textured planar polymer waveguide

Parameter	Nominal	Modeled
Pillar radius	NA	300 nm
Thickness of textured layer	250 nm	250 nm
Thickness of untextured layer	250 nm	400 nm
Period	660 nm	660 nm
n_g	1.507	1.507
n_p	1.65	1.65

The spectra in Figure 5.13 were obtained by probing the photonic modes of the polymer waveguide at a range of incident angles along the Γ–X axis using the specular measurement technique. Notice that superimposed on the relatively low background there are sets of high reflectivity peaks of s- and p-polarized pairs. There appears to be one s- and one p-polarized pair of modes dispersing strongly up in energy, and one pair dispersing strongly down in energy. The remaining s- and p- bands consist of an unresolved group of modes that disperse moderately up in energy. Figure 5.14 shows

the spectra in the M direction, which show two apparent s- and p-polarized band pairs, one dispersing up in energy and the other down. The spectra generated by the computer model reveals that each of these apparent pairs actually consists of two s-polarized modes and two p-, totalling eight modes in the M direction. Furthermore, the modeling for the X direction shows that the middle group of unresolved modes is actually comprised of two s- and two p-polarized modes. This model confirms the remaining modes in the X direction to be one s- and one p-polarized pair of modes dispersing strongly up in energy, and one pair dispersing strongly down in energy.

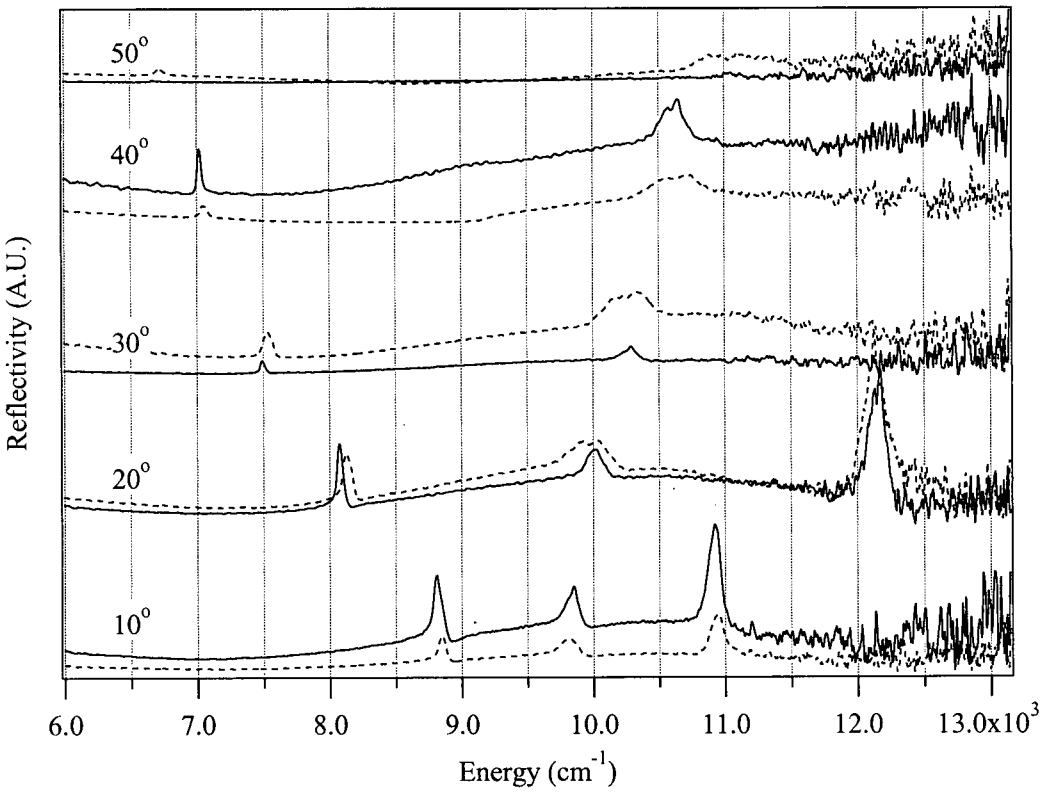

Figure 5.13: Normalized specular reflectivity data for the textured polymer waveguide for the X direction. Solid lines represent s-polarization; dashed lines represent p-polarization.

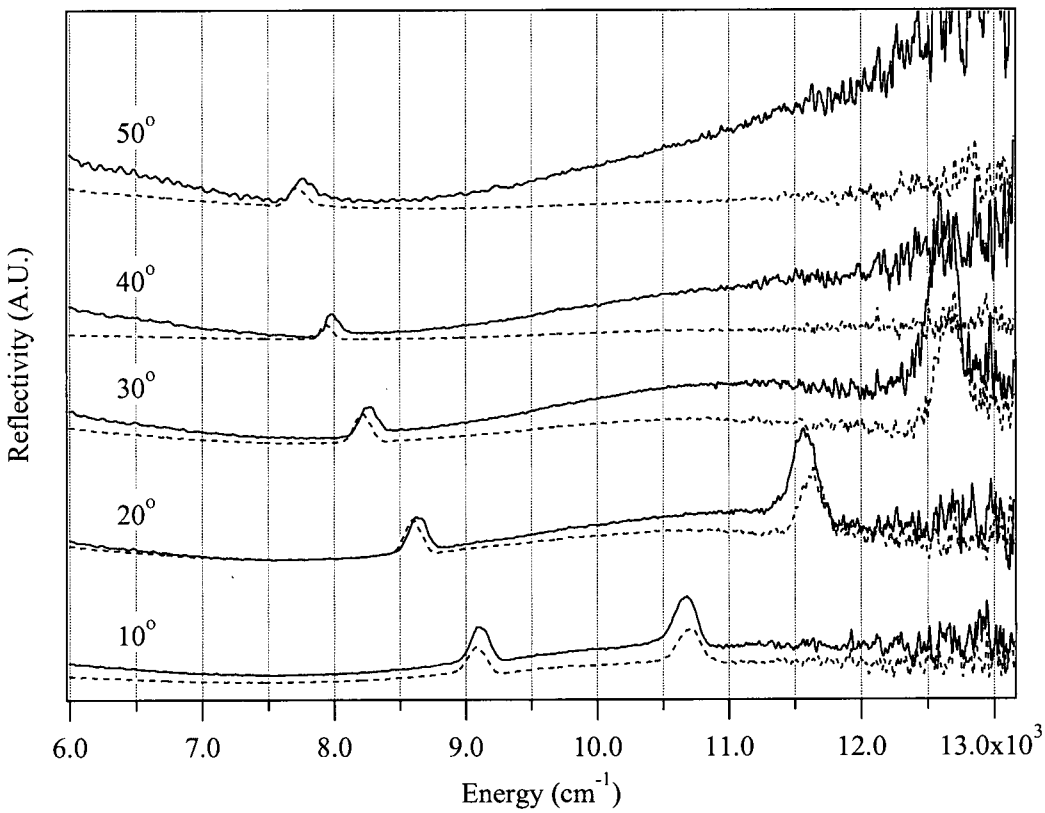

Figure 5.14: Normalized specular reflectivity data for the textured polymer waveguide for the M direction. Solid lines represent s-polarization; dashed lines represent p-polarization.

Figure 5.15 shows the downward dispersing branch of modes in the M direction. In this figure the experimentally derived spectra are superimposed on the corresponding simulated spectra. The model, which assumes a perfectly periodic, infinite grating, shows four distinct modes that rise to unity. However, in the data these modes are broad and overlapping. This broadening of the modes is not due to the resolution limit of the

spectrometer[4], but is a true representation of the mode shape. A published characterization study of a similar polymer waveguide at 632.8 nm reveals a similar discrepancy between the theoretical and the actual mode width, which was partially attributed to absorption. [25] Calculations for the polymer waveguide characterized here indicate that absorption only accounts for approximately 10% of the observed broadening. In the previous publication, it is suggested that birefringence contributes to the broadening, but simulations with birefringence conducted here do not show sufficient broadening. Further, it is suggested in the publication that the broadening may be due to optically induced changes to the polymer caused by their 100 μW probe beam. Since this polymer has the inherent characteristic of changing when exposed to intense light (see Chapter 4), it is reasonable that the probing light could affect changes in the waveguide that would produce noticeable changes in the spectral response.

The reason that the spectra consist of eight bands rather than four (as previously shown for a square lattice) is because the lowest order TE and TM slab modes for this waveguide are nearly degenerate: four bands therefore come from the mixing of the TE-like slab modes, and four bands come from the mixing of the TM-like slab modes. The band structure is shown in Figure 5.16.. This diagram depicts the dispersion for the experimental data as well as for the computer simulation of the polymer waveguide obtained using the parameters listed in Table 5.3.

The computer simulation of the dispersion of the modes agrees well with the experimental data and shows an apparent convergence of the bands near 9,800 cm^{-1}, minimal

[4]The spectral data reported in this thesis was acquired at 7 cm^{-1} resolution.

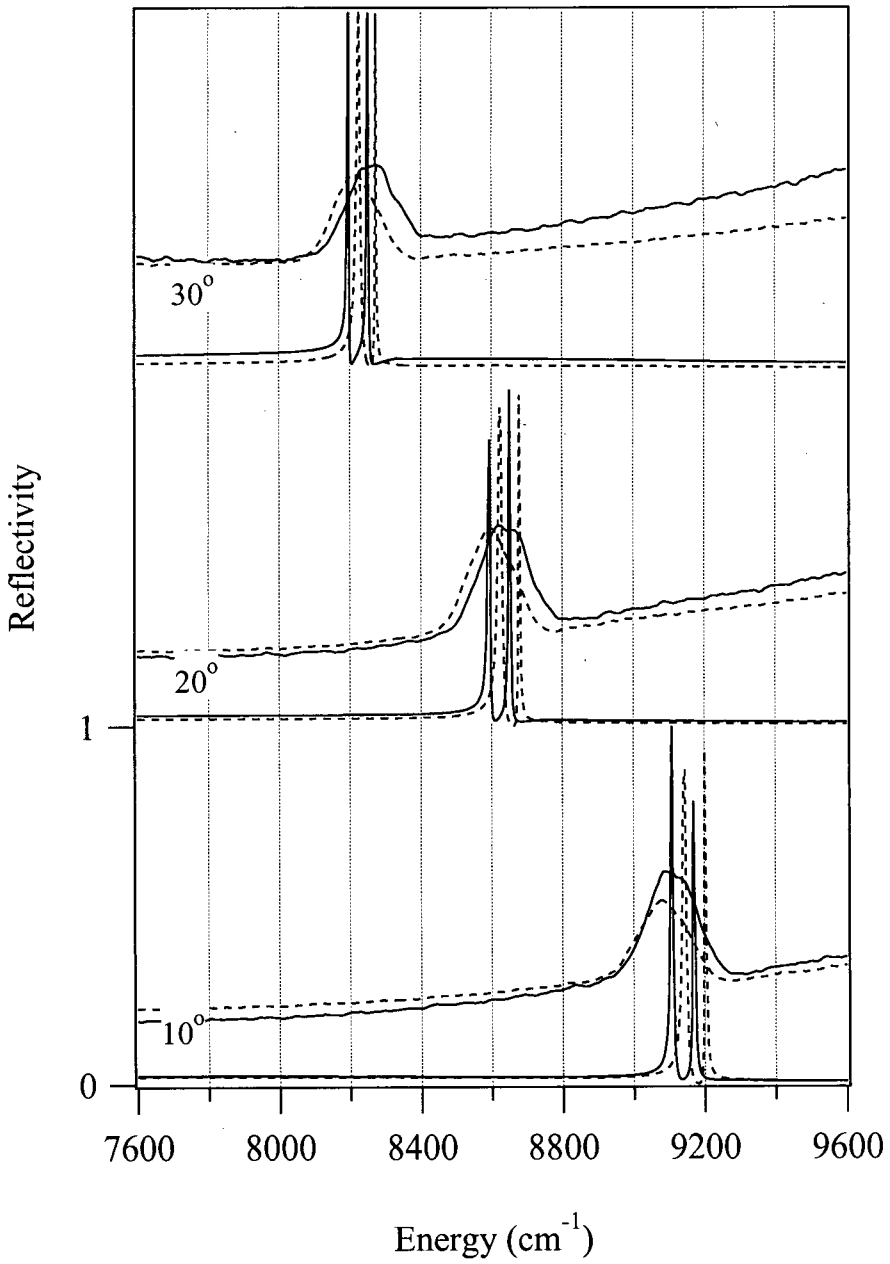

Figure 5.15: Simulation (narrow features) and data (broad features) for the textured polymer waveguide for 10°, 20° and 30° angles of incidence along the M direction. Note: the data are not plotted on an absolute scale. S-polarized spectra are represented by the solid lines, and p- by the dashed lines.

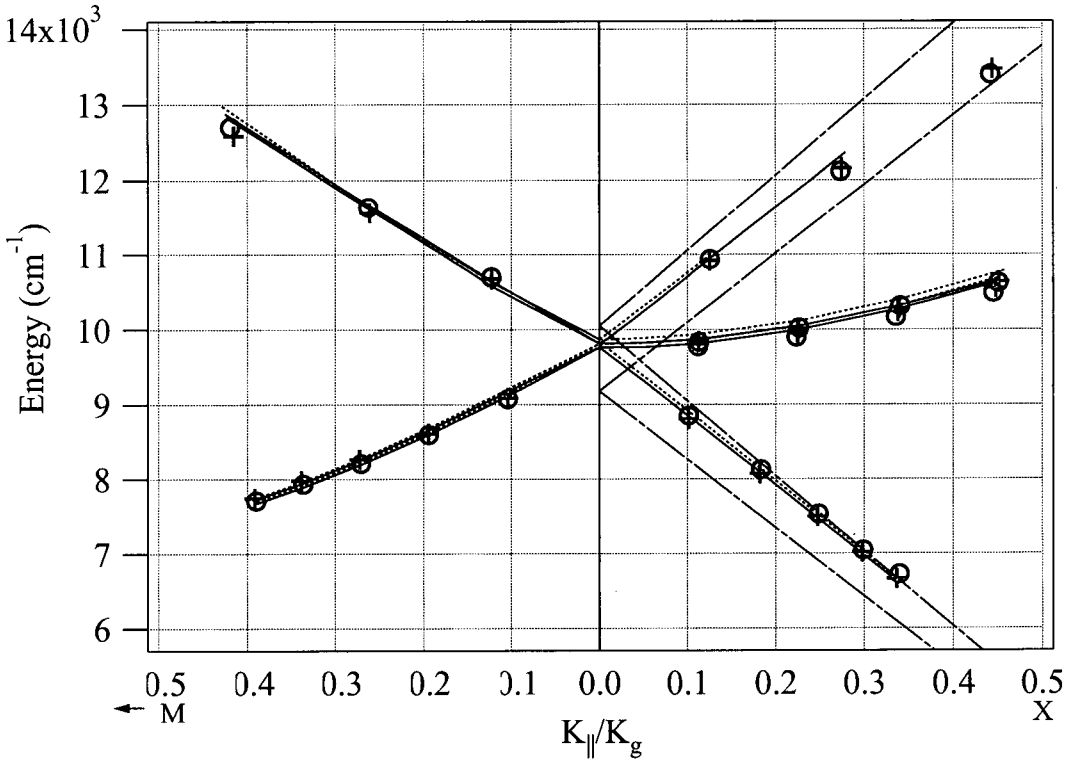

Figure 5.16: Dispersion diagram for textured planar waveguide with 2D polymer grating discussed in the text. Data values are shown as circles and crosses for s- and p-polarizations respectively. Simulations are shown as solid lines and dashed lines for s- and p-polarizations respectively. The light lines are represented by dot-dashed lines: the upper is the glass light line, and the lower is the polymer light line.

curvature of the lower and upper bands, and a slight upward curve of the central bands in the X direction. In the M direction the upward and downward dispersing bands show minimal curvature.

A dispersion diagram of this polymer waveguide *without* texturing would show a slightly curving band following the glass light line at low energies and transitioning gradually toward the polymer light line at higher energies. As evident in Figure 5.16, the

dispersion of this *textured* waveguide has the same basic characteristics as if it were untextured, with the exception of zone-folding. Thus the texturing is not greatly perturbing the band structure. When a grating serves as a weak perturbation evidenced by small gaps at zone boundaries, such as is the case with this polymer waveguide, the dispersion can be understood to follow simple kinematics. This means that the grating serves only to impart momentum in integer multiples to allow zone-folding, and does not strongly affect the dispersion characteristics of the waveguide. This occurs in this case essentially because the modes are quite weakly confined to the polymer due to the small dielectric contrast between the polymer and the glass. For this particular polymer waveguide, the dispersion follows simple kinematics.

This characterization of the textured polymer waveguide has demonstrated that this type of structure can exhibit relatively high resonant reflectivity and low non-resonant reflectivity. These traits make it well-suited for use as an optical filter, and in fact similar gratings of other materials are currently being used as polarization insensitive notch filters at normal incidence. [23] These devices strongly reflect a specific frequency range, while transmitting the remainder of the incident light. They take advantage of the fact that there is no distinction between s- and p-polarization at normal incidence for a symmetric two-dimensional lattice. Figure 5.17 shows a simulation of the reflectivity spectra for this polymer waveguide at normal incidence. Note the high, narrow band reflectivity and the low, non-resonant reflectivity, which would make this waveguide an excellent polarization insensitive notch filter. However, Figure 5.18 shows spectra for the same waveguide at a

1° angle of incidence. A change of just one degree causes considerable dispersion, making all eight modes clearly distinct, and rendering it ineffective as a polarization insensitive notch filter. Although progress has been made in decreasing the angle sensitivity of this type of filter [23], these designs are constrained to function at near-normal incidence due to the inherent dispersion characteristics of low index-contrast waveguides with two-dimensional texturing.

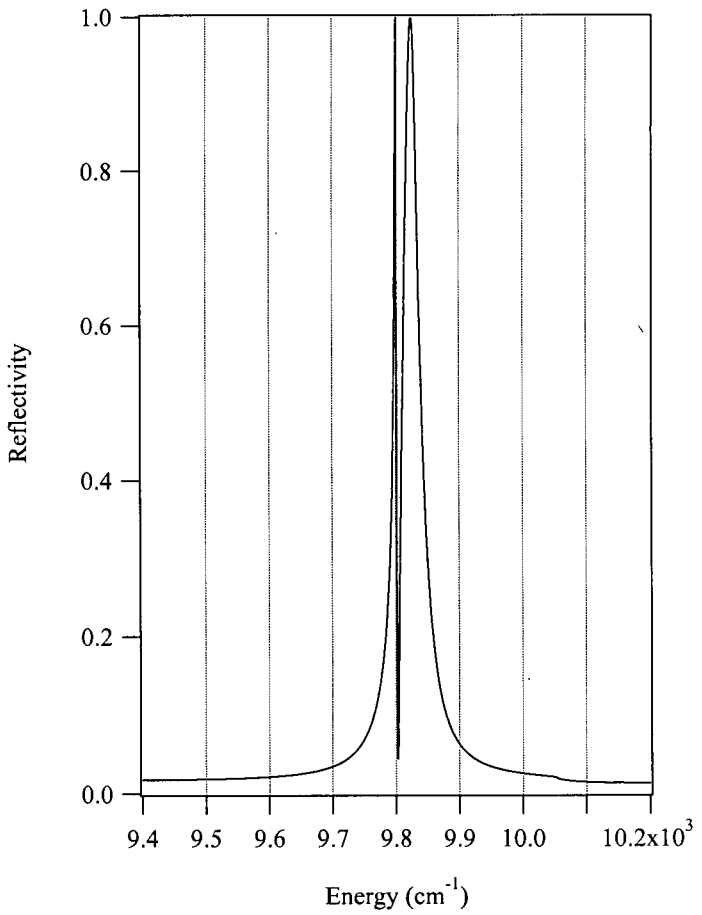

Figure 5.17: Simulated specular reflectivity of the textured polymer waveguide at normal incidence.

The polymer grating presented here has polarization insensitive reflectivity at angles

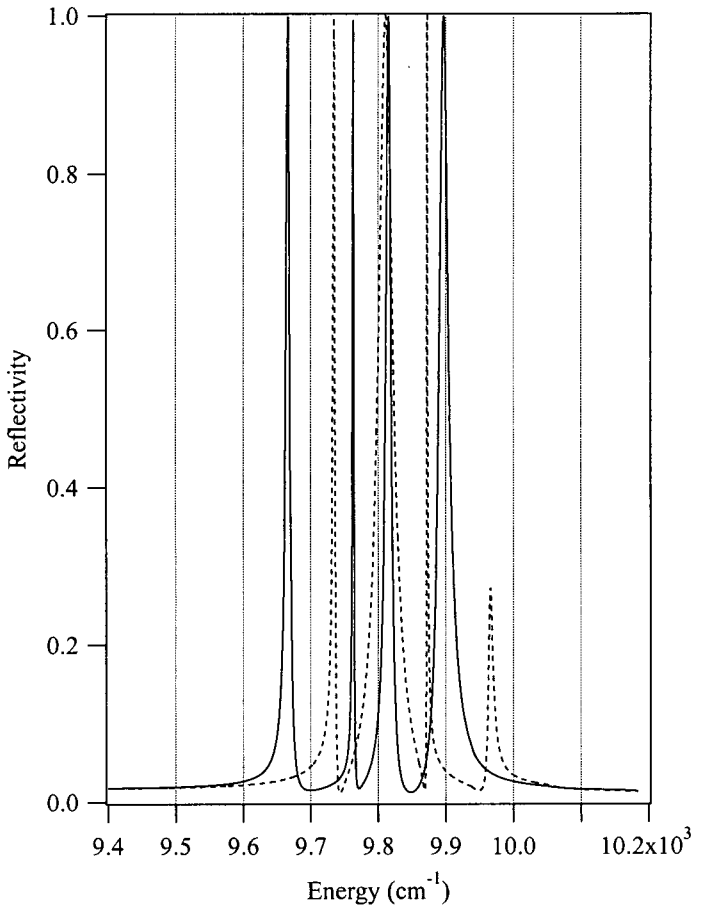

Figure 5.18: Simulated specular reflectivity of the textured polymer waveguide at 1° in the X direction. Solid lines represent s-polarization; dashed lines represent p-polarization.

far from normal incidence due to the significant overlap of the s- and p-polarized modes. Figure 5.19 shows an enlargement of the spectra from this sample at a 30° angle of incidence, in comparison with the simulated results at the same angle. Note again that the model shows the modes to be distinct and separate, which would indicate that this device would not be particularly useful. However, in the actual data the modes are clearly overlapping. This overlapping of s- and p-polarized modes, in conjunction with the strong resonant reflection and low non-resonant reflection, make the pDR1M polymer

textured planar waveguide particularly well suited as a polarization insensitive device which filters (i.e. reflects) a specific frequency range of incident light. In addition, the selected frequencies can be tuned by changing the angle of incidence, while maintaining polarization insensitivity.

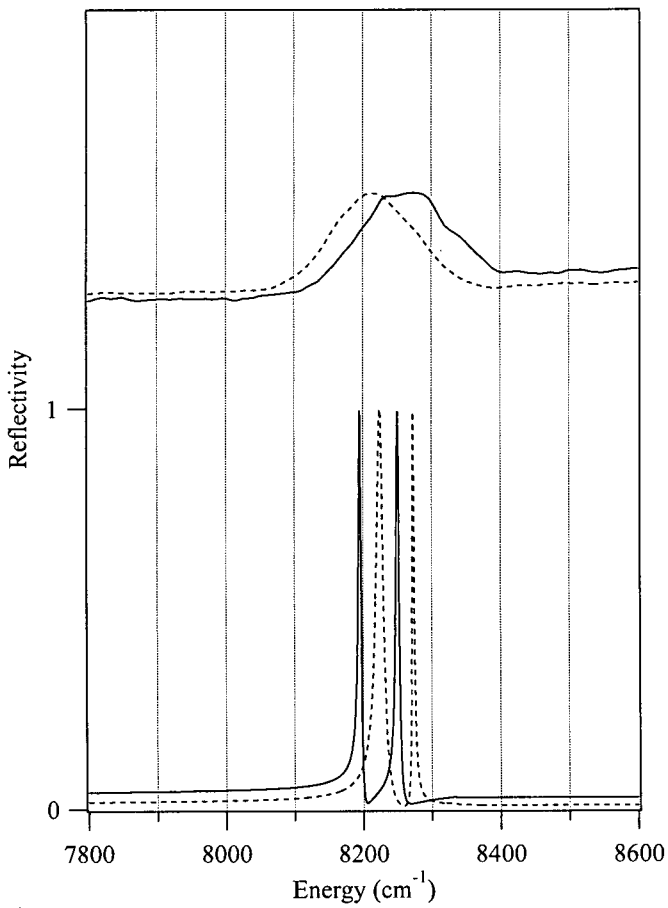

Figure 5.19: Specular reflectivity of the polymer waveguide at a 30° angle of incidence in the M direction. The top spectra are data, and the bottom are simulated. Note that the scale is specifically for the simulation. The s-polarized spectra are represented by solid lines; p- polarized spectra are represented by dashed lines. The peak reflectivities in the simulations go to unity.

Additionally, data was collected for the two orthogonal X symmetry directions. The

s-polarized specular reflectivity data for a 30° angle of incidence is shown in Figures 5.20 (a) and (b). In each spectrum the three mode groups are evident. However, there is a significant difference in oscillator strength between the two orthogonal directions. In Figure (a) the central modes are much stronger than the side modes, while in Figure (b) the situation is reversed. Note that the energies are the same for both orientations. Based on the kinematics discussion in Chapter 2, the high and low energy modes which disperse quickly up and down in energy are primarily due to coupling with the Fourier components parallel to the direction of incident radiation, while the modes which disperse slowly up in energy are primarily due to coupling with the Fourier components perpendicular to the direction of incident radiation. By rotating the waveguide 90°, the axes are switched. This is a clear sign that there is a difference in the strength of the Bragg scattering in the two orthogonal X directions. This is corroborated by AFM micrographs of this sample which show that in one direction the texturing periodicity is very regular, whereas in the other direction it is less regular.

Further, pDR1M appears to change over time. Figure 5.21 shows two AFM micrographs of the same pDR1M grating taken before and after a three month interval. A comparison of the two images shows a change in the grating morphology. In Figure 5.21(a), the amplitude of modulation is relatively uniform in both directions, while in Figure 5.21(b), the amplitude is much larger in one direction than it is in the other. The cause for this change is not known, but could be due to prolonged exposure to ambient

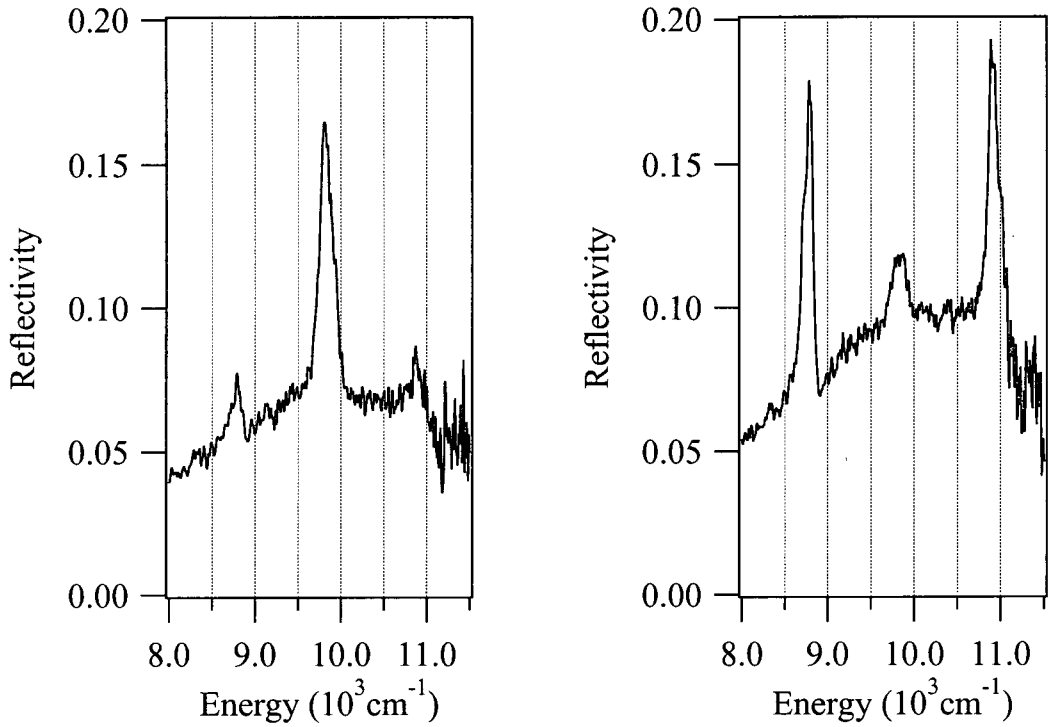

Figure 5.20: S-polarized specular reflectivity data for the polymer waveguide at a 10° angle of incidence along the X symmetry direction. The spectrum in Figure (a) was taken orthogonally (i.e. azmuthal angle of incidence was rotated 90°) to the spectrum in Figure (b).

light. Currently, the mechanism by which this polymer moves is not completely understood. Until further research on pDR1M determines the effects of long-term exposure to ambient light, it may not be possible to completely prevent structures made with this material from degrading, which may serve to limit its usefulness in applications.

Overall, the pDR1M polymer is an intriguing new material which holds promise for

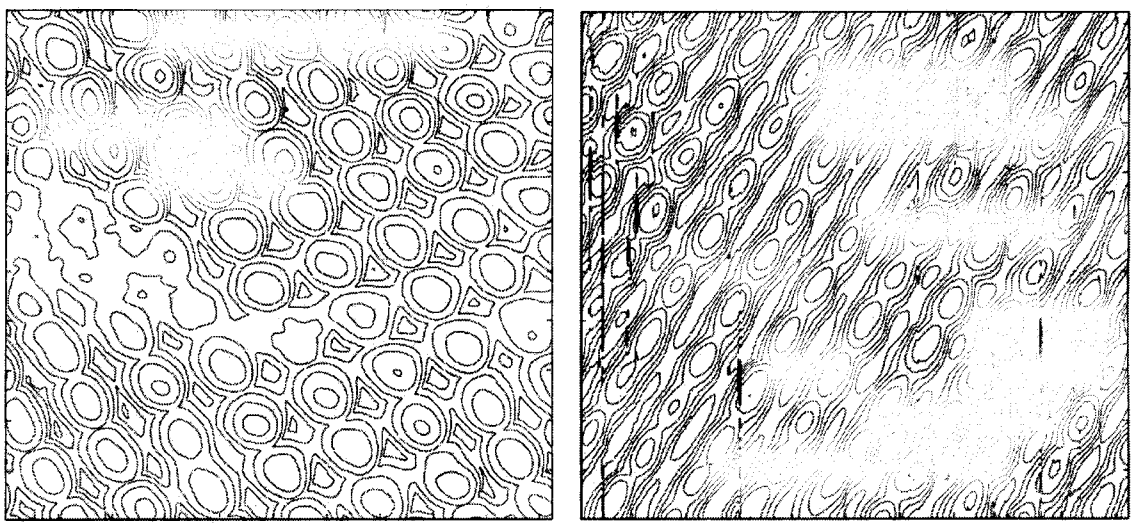

(a) Fresh polymer grating (b) Three month old polymer grating

Figure 5.21: Atomic force micrographs of two polymer square lattice gratings. The sample shown in Figure (a) was recently manufactured, while the one shown in Figure (b) was exposed to ambient light for approximately 3 months. Each contour line is 50 nm.

optical applications. The low index-contrast polymer waveguide characterized here provides an innovative medium for engineering low-cost devices requiring large area gratings. As an example, this polymer has been shown to exhibit properties that could be further engineered to realize a polarization insensitive notch filter. It should be noted, however, that this sample was not optimized for this purpose.

5.2.2 Flat Photonic Bands Along the Entire Γ–X Line of a 2D Square Lattice

From analyzing the previously discussed triangular lattice and square lattice waveguides with high index-contrast gratings, the square lattice seems to offer the greater potential

for *engineering* a flat band (or bands) that extend across the first Brillouin zone. It has been shown that a band exhibiting low group velocity ($v_g = \delta\omega/\delta k$) offers an increase in the efficiency of certain non-linear processes inside bulk photonic crystals. [28–30] Therefore a waveguide was designed with a square lattice in such a way as to optimize the flatness of one of the bands. This exercise served to test the ability to design and realize a textured planar waveguide with a specific, intended band structure.

In designing this structure, a 150 nm thick waveguide core was selected, which is thicker than that used in the previously described GaAs samples, because a thicker waveguide provides a richer band structure than a thinner one, increasing the potential for achieving flat bands. This richer band structure occurs because in a thicker waveguide the TE and TM slab modes are closer together in energy. When a thicker waveguide is textured with a high index-contrast grating, the modes from the TE-like gap and the TM-like gap are closer together, providing anti-crossings closer to zone center. With more bands anti-crossing, there is more interaction between the bands and thus more potential for flat bands to occur.

Modeling this structure required the use of the modification to the code which allows for the modeling of thick gratings. With this modification, the 150 nm thick core was modeled as two layers. The specific values used for the modeling are given in Table 5.4. The computer-modeled band structure of the waveguide is shown in Figure 5.22.

In this theoretical dispersion diagram, the lowest four bands near zone center can be loosely associated with the TE slab mode gap. As expected for a square lattice, there are

Table 5.4: Key modeling parameters for "flat band" structure

Parameter	Value
Pitch	390 nm
Hole radius	90 nm
Thickness of textured layer	2x70 nm
Thickness of oxide layer	1000 nm

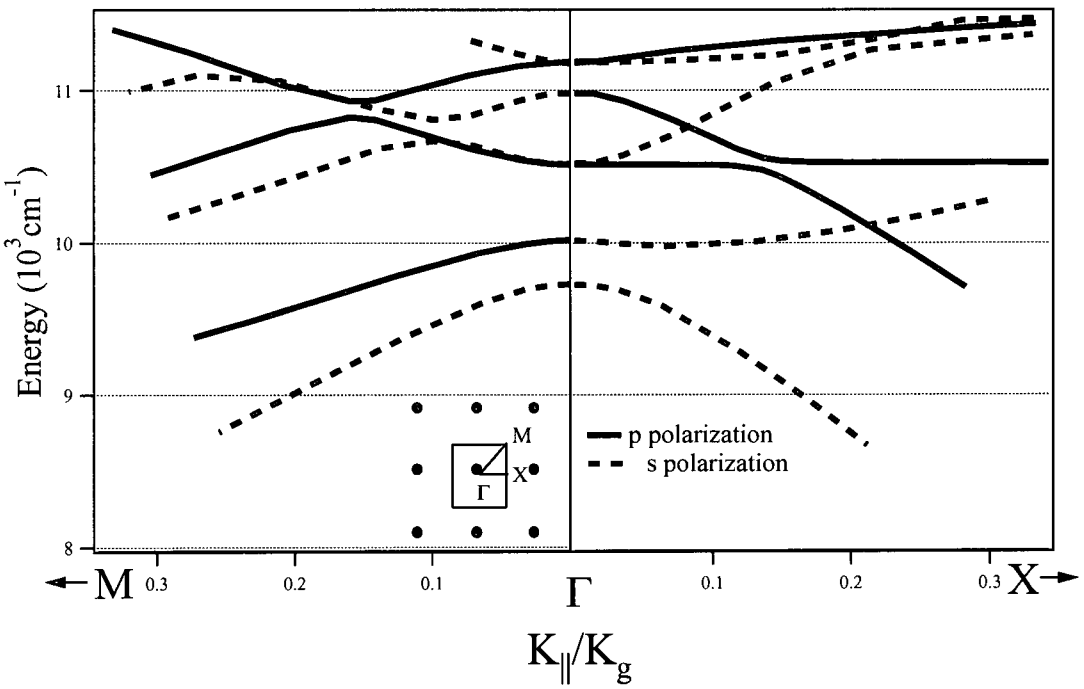

Figure 5.22: Theoretical dispersion diagram for the 150 nm thick textured planar waveguide with the square lattice discussed in the text. Note the p-polarized, low-dispersion bands near 10,000 cm^{-1}. [17]

four bands in the X direction: two dispersive s-polarized bands, as well as one s- and one p-polarized band that are less dispersive. The next higher set of bands can be loosely associated with the TM slab mode gap. At the TM-like gap the two dispersive modes

are expected to be p-polarized, and the two less dispersive modes to be one s- and one p-polarized. [20] Only the three lower-energy bands are plotted because the highest energy p-polarized band occurs above the GaAs absorption edge (11,400 cm^{-1}) and thus does not show up in the simulation. Note the extremely flat "band," that actually consists of two p-polarized bands, which occurs in the X direction and originates at the top of the TE-like gap. [17] Modeling shows the first of these two bands to originate at 10,390 cm^{-1} at zone center. It remains flat across 25% of the Brillouin zone, where it anti-crosses with the second band, then curves downward in energy. Beyond the anti-crossing the second band becomes nearly dispersion free at a slightly higher energy (10,445 cm^{-1}) than the first band. This band continues across the remainder of the Brillouin zone, where at zone edge it has an energy of 10,452 cm^{-1}. Thus the overall dispersion is only 62 cm^{-1} across the entire Brillouin zone. The flatness of this band is a consequence of the p-polarized band from the TE-like gap anti-crossing with the downward dispersing p-polarized band from the TM-like gap. The simulated specular reflectivity spectra for this design is shown in Figure 5.23.

A textured planar waveguide for this flat band was fabricated using ASU506, which consists of 150 nm of GaAs on top of 1.0 μm of $Al_{0.98}Ga_{0.02}As$ on a GaAs substrate. A square lattice of circular holes 390 nm apart with a radius of 90 nm was etched completely through the waveguide core. Every fifth hole was omitted, creating a defect superlattice. The $Al_{0.98}Ga_{0.02}As$ layer was fully oxidized.

The specular reflectivity data at various angles of incidence along the Γ–X direction

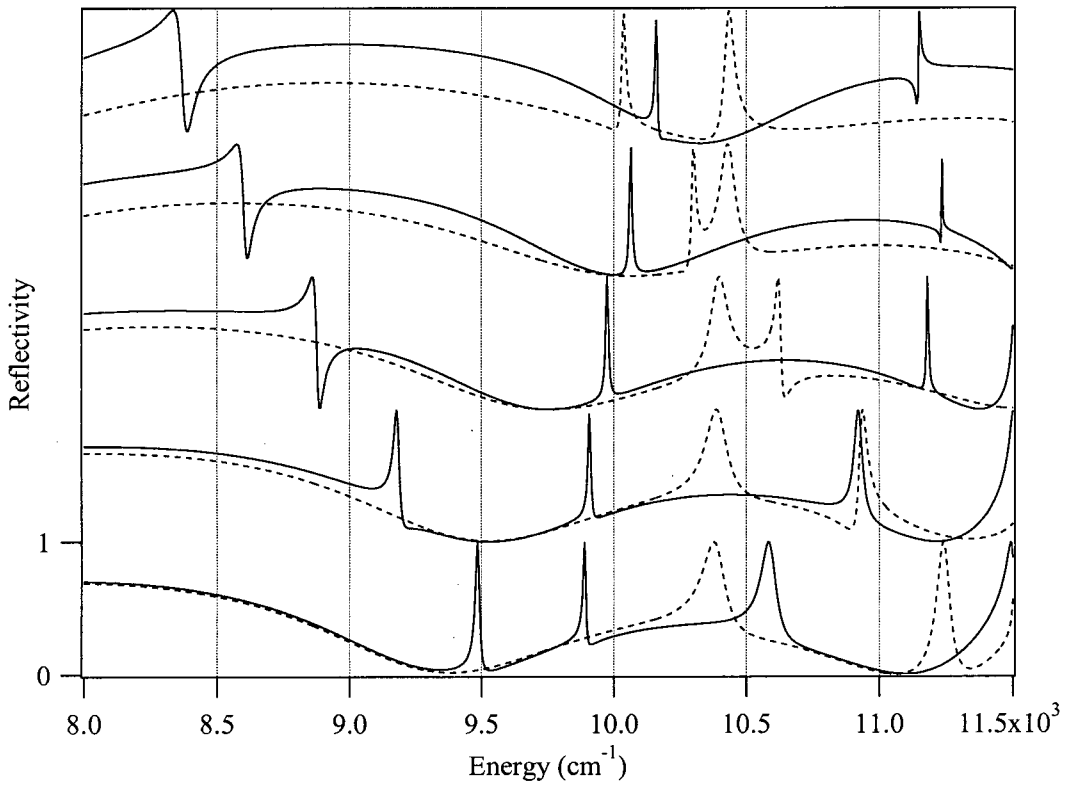

Figure 5.23: Simulation of specular reflectivity for the 150 nm thick textured planar waveguide with the square lattice discussed in the text. The spectra correspond to angles of incidence of 10°, 20°, 30°, 40° and 50° from the bottom up. The solid lines represent s-polarized simulations. The dashed lines represent p-polarized simulations.

are shown in Figure 5.24. All the modes from the TE-like gap and the lowest p-polarized mode from the TM gap are evident. There is an s-polarized mode that disperses down in energy from $\sim$9,500 cm^{-1} to $\sim$8,300 cm^{-1}. There is a relatively flat s-polarized mode near $\sim$10,000 cm^{-1}. There is also a faint s-polarized mode beginning at $\sim$10,600 cm^{-1} and dispersing up in energy, which is lost in the GaAs absorption above $\sim$11,400 cm^{-1}. There is one p-polarized mode starting at $\sim$11,100 cm^{-1} and dispersing down, which anti-crosses with the p-polarized mode at $\sim$10,400 cm^{-1}, as predicted in the simulation. Due

to the broad nature of the Fano-resonances associated with the flat band, it is difficult to fit these specular data to the accuracy needed in order to determine the precise dispersion of this band. Therefore a defect superlattice was included in the design so that more precise measurements could be taken with the new diffraction measurement technique (as will be discussed in Section 5.3.1). Qualitatively, the dispersion of the bands from this textured planar waveguide with a defect superlattice agrees well with the theoretical predictions for the dispersion of a waveguide with a simple lattice.

To summarize, the waveguide discussed herein exhibits a nearly dispersion free (<1%) mode across the entire Brillouin zone in the X direction. This flat band was observed experimentally up to a 50° angle of incidence, which is more than 30% of the way across the Brillouin zone. However, due to the close proximity and breadth of the modes, the exact mode positions and lifetimes can not be reliably extracted using the numerical fitting technique mentioned in Section 5.1.1. To measure the precise position and lifetimes of these types of modes, the background-free measurement technique described in Chapter 2 was used. These results are discussed in the following section.

5.3 Waveguides with Defect Superlattices

The 2D textured planar waveguides in the previous sections were characterized using specular reflectivity to probe the low-lying resonant bands. While this measurement technique has proven useful in terms of quantitative comparisons between model and experiment, it has some limitations. The Fano-like features in the reflectivity spectra

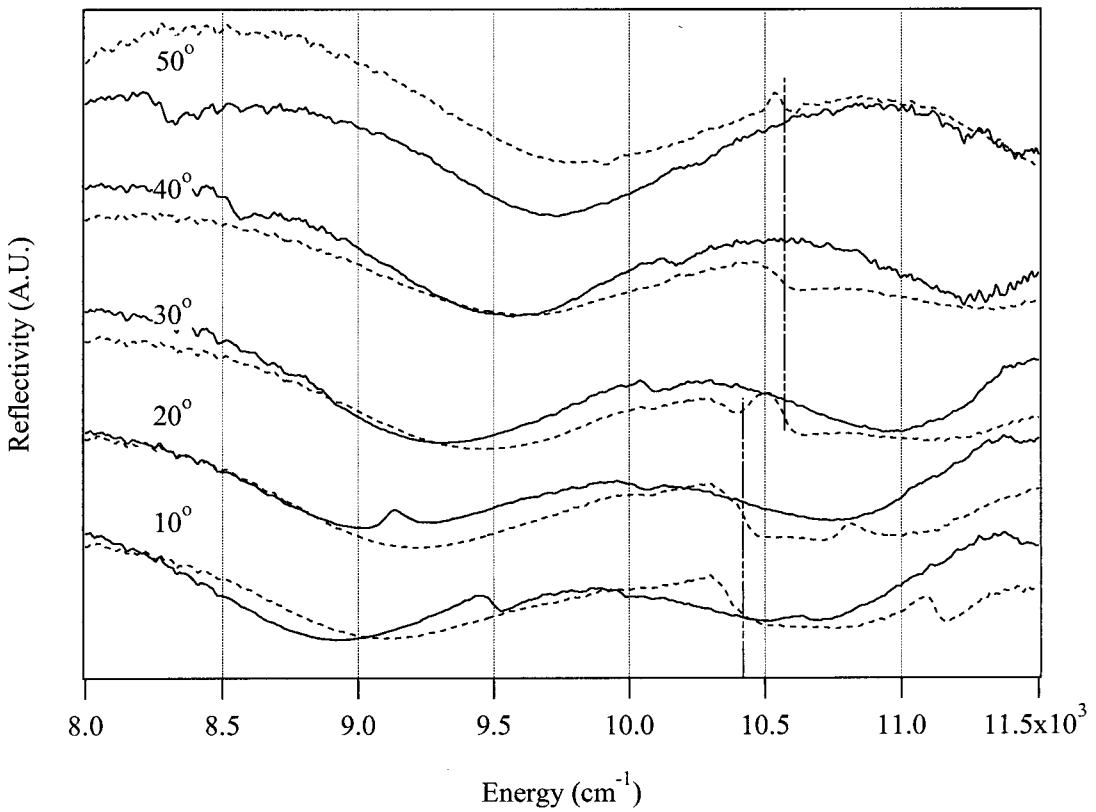

Figure 5.24: S-polarized and p-polarized specular reflectivity data, represented by solid and dashed lines respectively, for the 150 nm thick textured planar waveguide with a square lattice referred to in the text. The spectra correspond to angles of incidence of 10°, 20°, 30°, 40° and 50° from the bottom up. Near 10,400 cm^{-1} these spectra exhibit flat p-polarized bands, as indicated by the dot-dashed lines.

used to extract the mode profiles are sometimes difficult to distinguish from the non-resonant background reflectivity. In addition, this technique probes modes above the light line only, and does not offer access to the band structure below the light line. Both of these limitations can possibly be addressed by incorporating in the texture pattern a "defect superlattice" that weakly perturbs the band structure of the underlying "base lattice."

A defect superlattice couples a small amount of light out of the waveguide in a non-specular direction via the Fourier coefficients of the defect superlattice, which in theory allows mapping of the band structure of base lattice modes below the light line, while at the same time enabling a background-free method for viewing the modes above and below the light line. It is desirable to characterize modes below the light line of the base lattice because these modes do not have radiative components, and thus have the potential to efficiently transmit information in-plane for device applications.

In some cases, a defect superlattice introduces a "defect band" that appears inside the pseudo-gap characteristic of the base lattice (see Section 2.1.3). This band can occur whether or not the defect superlattice has a significant affect on the underlying base lattice structure.

The author is unaware of any other published work that considers this application of defect superlattices as a means of extending the utility of white light scattering as a powerful probe of the *entire* band structure of plain photonic crystals. This section describes work aimed at evaluating the practical utility of this novel concept. This method of probing the band structure of textured planar waveguides is explored both experimentally and theoretically via characterization of three waveguides: the previously discussed "flat band" square lattice as well as the previously discussed triangular lattice, and an additional waveguide with a triangular lattice. The method proves especially useful in characterizing low-dispersion bands above the light line. The usefulness of the technique in probing other bands, such as in the triangular lattice structures, is dependant

upon the degree to which the defect superlattice perturbs the modes of the underlying base lattice. Finally, this section describes a textured planar waveguide design in which a defect band exists within a complete pseudo-gap. The potential use of such a structure as the basis for a broad band angle and polarization insensitive notch filter is discussed.

5.3.1 Superlattice Scattering from a Low Dispersion Band

This section explores the use of the diffraction measurement technique to further analyze the GaAs "flat band" textured planar waveguide sample described in Section 5.2.2. Recall that this waveguide has a square base lattice of holes with a defect superlattice that omits every fifth hole of the base lattice in the x and y direction. This grating pattern is clearly evident in the scanning electron micrograph of this sample shown in Figure 5.25. Note that the orientation of the lattice in this picture is indicative of the pattern on the actual sample: the lattice is on a $90\,\mu$m x $90\,\mu$m portion of the waveguide, and the square pattern is rotated 22.5° within the $90\,\mu$m x $90\,\mu$m square. This was done to prevent the square aperture diffraction pattern from interfering with the collection optics during diffraction data collection.

To obtain the diffraction data for the region of the band structure containing the flat bands, the experimental apparatus was oriented to collect the diffraction spectra from the $-K_g^D$ diffracted order at an energy of $10{,}000\,\mathrm{cm}^{-1}$ (the approximate location of the flat bands). This required adjustment to the sample mount, as well as the incident light, for each angle of incidence. To calculate the angles for the orientation of the apparatus

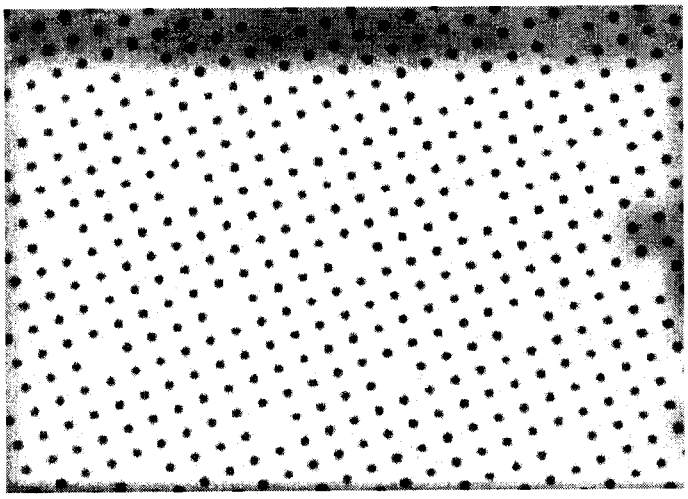

Figure 5.25: SEM micrograph of the textured planar waveguide with a square lattice fabricated using ASU506. The air filling fraction is 18%. The pitch of the lattice is 390 nm. The thickness of the GaAs core is 150 nm.

the following equations are used

$$K \sin\theta_{in} - K_g^D = K \sin\theta_{out} \tag{5.1}$$

where

$$K_g^D = \frac{1}{\Lambda^D} \tag{5.2}$$

and

$$K = \frac{1}{\lambda} \tag{5.3}$$

and where Λ^D is the spacing between defects.

Diffraction spectra were collected for the same angles of incident light as were used to obtain the specular reflectivity spectra shown in Figure 5.24. Figure 5.26 shows the experimental data for the -K_g^D diffracted order while Figure 5.27 shows the simulated -K_g^D diffracted order. The spectra presented here are raw data, as opposed to the normalized[5] data presented for the specular reflectivity spectra.

The non-dispersive (flat) s- and p-polarized bands from the TE-like gap, as well as the downward dispersive p-polarized band from the TM-like gap, occur within the selected energy range. The simulation for this energy range, shown in Figure 5.27, produces two modes: a higher energy p-polarized mode and a lower energy s-polarized doublet. For the experimental data, a polarizer was used to confirm that the higher energy mode is p-polarized and the lower energy doublet is predominantly s-polarized. In both the data and the simulation, the p-polarized mode near 10,400 cm^{-1} is clearly evident. Slightly lower in energy there is a less intense s-polarized doublet. Both the s- and p-polarized modes show little dispersion up to a 30° angle of incidence, where the s- modes become undetectable. At approximately 40° the p-polarized mode becomes a broad doublet, then at 50° returns to a (now asymmetric) single mode, centered at a slightly higher energy. Overall there is striking qualitative agreement between the data and the simulation.

It is now possible to quantitatively compare the linewidth of the modes from the simulation with the actual linewidths from the raw data. Previously, when using data taken with the specular measurement technique, the linewidth would have had to be

[5]Specular reflectivity data is normalized by dividing the collected spectra by the spectra from bare GaAs.

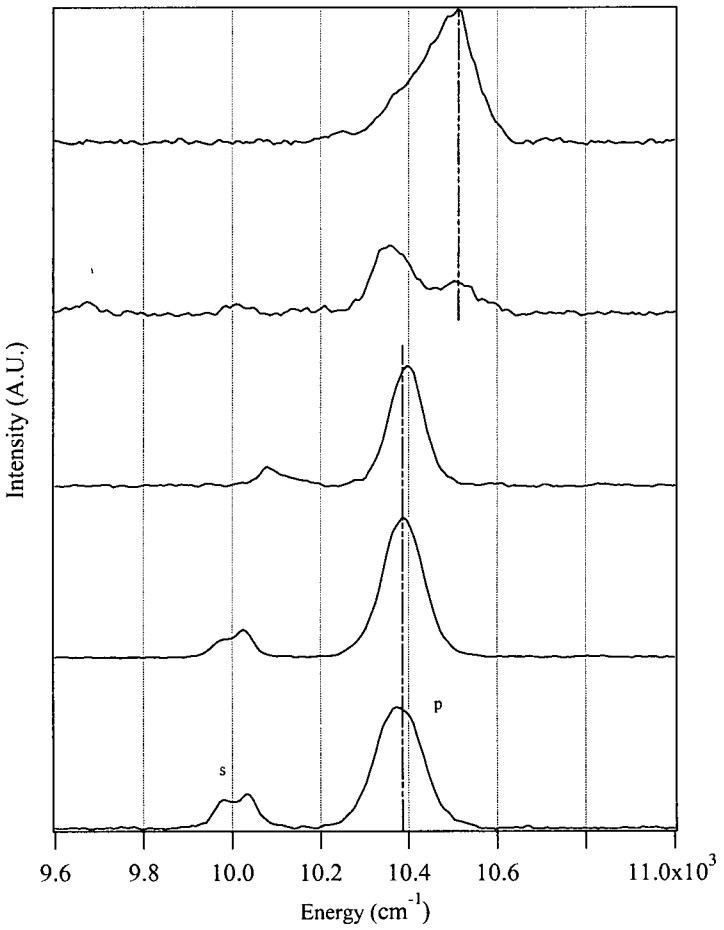

Figure 5.26: Diffraction spectra for the -K_g^D diffracted order from the defect superlattice of the textured planar waveguide with a square lattice for incident angles of 10°, 20°, 30°, 40° and 50°, from the bottom up.

calculated with the mathematical fitting technique, as described in Section 5.1.1. This method is not well-suited for calculating the linewidth for closely spaced modes, such as the ones associated with the anti-crossing seen here. When using the new diffraction measurement technique, the linewidth is immediately available in the raw data. Thus, there is little uncertainty in this measurement, and artifacts are not introduced by the fitting procedure. Specifically for the flat band, the simulation shows the linewidth for

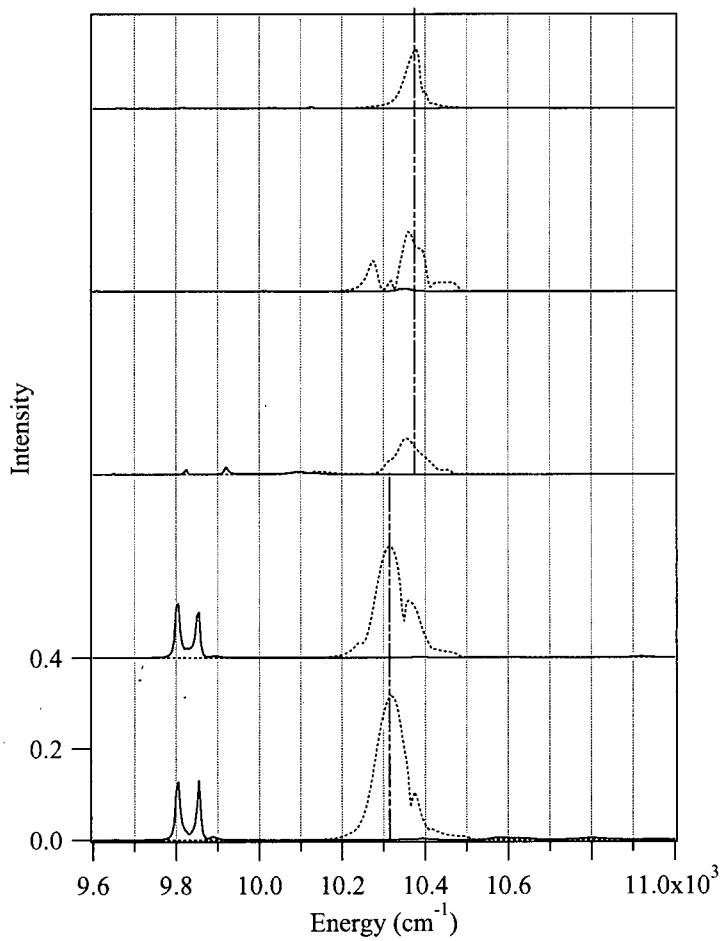

Figure 5.27: Simulated p-polarized diffraction spectra (dashed lines) and s-polarized diffraction spectra (solid lines) for the $-K_g^D$ diffracted order from the defect superlattice of the "flat band" sample for incident angles of 10°, 20°, 30°, 40° and 50°, from the bottom up.

the p-polarized band to be $97\,\mathrm{cm}^{-1}$ at 10°. In the experimental data, the linewidth for the p-polarized band is $150\,\mathrm{cm}^{-1}$ at 10°. The mode is broader in the data than in the simulation, which is likely due to the modes being effected by physical imperfections which are not taken into account by the simulation. Slight irregularities in the texturing of this waveguide are suspected of causing some degree of broadening of the modes, as

was suspected to be the case for the polymer waveguide discussed in Section 5.2.1. The diffraction measurement technique removes one significant source of uncertainty, allowing a more precise, quantifiable evaluation and comparison of the lifetimes of these modes. The $\sim 50\,\mathrm{cm}^{-1}$ differential in the measured and simulated bandwidths is consistent with the linewidth comparisons done by V. Pacradouni on the square lattice sample of Section 5.1.1, using only specular data.

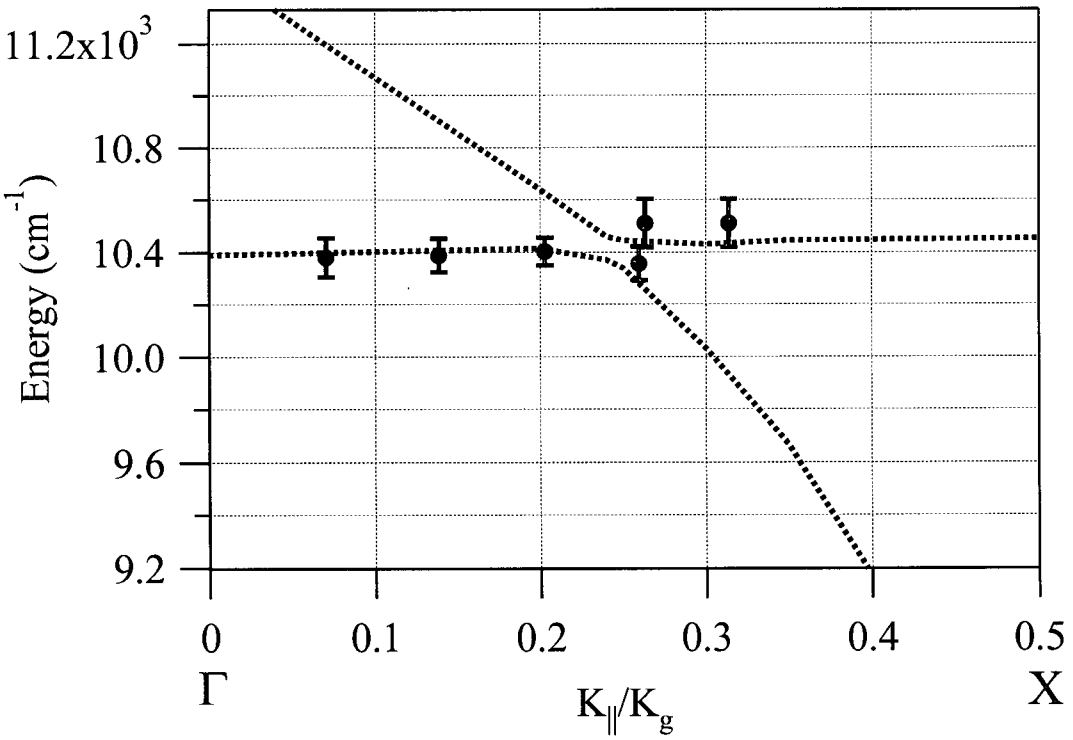

Figure 5.28: Dispersion diagram of the flat p-polarized bands showing simulation and data. Dotted line represents the simulation for the base lattice. Large dots represent central location of the mode derived experimentally via the $-K_g^D$ diffracted order. Error bars on data points represent the width of gaussian fits to mode profile from diffraction data.

Qualitatively, the position of the modes in the simulation has good agreement with

the modes in the data. This comparison is made more easily quantifiable by the diffraction measurement technique. With specular reflectivity data, the mathematical fitting technique can be used to approximate the position of the modes. However, when modes are positioned close together, this method is problematic. The diffraction technique facilitates reliable, precise position extraction without complicated mathematical fitting, thus allowing easy calculation of dispersion. For the p-polarized band depicted in Figure 5.26, the data show a 1.0% dispersion over more than 30% of the Brillouin zone, while the simulation predicts 0.6%. There is only 0.4% difference between the theoretical and measured dispersion; the level of accuracy to which this is measured is not possible with the specular measurement technique. Figure 5.28 shows the simulation of the flat p-polarized bands and the mode locations from the diffraction data.

To further investigate these low dispersion bands, the computer code was used to extract the strength of the p-polarized Fourier field components for various values of in-plane wavevector. Figure 5.29 shows momentum space diagrams of these results. Figures (a)–(c) are for the upper band, that originates from the TM-like gap and anticrosses, becomming flat, whereas Figures (d)–(f) are for the lower band, that originates from the TE-like gap and then disperses down in energy after the anticrossing. Prior to the anticrossing, the upper band is primarily comprised of TM field components. After the anticrossing it is composed mainly of TE field components. This is evident for this p-polarized band because the single dominant Fourier coefficient lies on the line of symmetry before the anticrossing. After the anticrossing the strong Fourier coefficients

occur in symmetric pairs, which add asymmetrically to produce a p-polarized mode. The lower band starts near zone center primarily composed of TE field components and transitions to being composed primarily of a TM field component after the anticrossing.

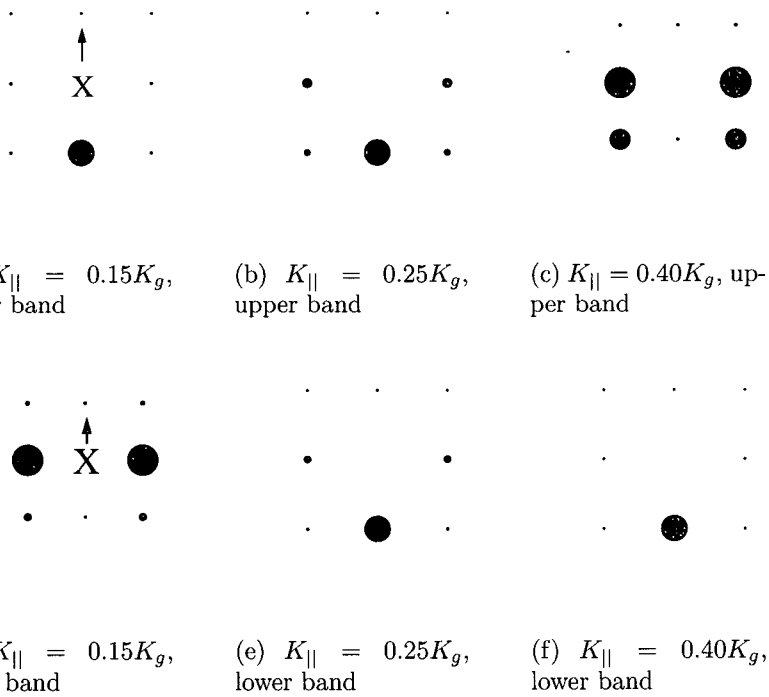

(a) $K_{||} = 0.15K_g$, upper band (b) $K_{||} = 0.25K_g$, upper band (c) $K_{||} = 0.40K_g$, upper band

(d) $K_{||} = 0.15K_g$, lower band (e) $K_{||} = 0.25K_g$, lower band (f) $K_{||} = 0.40K_g$, lower band

Figure 5.29: Momentum space diagrams of low dispersion bands before and after the anticrossing. The strength of each Fourier component is indicated by the size of the dot. Figures (a)–(c) correspond to the band that originates at the bottom of the TM-like gap. Figures (d)–(f) correspond to the band that originates near the top of the TE-like gap.

When comparing the spectra obtained using the diffraction technique with that obtained with the specular measurement technique, there are two notable discrepancies. First, the downward dispersive p-polarized mode evident in the specular reflectivity data is conspicuously missing from the diffraction data. This mode is also absent from the simulated diffraction spectra. Although the band itself is not visible, at 40° there is clear

evidence of it anti-crossing with the flat band. Secondly, the lower energy s-polarized feature that appears faintly in the specular reflectivity data is clearly shown in the diffraction data to be a doublet. Simulations of this mode with wider defect spacing show this doublet to be a single mode, as it has to be in the absence of the superlattice.

The diffraction measurement technique has been shown here to enable background-free probing of these low dispersion bulk modes. In addition, using this technique to further characterize flat bands has improved the level of quantifiable results using this type of white light probe technique.

5.3.2 Superlattice Diffraction from Triangular Lattice Structures

For the planar waveguide discussed in the previous section, both the experimental and the theoretical diffraction results were completely dominated by modes associated with flat bands lying above the air light line. To investigate the use of the diffraction measurement technique to probe more dispersive modes, a planar waveguide was selected which is textured with the previously described triangular lattice configuration, known to exhibit relatively dispersive bands. This section reports experimental and theoretical studies of defect diffraction from two samples of this waveguide which differ only in the lattice constant of the defect superlattice. For the technique to provide an effective means of probing the underlying base lattice band structure, the defect superlattice must act only as a weak perturbation. "Weak" here implies that the actual band structure rendered

in the first Brillouin zone of the superlattice can be interpreted as trivial, kinematic zone-folding of the bands characteristic of the base lattice structure (as illustrated in Figure 2.7).

Figure 5.30 illustrates the same ideas in a slightly different way. Here "weak" superlattice is described as causing a small renormalization of the (already renormalized) bands characteristic of the base lattice. If the gaps at the defect zone boundaries are small, then the diffraction from the various defect lattice vectors should follow the base lattice dispersion. The dark line in Figure 5.30 labelled "0" represents the parameter space stimulated directly by white light at a well-defined angle of incidence. This is the parameter space probed by the specular measurement technique, as described in Section 2.3.1. The lines parallel to the zeroth order represent additional points in parameter space probed by adding or subtracting integer multiples of the defect lattice grating vector. The spectra obtained from any of these diffracted orders (including specular) should show signs of coupling into this mode via various multiples of K_g^D represented by all of the intersections. For this example, the $+K_g^D$ diffracted spectra might be expected to dominantly show this mode background-free at a higher energy than seen in the specular reflectivity spectra; this mode should continuously disperse up in energy as the angle of incidence of the probe beam is increased. In the -K_g^D diffracted order, when the probe beam is near normal incidence the mode should appear higher in energy than it does in the specular; as the angle of incident light is increased, the mode should disperse down in energy until zone center, where it should "turn around" and disperse up in energy.

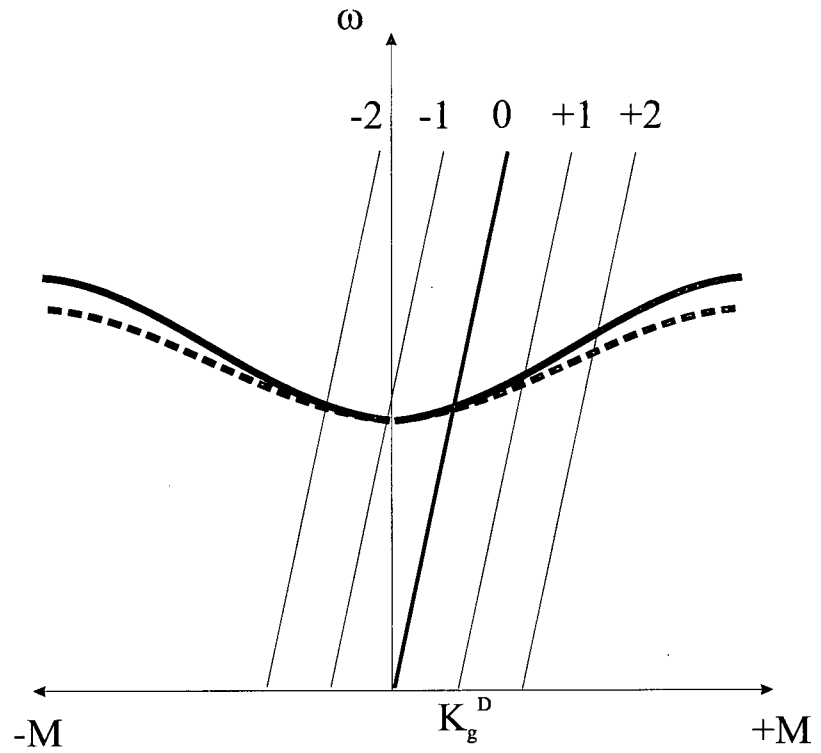

Figure 5.30: Schematic diagram illustrating the diffraction probe technique. The bold, straight line at 0 represents the parameter space directly stimulated by the incident light. The dashed line represents the upper most p-polarized band, and the solid represents the upper most s-polarized band of the triangular lattice structure (see Figure 5.6).

At some point as the defect lattice spacing becomes comparable to the base lattice spacing, this simple interpretation of renormalizing the already renormalized base-lattice modes cannot be used effectively. Instead, the band structure must be interpreted in terms of the renormalization of the slab modes by a complex unit cell which includes the defect superlattice. For example, consider a triangular lattice with a defect superlattice which omits every fifth hole. The unit cell for this lattice contains nineteen sites, as opposed to the non-defect version of this lattice, which contains only one. So, where previously seven Fourier coefficients were sufficient to describe the band structure near

the second order gap, now ninety-one Fourier coefficients must be used to describe the renormalized band structure to the same accuracy.

To evaluate the diffraction technique's efficacy in revealing the band structure of the underlying base lattice, two samples are investigated: the GaAs waveguide described in Section 5.1.2, which has a defect superlattice with every seventh hole omitted, referred to as T-7; and a similar GaAs waveguide with every fifth hole missing, referred to as T-5. A scanning electron micrograph of T-5 is shown in Figure 5.31. The experimental apparatus was oriented to collect diffraction data from $\sim$10,000 cm^{-1} because this is the range of energies where the second order gap from the base lattice grating is located, as determined via specular reflectivity measurements. The angles required to orient the sample were calculated using Equation 5.1 with $K_g^D = \frac{2}{\sqrt{3}\Lambda^D}$. The samples were oriented so that the light was incident along the M direction. The diffraction data was collected without a polarizer due to the low signal strength.

The -K_g^D diffraction data for T-5 are shown in Figure 5.32. The modes which are evident in the bottom four spectra (2°, 4°, 6° and 8°) are dispersing down in energy. No data could be collected between 8° and 14° since the signal for these angles is physically blocked by the apparatus. The top four spectra, which correspond to angles of incident light of 14°, 16°, 18° and 20°, show modes which are generally dispersing up in energy. Figure 5.33 shows the $+K_g^D$ diffraction data from sample T-5. This data was collected for angles of incident light of 2°, 4°, 6°, 8°, and 10°. There are no well-defined modes, but there is an upward trend in the dispersion of the weak structures in these spectra. The

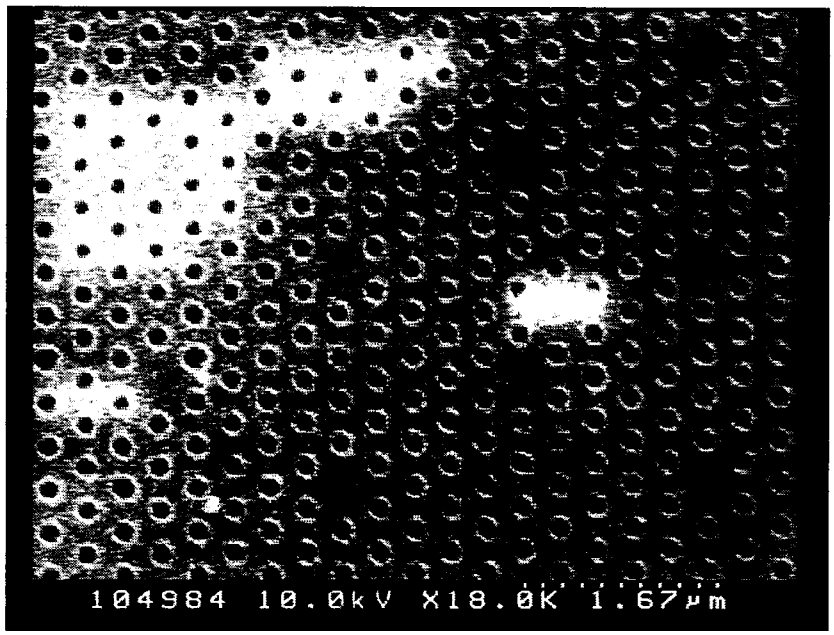

Figure 5.31: Scanning electron micrograph of T-5 sample: a planar waveguide textured with a triangular base lattice, with a defect superlattice 5x the period of the base lattice. This waveguide was fabricated using ASU721, and the pitch of the lattice is 600 nm.

diffraction signal in the $+K_g^D$ direction is ~5x weaker than that in the $-K_g^D$ direction.

Table 5.5: Key modeling parameters for T-5

Parameter	Value
Pitch	560 nm
Hole radius	70 nm
Thickness of textured layer	73 nm
Thickness of oxide layer	300 nm

Simulations were performed for T-5 using the parameter values in Table 5.5. The simulation results are shown in Figure 5.34 for the $-K_g^D$ and Figure 5.35 for the $+K_g^D$ diffraction directions. For the $-K_g^D$ diffracted order, a group of s- and p-polarized modes disperses down in energy for incident angles from 2° to 12°, then "turns around" and

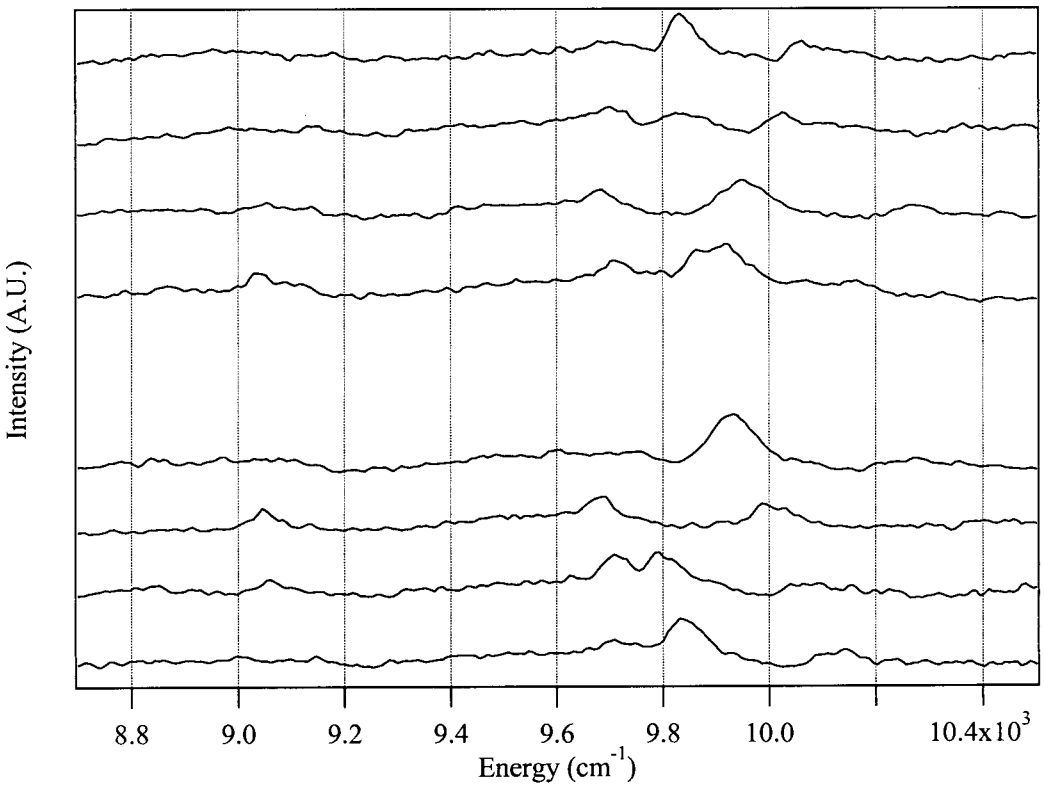

Figure 5.32: Unpolarized -K_g^D diffraction data for T-5. Spectra from the bottom up are for incident angles of 2°, 4°, 6°, 8°, 14°, 16°, 18°, and 20°.

disperses up in energy through 20°. This "turn around" is located at the point where these bands pass through the first defect Brillouin zone boundary, which is consistent with the data in Figure 5.32. For the $+K_g^D$ diffracted order, there are several modes of both s- and p-polarization which disperse up in energy for all angles of incidence from 2° to 20°. This is qualitatively consistent with the behavior of the weak peaks in Figure 5.33. The calculated intensity of the simulated modes for the $+K_g^D$ direction are ~5x weaker than those for the -K_g^D simulations.

The s-polarized specular reflectivity data taken in the M direction for T-5 are shown

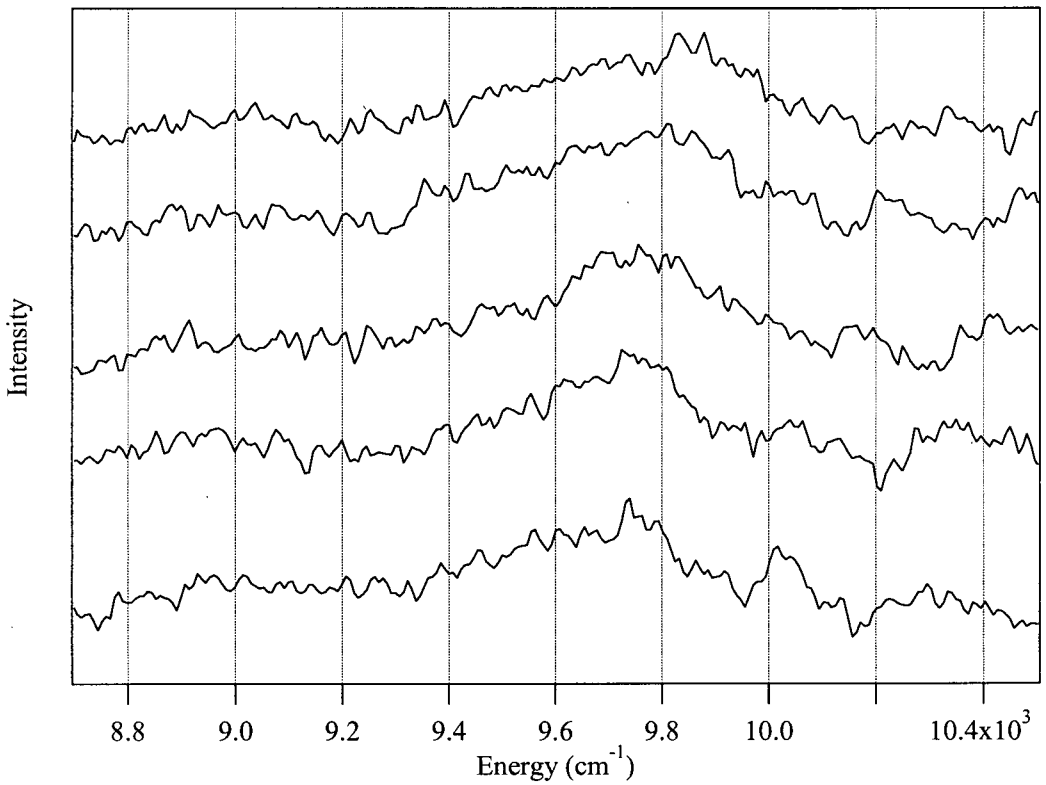

Figure 5.33: Unpolarized $+K_g^D$ diffraction data for T-5. Spectra from the bottom up are for incident angles of 2°, 4°, 6°, 8°, and 10°.

in Figure 5.36. Corresponding simulations for s- and p-polarizations for various angles of incidence are shown in Figure 5.37. At a gross level, both the data and the simulations are very similar to those corresponding to a comparable structure with no defect superlattice. However, evidence of the perturbation is exhibited clearly in the vicinity of the broad, high energy modes at 2.5° and 5° angles of incidence. These additional undulations are more pronounced in the simulations than in the data, especially at large angles of incidence.

In summary, the T-5 diffraction data in the $+K_g^D$ and $-K_g^D$ directions exhibits many of

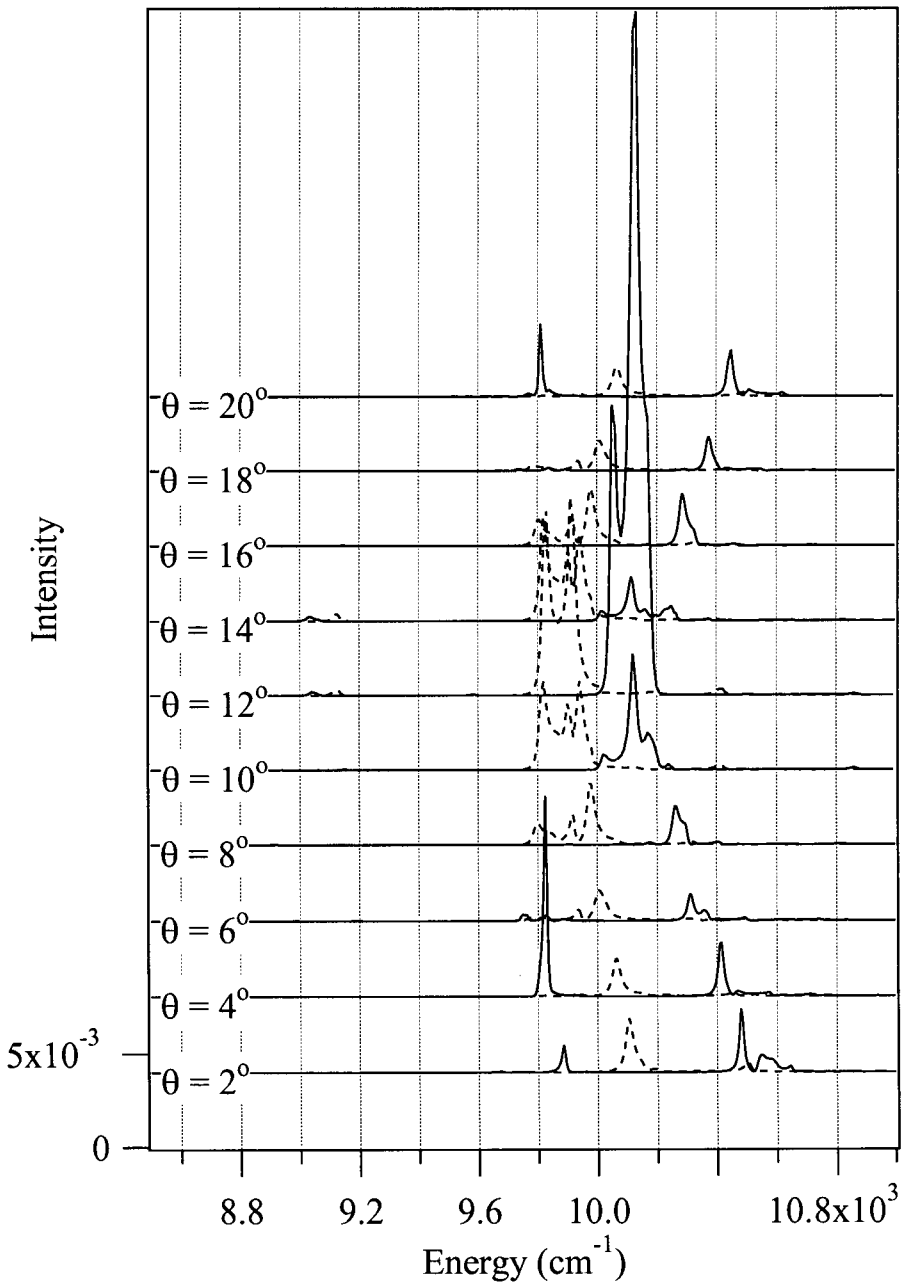

Figure 5.34: Simulation for -K_g^D diffracted order from the defect superlattice of T-5. P-polarized is represented by the dashed lines, and s-polarized by the solid.

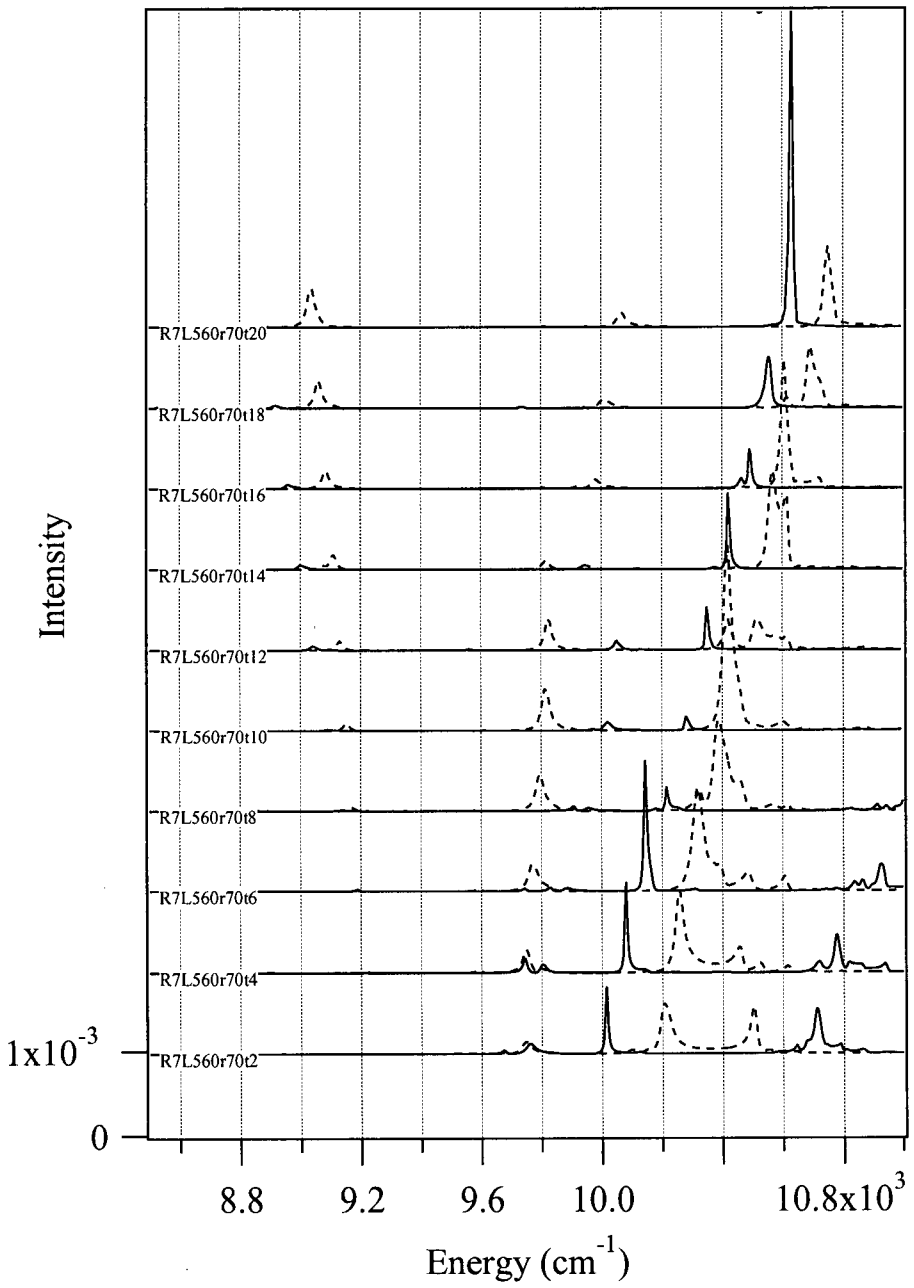

Figure 5.35: Simulation for $+K_g^D$ diffracted order from the defect superlattice of T-5. P-polarized is represented by the dashed lines, and s-polarized by the solid.

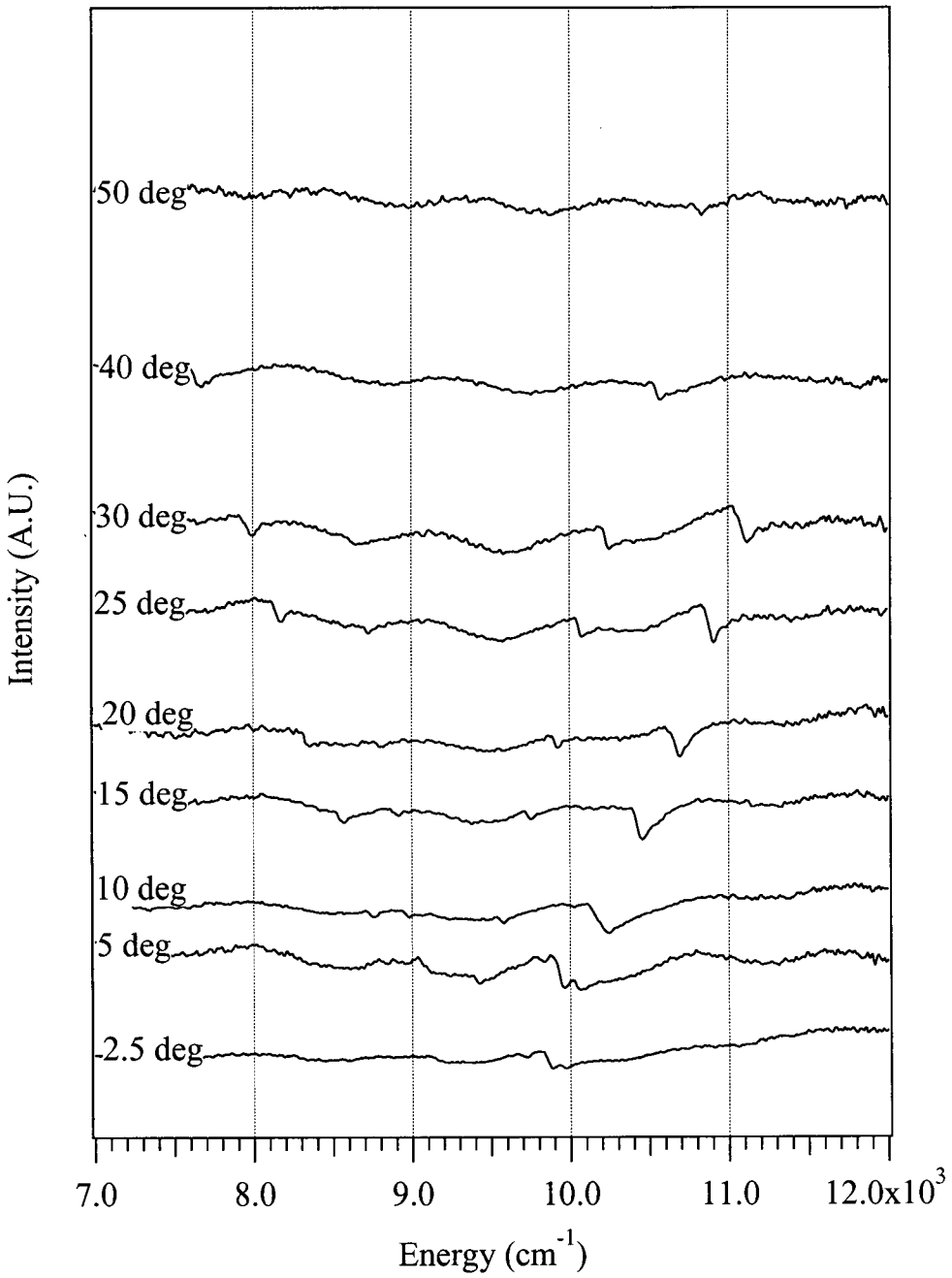

Figure 5.36: S-polarized specular reflectivity data for T-5, taken at various angles of incidence in the M direction.

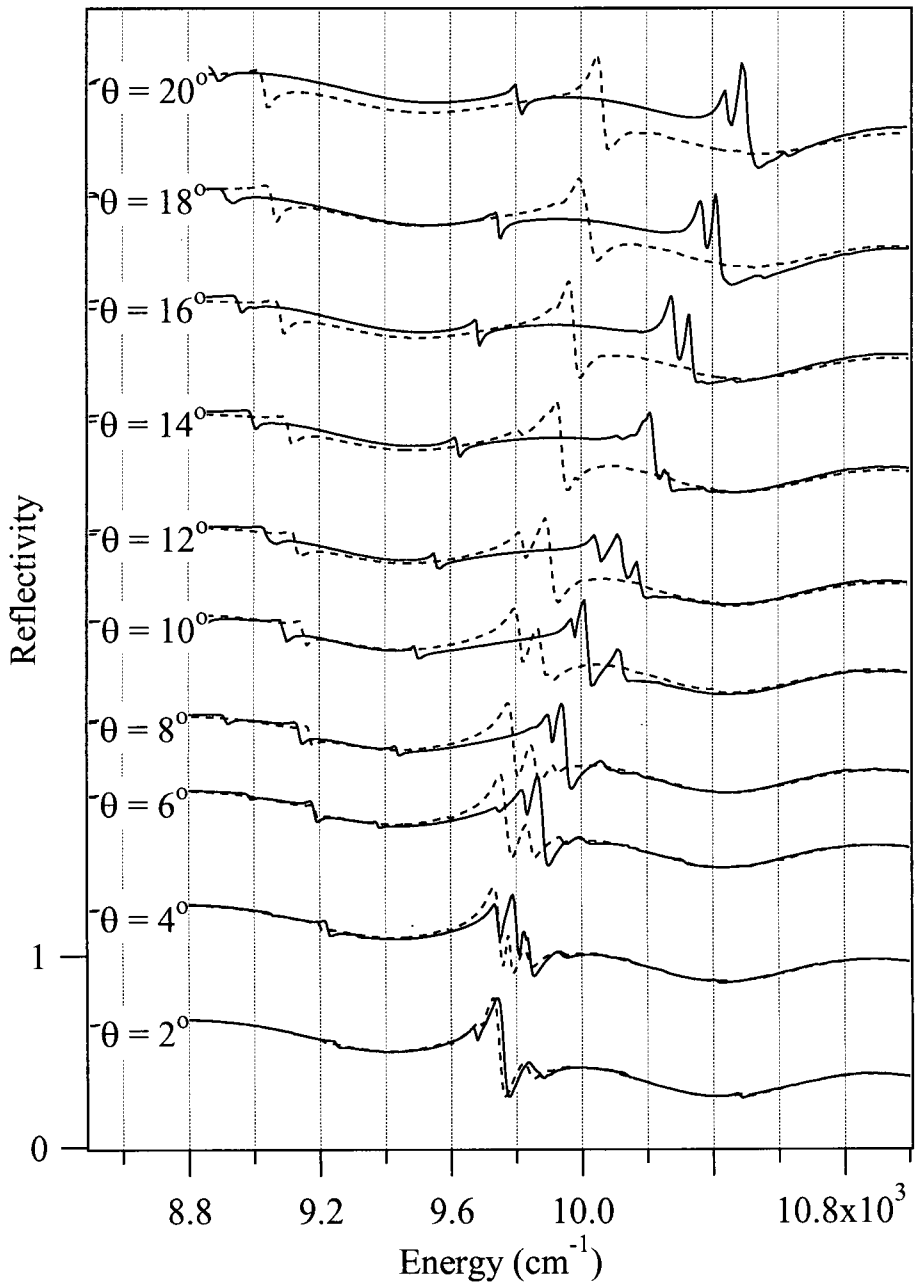

Figure 5.37: S-polarized (solid lines) and p-polarized (dashed lines) specular reflectivity simulations for T-5, at various angles of incidence in the M direction.

the qualitative features predicted by the simulations. Going away from normal incidence in the M direction, the -K_g^D data contains several modes that disperse down in energy out to ~10° angle of incidence, beyond which the group starts to disperse back up in energy. In contrast, the modes in the +K_g^D direction monotonically increase in energy away from normal incidence out to at least ~20°. The linewidths of the modes in the -K_g^D direction are within a factor of two of the simulated modes' linewidths, and the scattering strength in the -K_g^D direction is substantially stronger than in the +K_g^D direction. The principal difference between the experiment and simulations lies in the relative strengths of the various modes that appear in any given order of diffraction. This can largely be attributed to the fact, as borne out by simulations, that the dispersion efficiency in any given order seems to be exceedingly sensitive to variations in incident angle and the structure's precise physical characteristics. More discussion regarding the nature of the modes observed in these spectra follows the presentation of a similar study of sample T-7.

Using the diffraction measurement technique to probe sample T-7 produces the -K_g^D data shown in Figure 5.38. These spectra were obtained at angles of incident light of 2°, 4°, 6° and 15°. No data could be collected from 8° to 14° because the signal for these angles is physically blocked by the apparatus. The bottom three spectra show a single, well-defined mode dispersing down in energy. At 15° there is a single mode located at approximately the same energy as the mode at 2°. Figure 5.39 shows the +K_g^D diffraction data for this sample at 2° and 4°. One mode is apparent; it disperses up from 2° to 4°.

Again, the diffraction signal for the $+K_g^D$ is ~5x weaker than that for the $-K_g^D$.

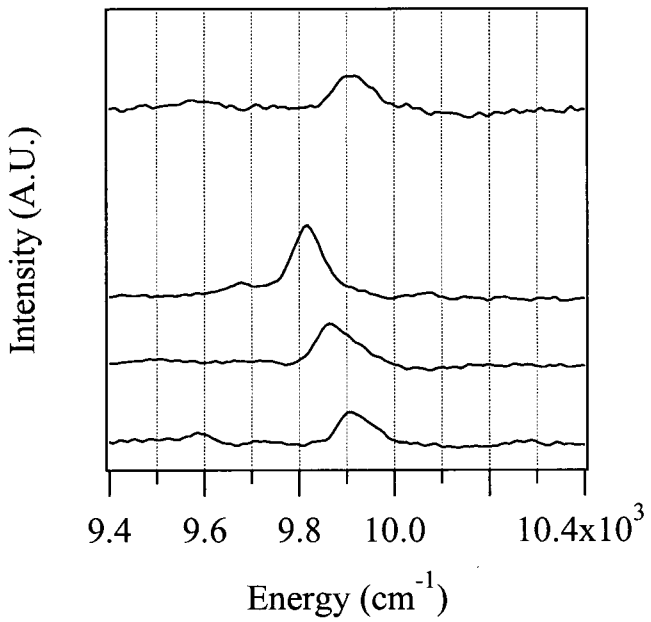

Figure 5.38: Unpolarized $-K_g^D$ data for T-7, taken at 2, 4, 6, and 15° in the M direction.

Simulations were performed for T-7 with the same values used previously to model this waveguide, as described in Section 5.1.2. The simulations for the $-K_g^D$ diffracted order, shown in Figure 5.40, exhibit one s- and one p-polarized group of modes dispersing down in energy from 2°, flattening out between 6° and 10°, and then dispersing up in energy through 18°. The "turn around" in the direction of dispersion occurs between 6° and 10°, which corresponds with the condition where the modes encounter the first Brillouin zone boundary of the defect lattice (just as shown for T-5), which occurs for this structure at 7.9° for 10,000 cm^{-1}. The two dashed lines indicate the location of the base lattice modes, as indicated by the specular reflectivity simulations for the non-defect lattice (shown previously in Figure 5.10). The simulations exhibit qualitative agreement

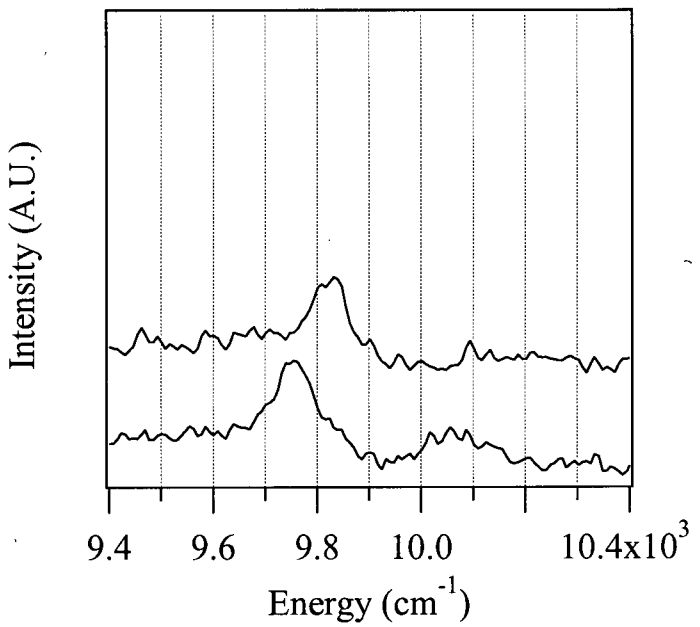

Figure 5.39: Unpolarized $+K_g^D$ data for T-7, for 2 and 4° in the M direction.

with the data with regard to the intensity of the modes, and to the general dispersion; however there is only one mode apparent in the data. The similarity between the 2° and 15° spectra observed in the data is also shown in the simulations. For the $+K_g^D$ simulations, shown in Figure 5.41, one s- and one p-polarized mode are each dispersing continuously up in energy for this range. The dashed line indicates the location of the upward dispersing s-polarized mode, as indicated by specular reflectivity simulations. The continuous upward dispersion of the two modes in the $+K_g^D$ simulations corresponds to the upward dispersion of the single mode shown in the data. The widths of the modes also compare well. Overall, the diffraction data and simulations for sample T-7 exhibit many of the same features seen in the T-5 sample, but the number of modes with significant diffraction efficiency is less in T-7, making it easier to interpret the results.

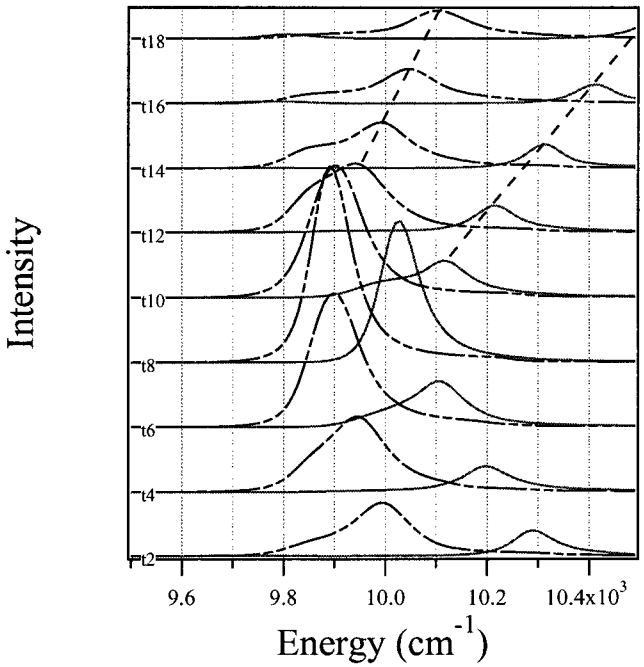

Figure 5.40: Simulation of -K_g^D spectra for T-7. Solid lines represent s-polarization; dashed lines represent p-polarization. Simulation is for the M direction and for angles of 2° to 18° from the bottom up.

The interpretation that follows makes reference to the simulations shown in Figures 5.40 and 5.41, and the schematic diagram of the defect-zone-folded band structure in Figure 5.42. The zone-folding shown in Figure 5.42 involves only the base lattice s- and p-polarized bands (represented by solid lines in the figure) that disperse upward from a common origin at 9,750 cm^{-1}, as in Figure 5.6. Furthermore, it only includes those parts of these bands that are folded by reciprocal lattice vectors oriented along the M direction. That is, it is effectively a 1D reduction that ignores bands folded by defect lattice vectors that do not lie on the Γ–X axis.

By illuminating the sample with a light beam corresponding to the thick gray line in

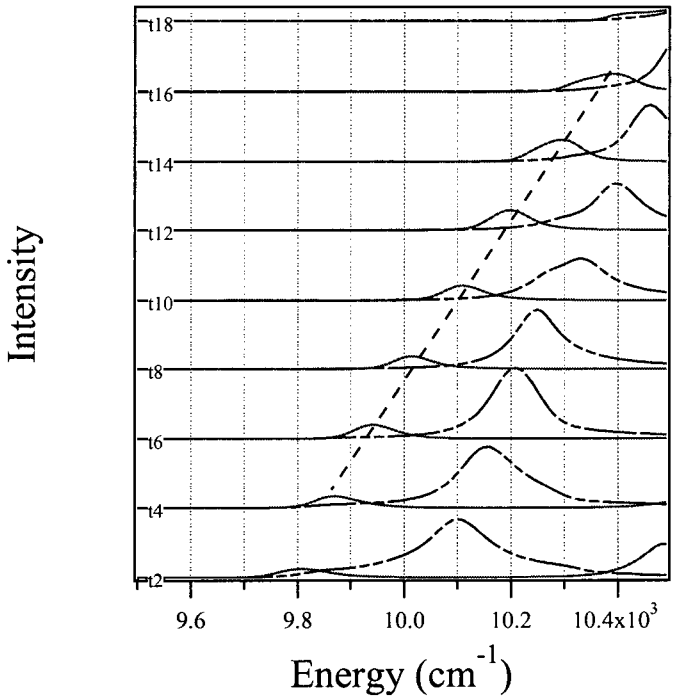

Figure 5.41: Simulation of $+K_g^D$ spectra for T-7. Solid lines represent s-polarization; dashed lines represent p-polarization. Simulation is for the M direction and for angles of 2° to 18° from the bottom up.

Figure 5.42, many bands are excited at locations indicated by the open circles. All of the zone-folded bands in this figure can be excited with a beam incident at angles between 0 and ~7.9°. The modes that show up clearly in the $-K_g^D$ simulations for sample T-7 over this angular range correspond to the two downward dispersive bands shown as dashed lines in the figure. The modes that show up clearly in the $+K_g^D$ simulations over this angular range correspond to the two of the upward dispersive bands. Specifically, the lower energy mode corresponds to the upward dispersing s-polarized band from the base lattice (solid line in Figure 5.42 labeled 's') while the higher energy mode corresponds to the dash-dot line which is the second zone-fold of the upper dispersing p-polarized

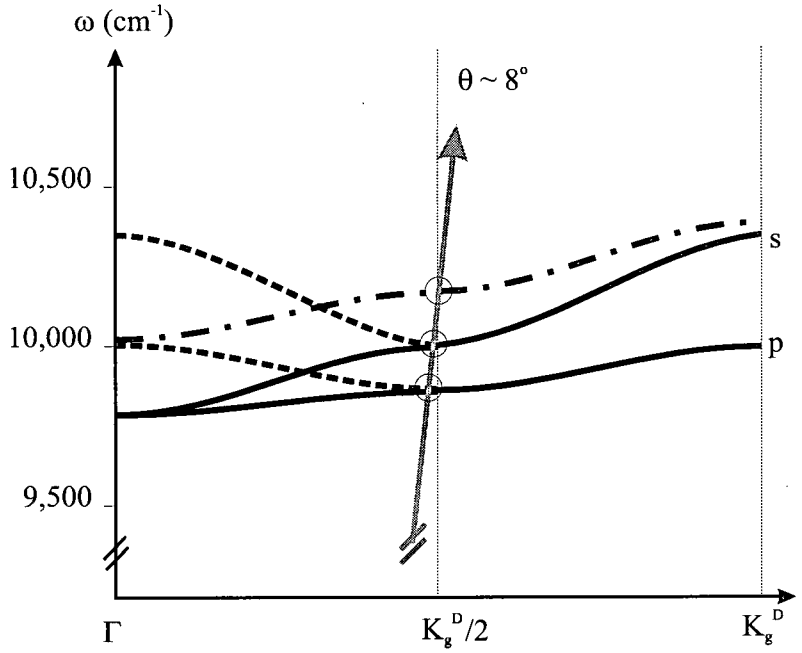

Figure 5.42: Schematic zone diagram showing upward dispersing bands at top of second order TE-like gap in the M direction. The dashed lines represent the downward dispersing bands and the solid lines represent the upward dispersing bands.

band from the base lattice. Other bands, most notably the lowest upward dispersing p-polarized band, are almost completely absent in the -K_g^D diffraction signal. Looking back at the T-5 simulations, some of the peaks correspond to these same bands. Note, however, that the lowest upward dispersing p-polarized branch is visible, as are higher lying bands. The principal difference between T-7 and T-5 samples is that there are numerous other bands in T-5 that contribute to the diffraction, although they are weaker than those in T-7. Most of these additional bands in T-5 are effectively zone-folded by reciprocal lattice vectors oriented away from the Γ–X axis.

Thus it appears that for dilute superlattices the signals diffracted via different orders of the defect lattice provide a direct, background-free probe of the 1D zone-folded base

bands, as anticipated. More dense superlattices cause a more significant perturbation to the base band structure, resulting in more complicated spectra. Although in principle the data could be "unfolded" in 2D, this would represent a significant challenge. The biggest difficulty appears to be the huge variability in the diffraction efficiency, both within a band (as a function of in-plane wavevector) and between different bands. These efficiencies are also very sensitive to the geometrical parameters of the structures.

With this understanding, the diffraction data from T-7 can also be better interpreted. Figure 5.43 shows the s-polarized, and Figure 5.44 the p-polarized specular reflectivity data collected in the M direction for T-7. The high energy mode in the s-polarized data and the high energy mode in the p-polarized data are degenerate where they intersect zone center at 9,750 cm^{-1}. These modes disperse up in energy away from zone center. The mode seen in the $+K_g^D$ diffraction data (Figure 5.39) also has a value of 9,750 cm^{-1} at zone center, and disperses up in energy away from zone center. The mode in the $+K_g^D$ data is a background-free representation of the s-polarized base lattice mode seen in the specular reflectivity spectra. Referring to the $-K_g^D$ diffraction data (Figure 5.38), the mode disperses down from 9,900 cm^{-1} to 9,750 cm^{-1} as it approaches 8°, which is the intersection of the mode with zone edge. This mode in the $-K_g^D$ data is a background-free representation of the p-polarized base lattice mode seen in the specular reflectivity data. The relative diffraction efficiencies are different from the simulations, but the basic interpretation is the same. Thus, the superlattice diffraction measurement technique does provide a background-free probe of the band structure of textured planar waveguides

when the defect superlattice is dilute.

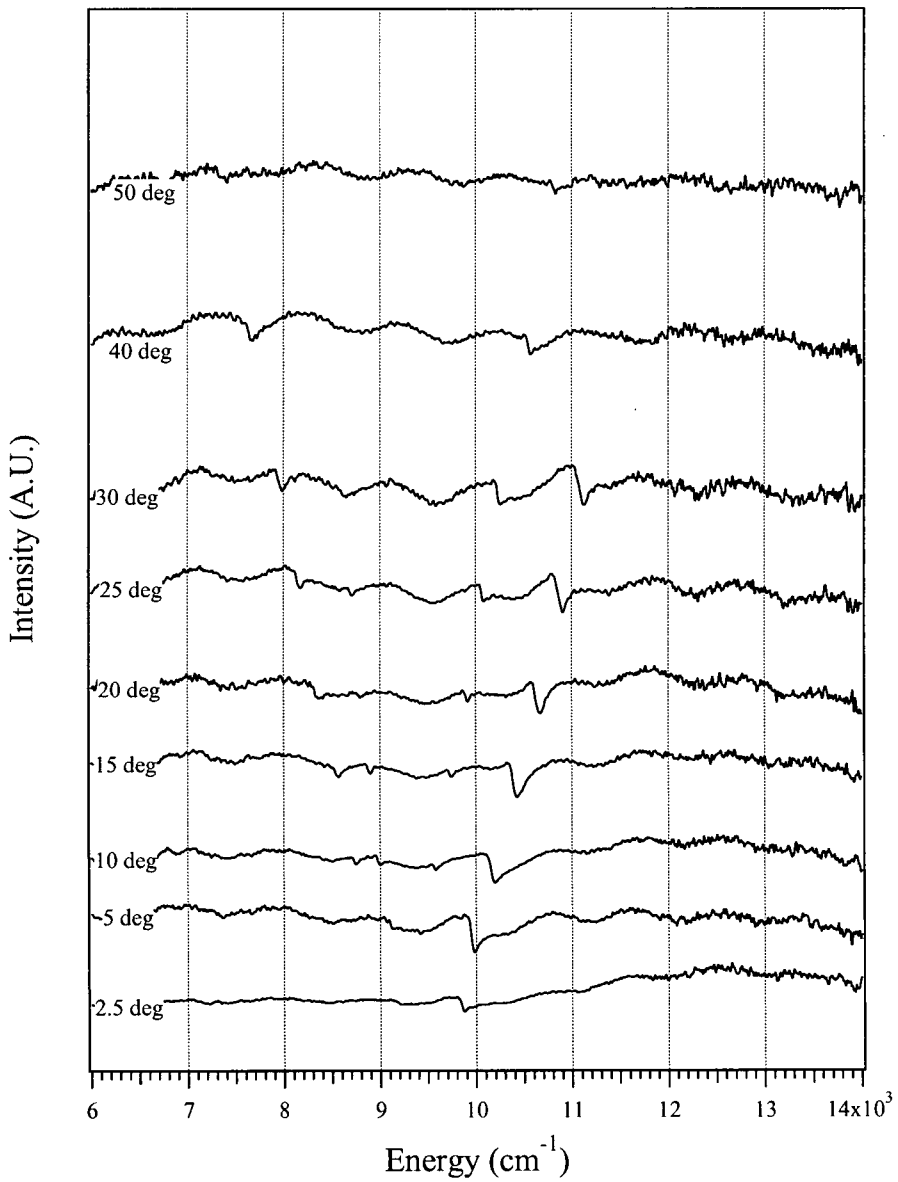

Figure 5.43: S-polarized specular reflectivity data for T-7 taken in the M direction.

The diffraction measurement technique can extend the level of quantitative agreement between experimental results and theoretical predictions by providing background-free

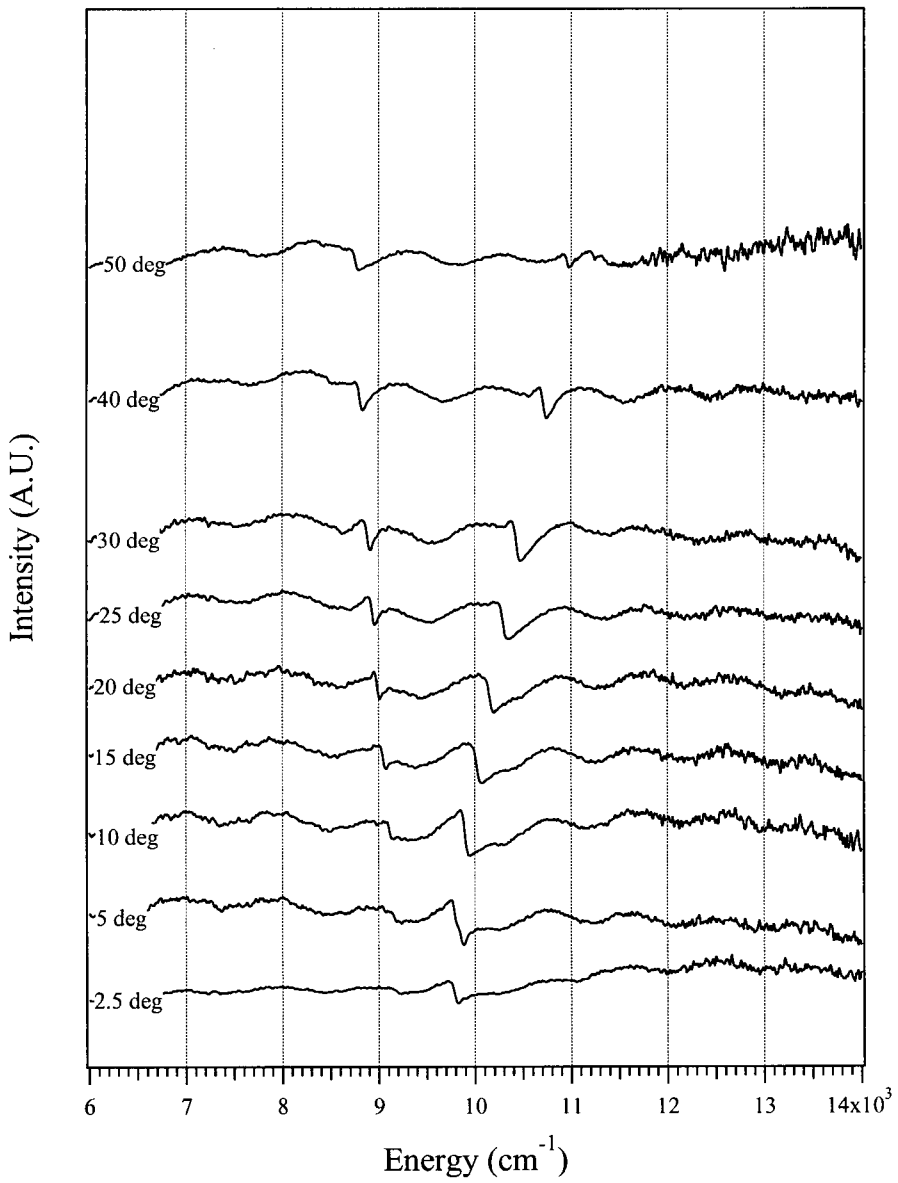

Figure 5.44: P-polarized specular reflectivity data for T-7 taken in the M direction.

mode profiles. Specifically in the case of T-7, this aids in the determination of the thickness of the oxide layer beneath the waveguide core. The $+K_g^D$ diffraction data taken with light incident at 2° is shown in the bottom graph of Figure 5.45 with simulations of

this structure done for various thicknesses of the oxide layer. The bottom simulation is for a fully-oxidized layer, the next is for 900 nm of oxide, the third is for 300 nm, and the top is for 200 nm. Based on the linewidth, it can be concluded that the oxide layer for T-7 is approximately 200 nm thick, which agrees with the Fabry-Perot spacing evident in Figure 5.5.

To conclude this section, the diffraction measurement technique can provide a background-free probe of dispersive modes, as well as flat bands. The scattering strength of the flat bands tends to be stronger than that from dispersive bands. This technique works best for dispersive modes when the defect superlattice represents a weak perturbation to the base lattice modes. When the perturbation is strong, the technique is not as useful for probing the base lattice modes because the defect superlattice causes a complicated renormalization of the slab modes, rendering the data difficult to decipher. While this technique does not replace the specular reflectivity technique for studying the dispersion of leaky photonic eigenstates, it does further the qualitative and quantitative understanding of textured planar waveguide band structure by providing background-free measurements of the modes' lineshapes, and hence their lifetimes.

5.3.3 True Defect Modes

The previous sections have discussed the incorporation of defect superlattices into textured planar waveguides as a means of revealing the leaky-mode band structure characteristic of the underlying base lattice. This section discusses the design of a textured

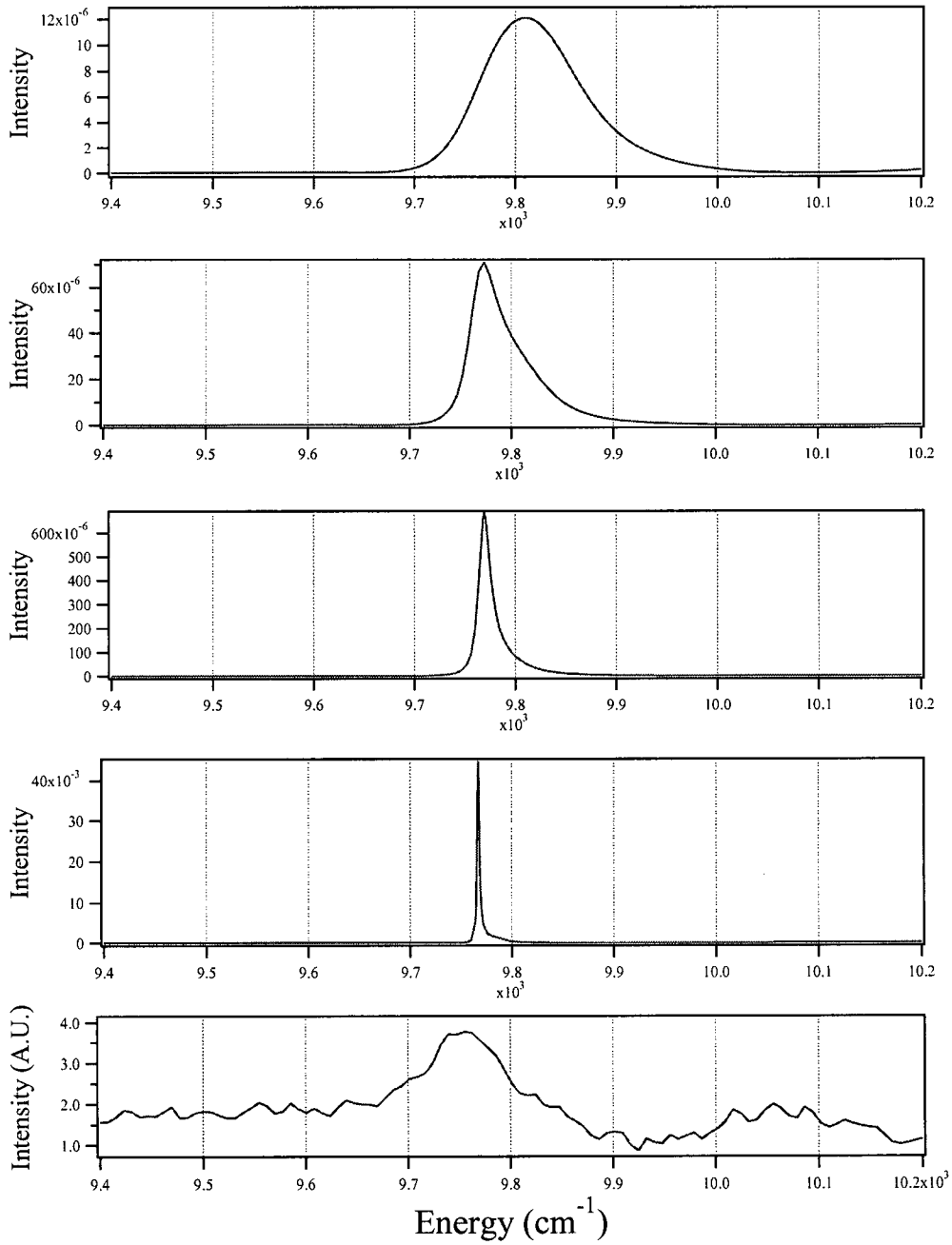

Figure 5.45: Triangular superlattice diffraction data compared with simulations for various oxide thicknesses. Simulations and data are for -K_g^D diffraction with incident light at 2° in the M direction. The oxide thickness for the simulations are, from the bottom up, 1600 nm, 900 nm, 300 nm, and 200 nm.

planar waveguide in which the base lattice possesses a complete pseudo-gap. The defect superlattice configuration is similar to that of the previously discussed T-7 sample. This superlattice gives rise to a defect band within the complete pseudo-gap that exhibits virtually no dispersion. As discussed above, such a structure makes possible a whole range of passive as well as active optical devices, such as channel waveguides [12, 40], notch filters and lasers [22]. Simulations of the specular reflectivity and superlattice diffraction from this sample show clear evidence of both the defect band and other base lattice bands that lie below the light line. These results theoretically validate the original concept of using defect superlattices not only as a background-free probe of *leaky* localized modes (as discussed in detail in Sections 5.3.1 – 5.3.2), but also as a means of probing modes below the light line, and localized defect bands.

In order to realize a complete pseudo-gap in a periodically textured planar waveguide, the lattice must possess a high degree of symmetry, and have an air filling fraction far from zero or one. To this end, a textured planar waveguide was designed with a triangular lattice and an air filling fraction of 34%. The other design parameters for this structure are detailed in Table 5.6. This design includes a defect superlattice that omits every seventh hole.

The simulated dispersion diagram for the TE band in this structure is shown in Figure 5.46. Note that this dispersion is for the base lattice only, in order to clearly demonstrate the magnitude of the complete first order TE pseudo-gap. This large gap extends from $7565\,\mathrm{cm}^{-1}$ to $9120\,\mathrm{cm}^{-1}$, which is 18.6% of the center frequency. The first order TM gap

Table 5.6: Design parameters for textured planar waveguide with defect mode

Parameter	Value
Pitch	375 nm
Hole radius	115 nm
Thickness of core	150 nm
Core composition	GaAs
Oxide thickness	1000 nm
Hole depth	150 nm

is much smaller and higher in energy, and does not overlap this region.

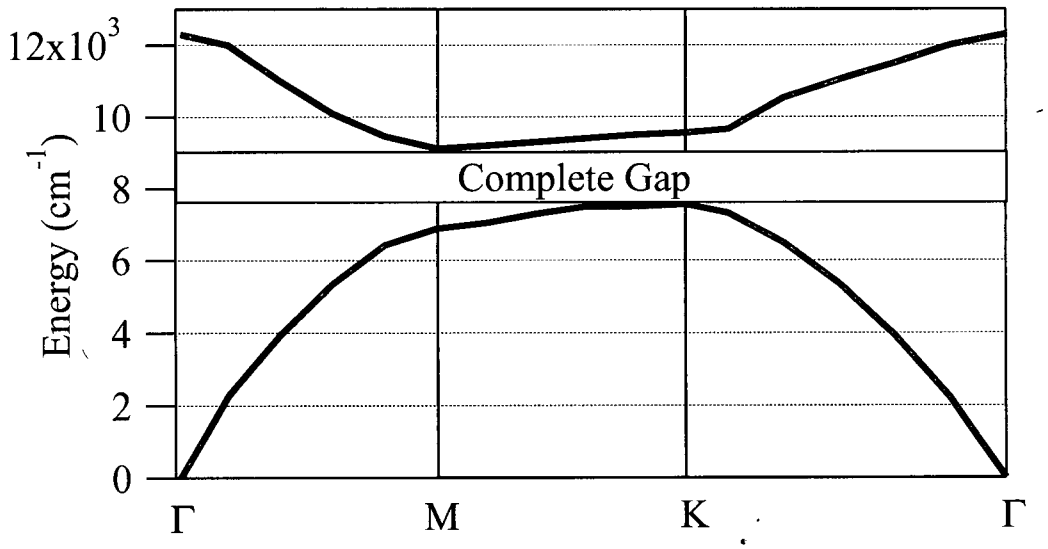

Figure 5.46: Dispersion diagram for the textured planar waveguide with the parameters shown in Table 5.6, showing a large TE pseudo-gap.

The inclusion of the defect superlattice in this waveguide creates a mode within the large first order pseudo-gap. Simulations of the specular reflectivity for this structure are shown in Figure 5.47 for a range of incident angles along the M direction. The

pronounced feature at 8,300 cm^{-1} is evidence of the existence of this mode. Although this is strictly a TE gap, the defect mode is evident in both the s- and p-polarizations. Note that there is virtually no dispersion of this defect band.

Figure 5.48 shows the simulated -K_g^D diffracted signal for this structure. Once again, the defect mode is apparent at 8,300 cm^{-1} in both the s- and p-polarizations for all angles of incidence along the M direction. These background-free spectra highlight several other smaller features, which were not as apparent in the specular reflectivity simulations. These features occur primarily near the edges of the pseudo-gap, and are associated with the band edges of the base lattice which lie below the light line as discussed in Section 2.3.2. These features are similar in nature to the defect-zone-folded signatures of the base lattice modes discussed extensively above, but here the corresponding base lattice bands lie below the air light line. It is highly desirable to be able to directly probe the dispersion of the truly bound modes that lie beneath the light line, and these simulations demonstrate that defect superlattices offer this ability, in principle.

Figure 5.49 is a momentum space diagram illustrating the relative strengths of the Fourier coefficients that comprise this defect mode when excited at a 10° angle of incidence. To make this diagram, the Fourier coefficients for each reciprocal lattice vector were extracted at the central energy of the defect mode for light incident at 10° angle of incidence aligned in the M direction. Each dot represents a reciprocal lattice vector (by position) and the relative magnitude (by dot diameter) of the corresponding Fourier field component. This number of reciprocal lattice vectors was required in order to model

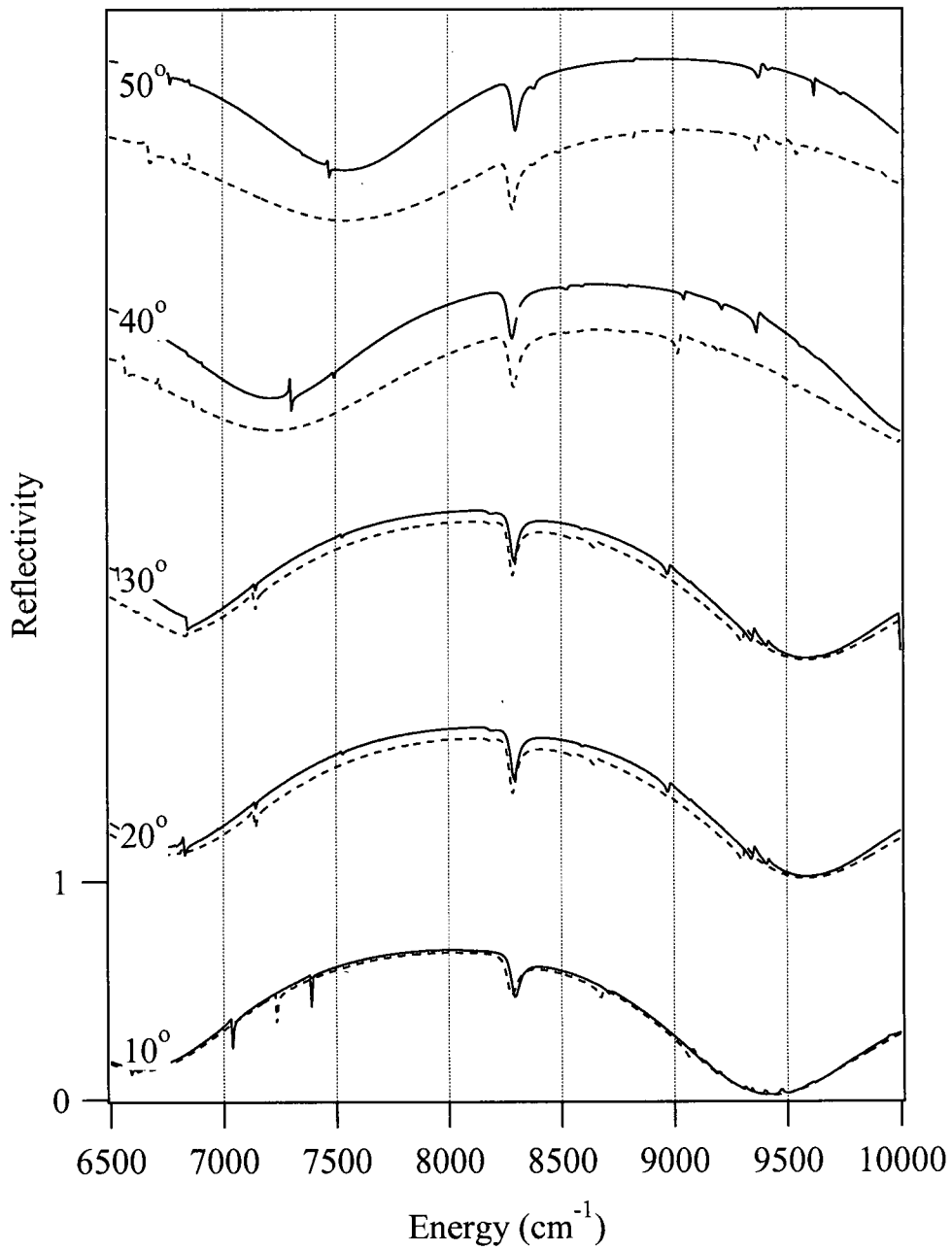

Figure 5.47: Simulated specular reflectivity for a textured planar waveguide with a triangular lattice, exhibiting a dispersion-free defect band in the first order pseudo-gap, shown for angles of incidence of 10°, 20°, 30°, 40° and 50° along the M direction. The solid lines represent s-polarized and the dashed lines represent p-polarized reflectivity spectra.

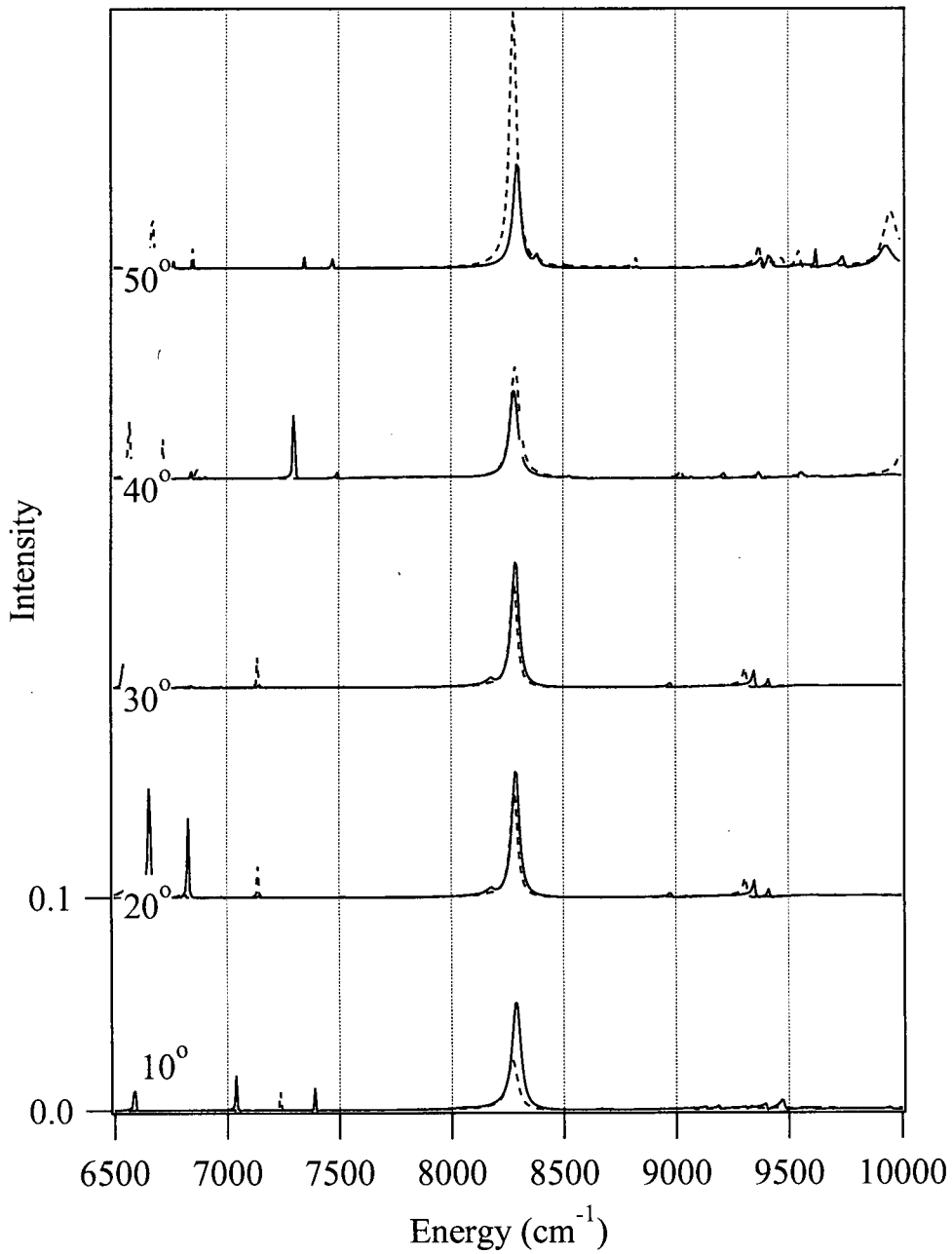

Figure 5.48: Simulated -K_g^D diffraction for a textured planar waveguide with a triangular lattice, exhibiting a dispersion-free defect mode in the first order pseudo-gap, shown for angles of incidence of 10°, 20,° 30,° 40° and 50° along the M direction. The solid lines represent s-polarized and the dashed lines represent p-polarized diffraction spectra.

a structure with a defect superlattice such as this. The strong Fourier coefficients (i.e. the larger dots) that contribute to this defect mode occur primarily at a radius half-way between zone center and the smallest *base* lattice vectors, which correspond to the seventh ring of reciprocal lattice vectors in this diagram. This makes sense because the energies of the base lattice TE slab modes at this average wavevector fall within a large TE-like pseudo-gap. Recall that the corresponding diagrams for dispersive modes shown in Section 5.1.2 were all dominated by just one or two components. The relatively large number of significant components associated with the defect bands also makes sense, because an infinitely localized state would correspond to a uniform dot size in this figure.

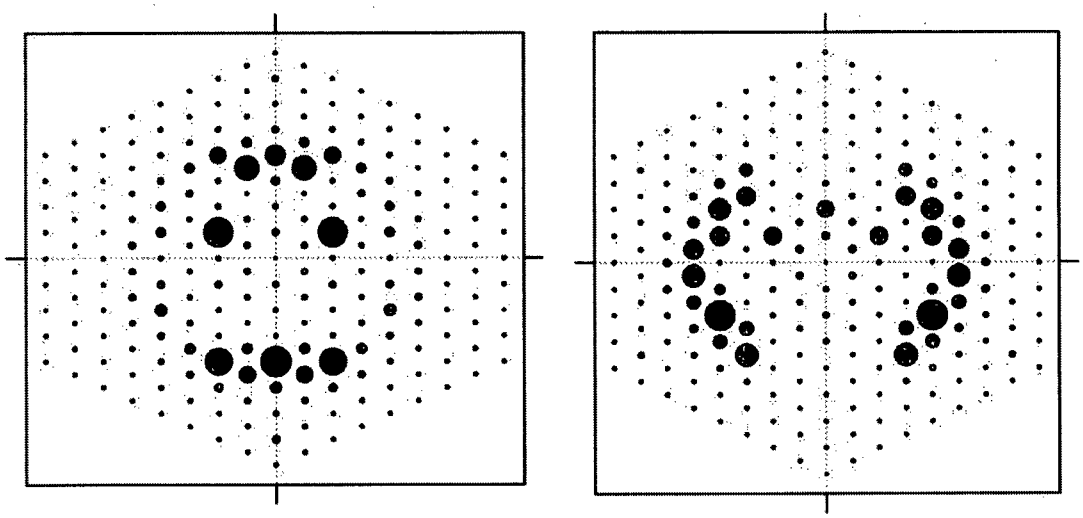

(a) s-polarization (b) p-polarization

Figure 5.49: Momentum space diagram for the defect mode in the waveguide with the triangular lattice discussed in the text. M direction is up in the diagram. The defect superlattice for this waveguide omits every seventh hole. The size of the dots shows the relative strengths of the Fourier coefficients of the fields excited at a 10° angle of incidence along the M direction.

Using these Fourier coefficients and reciprocal lattice vectors to plot the intensity of the s-polarized fields of the defect mode yields the real space diagram shown in Figure 5.50. This figure shows significant localization of the fields on the locations of the defect sites when illuminated with white light at a 10° angle of incidence along the M direction. This illustrates the fact that light within the pseudo-gap is not permitted to travel classically through the waveguide, but can tunnel from defect site to defect site. It has been shown that when these defect sites are arranged in particular patterns (e.g. straight lines, straight lines with bends, etc.), light at the frequency of the defect mode can be made to "follow the defects." [2].

A textured planar waveguide was fabricated to the specifications delineated above. As the parameters for this structure are similar to the other GaAs textured waveguides fabricated for the research presented in this thesis, the realization of this waveguide design should be no less successful than the other structures. However, characterization of this waveguide has revealed only a broad, unstructured emission covering the entire first order pseudo-gap. The reason for this is not known.

Although this design has not been experimentally realized, a patent application is in the process of being filed for its use as a polarization and angle insensitive notch filter. Recall that the notch filter referred to in the context of the polymer waveguide involved polarization-insensitive response, which is desirable; but the center frequency of the notch varied continuously with the incident angle, which may or may not be desirable,

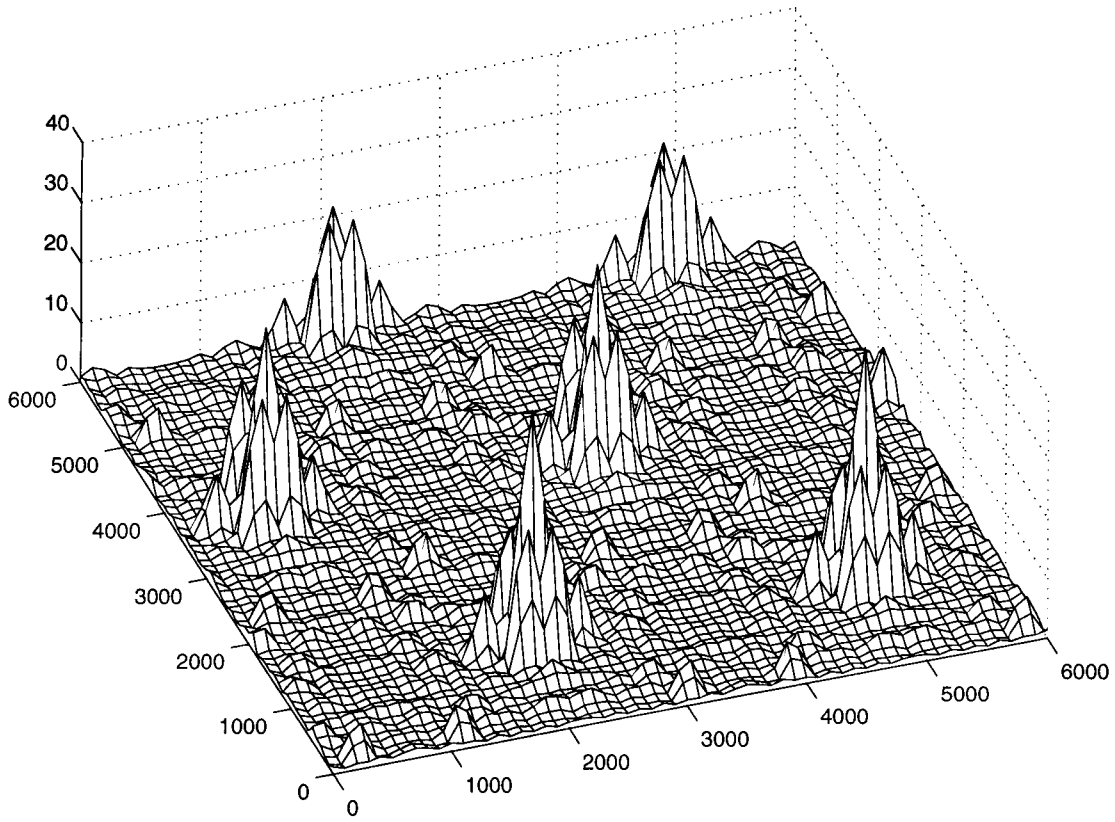

Figure 5.50: Real space plot of the magnitued squared of the total vector field at the surface of the defect lattice waveguide discussed in the text, for a 10° angle of incidence along the M direction. There is strong localization of the field at the defect sites.

depending upon the application. Here, the use of a high index-contrast textured waveguide capable of supporting a complete pseudo-gap, together with the defect superlattice, offers polarization insensitive filtering at a fixed frequency, independent of incident angle.

To summarize this section, the theoretical model used in previous sections to quantitatively explain the scattering properties of several different 2D textured waveguides was used to design a different structure with a complete TE pseudo-gap. The model predicts that clear signatures of near-dispersionless gap modes and base lattice modes

below the light line should be observed in white light scattering spectra when a defect superlattice is incorporated in the structure. Although the first and only attempt to verify these predictions was not successful, this is almost certainly a consequence of fabrication difficulties, not an indication that the design is flawed.

Chapter 6

Conclusions and Recommendations

The objective of the work presented in this thesis, to reveal and quantify the broadband linear optical scattering properties of 2D textured planar waveguide structures, has been achieved. The factors contributing to this success were a versatile, accurate and easy-to-use broadband spectroscopy apparatus, a rigorous yet efficient computer model, and the ability to fabricate the relevant samples. The author processed the majority of the samples, was solely responsible for the apparatus, and extended the modeling code by developing and implementing the routines necessary to model defect superlattices. Overall, outstanding agreement was achieved between the experimental characterization of the samples using the author's apparatus and the results obtained with the computer modeling code. Together the theoretical and experimental results provide a comprehensive examination of electromagnetic excitations associated with 2D textured planar waveguides.

By achieving unprecedented agreement of measured and calculated band structures of leaky modes associated with the second, and up to the seventh, zone-folded Brillouin

zones of square and triangular lattice structures, a thorough characterization of the polarization and dispersive properties of these localized electromagnetic modes has been achieved. All of the results can be interpreted using symmetry arguments and a picture in which the true Bloch states are the result of texture-inducing mixing of TE-like and TM-like slab modes characteristic of the underlying "average" slab waveguide. The pure kinematic effects of 2D texturing are revealed in the scattering spectra from a novel azo-polymer-based structure. More substantial renormalization effects are clearly evident in the GaAs-based structures: second order gaps at zone center $\sim$10%; complete first order pseudo-gaps $\sim$20% of the center frequencies; significant anti-crossings away from zone center; and nearly dispersion-free modes across the entire Brillouin zone, both outside and inside a complete pseudo-gap.

The work presented in this thesis has contributed significantly to the quantitative analysis of the dispersion characteristics of 2D textured planar waveguides due, in large part, to the use of the specular reflectivity and diffraction measurement techniques implemented in combination with the specially designed experimental apparatus. The specular measurement technique has proved to be an invaluable overall characterization tool for probing the leaky photonic modes attached to these planar waveguides. The diffraction measurement technique, developed by the author, has been shown to enhance this characterization of leaky modes by providing background-free spectra, especially from modes with low dispersion. It has also been shown to provide background-free spectra from more highly dispersive leaky modes of a textured planar waveguide with a defect

superlattice, when the defects are spaced widely enough so as not to strongly perturb the renormalized base lattice modes. In addition, this diffraction measurement technique has been explored for its potential to uniquely supplement specular reflectivity characterization by enabling the probing of all base lattice modes, including those below the light line. Although characterization of these bound modes has not been experimentally demonstrated, the model simulations give confidence that the method is sound.

Recommendations for future work include continued efforts to use the diffraction measurement technique to characterize modes below the light line. This could be made easier by replacing the low power white light source with a higher power arc lamp. Once a good sample is fabricated with a localized defect mode, a near-field optical scanning microscope (NSOM) could be used to map the physical extent of the localized mode.

Bibliography

[1] Joseph F. Ahadian and Jr. Clifton G. Fonstad. Epitaxy-on-electronics technology for monolithic optoelectronic integration. *Optical Engineering*, 37:3161, 1998.

[2] Mehrnet Bayindir, B. Temelkuran, and E. Ozbay. Propagation of photons by hopping: A waveguiding mechanism through localized coupled cavities in three-dimensional photonic crystals. *Physical Review B*, 61(18):855–858, 2000.

[3] Alvaro Blanco, Emmanuel Chomski, Serguei Grabtchak, Marta Ibisate, Sajeev John, Stephen W. Leonard, Cefe Lopez, Francisco Meseguer, Hernan Miguez, Jessica P. Mondia, Geoffrey A. Ozin, Ovidiu Toader, and Henry M. van Driel. Large-scale synthesis of a silicon photonic crystal with a complete three-dimensional bandgap near 1.5 micrometers. *Nature*, 405:437–440, 2000.

[4] E. R. Brown and O.B. McMahon. High zenithal dirctivity from a dipole antenna on a photonic crystal. *Applied Physics Letters*, 68(9):1300–1302, 2000.

[5] A.R. Cowan. Periodically textured planar waveguides. Master's thesis, University of British Columbia, 2000.

[6] A.R. Cowan, P. Paddon, V. Pacradouni, and Jeff F. Young. Resonant scattering and mode coupling in two-dimensional textured planar waveguides. *Journal of the Optical Society of America*, 18(5), 2001.

[7] F. Gadot, A. de Lustrac, J.M. Lourtioz, T. Brillat, A. Ammouche, and E. Akmonsoy. High-transmission defect modes in two-dimensional metallic photonic crystals. *Journal of Applied Physics*, 85(12):8499–8501, 1999.

[8] Melles Griot. Photonics components, 2000.

[9] Eugene Hecht. *Optics, 2nd ed.* Addison-Wesley, 1987.

[10] M. S. Ho, A. Natansohn, and P. Rochon. Azo polymers for reversible optical storage. *Macromolecules*, 28:6124–6127, 1995.

[11] Chongjun Jin, Bingyin Cheng, Baoyuan Man, Zhaolin Li, Daozhong Zhang, Shouzheng Ban, and Bo Sun. Band gap and wave guiding effect in a quasiperiodic photonic crystal. *Applied Physics Letters*, 75(13):1848–1850, 1999.

[12] John D. Joannopoulos, Robert D. Meade, and Joshua N. Winn. *Photonic Crystals.* Princeton University Press, 1995.

[13] S. John. Strong localizaation of photonc in certain disordered dielectric superlattices. *Physics Review Letters*, 58:2486–2489, 1987.

[14] Vladimir Kuzmiak and Alexei A. Maradudin. Localized defect modes in a two-dimensional triangular photonic crystal. *Physical Review B*, 57(24):242–250, 1998.

[15] F. Lagugne Labarthet, P. Rochon, and A. Natansohn. Polarization analysis of diffracted orders from a birefringence grating recorded on azobenzene containing polymer. *Applied Physics Letters*, 75(10):1377–1379, 1999.

[16] S.Y. Lin, J. G. Fleming, D. L. Hetherington, B.K. Smith, R. Biswas, K.M. Ho, M. M. Sigalas, W. Zubrzycki, S.R. Kurtz, and et al. A three-dimensional photonic crystal operating at infrared wavelengths. *Nature*, 394:251–253, 1998.

[17] W.J. Mandeville, V. Pacradouni, A.R. Cowan, S. Johnson, and Jeff F. Young. Two dimensional photonic crystals with defect superlattices in air/gaas/al-oxide membranes. *International Conference on the Physics of Semiconductors*, Sep 2000.

[18] C.A. Murray and D.G. Grier. Colloidal crystals. *American Scientist*, 83, 1995.

[19] J.C. Nabity. Nanometer pattern generation system, 2001.

[20] V. Pacradouni, W.J. Mandeville, A.R. Cowan, P. Paddon, Jeff F. Young, and S.R. Johnson. Photonic band structure of dielectric membranes periodically textured in two dimensions. *Physical Review B*, 2000.

[21] Vighen Pacradouni. *Photonic bandstructure in strongly two-dimensionally textured semiconductor slab waveguides.* PhD thesis, University of British Columbia, 2001.

[22] O. Painter, R. K. Lee, A. Scherer, A. Yariv, J. D. O'Brien, P.D. Dapkus, and I. Kim. Two-dimensional photonic band-gap defect mode laser. *Science*, 284:1819–1821, 1999.

[23] Song Peng and G. Michael Morris. Resonant scattering from two-dimensional gratings. *Journal of the Optical Society of America*, A13:993, 1996.

[24] P. Rochon, J. Gosselin, A. Natansohn, and S. Xie. Optically induced and erased birefringence and dichroism in azoaromatic polymers. *Applied Physics Letters*, 60(1), 1992.

[25] P. Rochon, A. Natansohn, C.L.Callender, and L. Robitaille. Guided mode resonance filters using polymer films. *Applied Physics Letters*, 71(8):1008–1010, 1997.

[26] Paul Rochon. Personal communication, 2000.

[27] R.E. Sah, J.D. Ralston, S. Weisser, and K. Eisele. Characteristics of a two-component chemically-assisted ion-beam etching technique for dry-etching of high-speed multiple quantum well laser mirrors. *Applied Physics Letters*, 67(7), 1995.

[28] Kazuaki Sakoda. Low-threshold laser oscillation due to group-velocity anomaly peculiar to two- and three-dimensional photonic crystals. *Optics Express*, 4(12):481–489, 1999.

[29] Kazuaki Sakoda and Kazuo Ohtaka. Optical response of three-dimensional photonic lattices: Solutions of inhomogeneous maxwell's equations and their applications. *Physical Review B*, pages 5732–5741, 1996.

[30] Kazuaki Sakoda and Kazuo Ohtaka. Sum-frequency generation in a two-dimensional photonic lattice. *Physical Review B*, 54(8):5742–5749, 1996.

[31] Kazuaki Sakoda and Hitomi Shiroma. Numerical method for localized defect modes in photonic lattices. *Physical Review B*, pages 4830–4835, 1997.

[32] F. Sfigakis. Optical characterization of $al_xga_{1-x}as$ oxides. Master's thesis, University of British Columbia, 1999.

[33] F. Sfigakis, P. Paddon, M. Adamcyk, C. Nicoll, A.R. Cowan, T. Tiedje, and Jeff F. Young. Near-infrared refractive index of thick, laterally oxidized algaas cladding layers. *Journal of Lightwave Technology*, 18(2):199–202, 2000.

[34] B. Temelkuran, Mehmet Bayindir, E. Ozbay, R. Biswas, M. M. Sigalas, G. Tuttle, and K. M. Ho. Photonic crystal-based resonant antenna with a very high directivity. *Journal of Applied Physics*, 87(1):603–605, 2000.

[35] Pierre R. Villeneuve, Shanhui Fan, and J. D. Joannopoulos. Microcavities in photonic crystals: Mode symmetry, tunability, and coupling efficiency. *Physical Review B*, 54(11):7837–7842, 1996.

[36] D.C. Wright and N.D. Mermin. Crystal liquids: The blue phase. *Review of Modern Physics*, 61:385, 1989.

[37] E. Yablonovitch. Inhibited spontaneous emission in sold state physics and electronics. *Physics Review Letters*, 58:2059–2062, 1987.

[38] E. Yablonovitch, T.J. Gmitter, and K.M. Leung. Photonic band structures: The face-centered cubic case employing non-spherical atoms. *Physics Review Letters*, 67:2295, 1991.

[39] N. Yamamoto, S. Noda, and A. Sasaki. New realization method for three-dimensional photonic crystal in the optical wavelength region: Experimental consideration. *Japan Journal of Applied Physics*, 1:1907, 1997.

[40] A.M. Zheltikov, S.A. Magnitskii, and A.V. Tarasishin. Localization and channeling of light in defect modes of two-dimensional photonic crystals. *JETP LETTERS*, 70(5):323–328, 1999.